Thermal Management of an Axial Flux Permanent Magnet Machine Considering Heat Pipes

Seath Scowby

Thesis presented in partial fulfilment of the requirements for the degree
Master of Science in Engineering at the University of Stellenbosch

Thesis supervisor: R. T. Dobson
Co-Supervisor: Prof. M. J. Kamper

March 2003

DEPARTMENT OF MECHANICAL ENGINEERING
UNIVERISTY OF STELLENBOSCH

Declaration

I, Seath Scowby, the undersigned, hereby declare that the work contained in this thesis is my own original work and has not previously, in its entirety or in part, been submitted at any university for a degree.

Signature of candidate

Day of 2003

Summary

Axial Flux Permanent Magnet (AFPM) machines have become attractive because of significant improvements in permanent magnets over the past decade, improvements in power electronic devices, and the ever increasing need for more efficient machines in electric vehicle systems. In comparison with the cylindrical radial flux motor, the AFPM machine is better in a number of aspects: short frame; compact construction; high efficiency; brushless construction; good starting torque and high-power density. The common modes of failure and typical operating conditions of AFPM machines are discussed further. The focus of this research project is a prototype AFPM machine developed by the Electrical Engineering Department of The University of Stellenbosch. The machine considered has a power rating of 300 kW and an operating efficiency of 95 % at a speed of 2300 rpm. This specific machine is used as an example to illustrate the thermal characteristics of geometrically similar AFPM machines.

The thermal characterization was achieved with the use of two numerical computer models. Firstly a fluid model was specially developed and experimentally verified. The objective of the fluid model was to calculate the mass flow rate of air through any geometrically similar AFPM machine. The fluid model was further used to investigate the effects of different magnet thickness and axial gaps between the stator and the rotor plates on the mass flow rate of air through the machine. The fluid model was verified with experimental testing that was done on a half-scale Perspex model. During the experimental testing the magnet thickness was varied between 2.5 mm, 5.0 mm, and 7.5 mm along with axial gaps of 6.5 mm, 7.5 mm, 8.5 mm, and 9.5 mm. The fluid model showed a correlation to within 10 % of the experimental mass flow rates. The results of these tests showed that the magnet thickness and axial gap between the stator and the rotor plates had no significant effect on the mass flow rate of air. The fluid model was based on one-dimensional, steady-state, and incompressible flow.

The second numerical computer model was a thermal model. This model was used to calculate the transient temperature response of the AFPM machine. The model was based on a two-dimensional transient finite difference solution technique. Experimental temperatures taken from the prototype AFPM machine were used to verify the thermal model. Correlations between the experimental and theoretical temperatures were within 5.8 % of each other. The thermal model was used to investigate the effect of geometrical changes on the temperatures in the AFPM machine. It was found that these geometrical changes had no significant effect on the temperatures in the AFPM machine. It was also established that increasing the air mass flow rate

over about 1 kg/s had no further effect on lowering the temperatures. The stator was also identified as being the most critical component as it reached its maximum temperature limit before any other component. Heat pipes were considered as an alternative thermal management technique. The location of the heat pipe was limited to the stator. Further simulations were done to investigate the effect of the heat pipe properties on the amount of heat removed from the stator.

Recommendations were made concerning the thermal management of the current and possible future prototype AFPM machines. It was recommended that a further more detailed investigation into the use of heat pipes be considered. This recommendation is substantiated by the fact that in this research project only one type of heat pipe was considered and its location was limited to within the stator.

Opsomming

AFPM masjiene het meer aantreklik geword weens betekenisvolle verbeteringe in permanente magnete gedurende die laaste dekade,verbeteringe in elektroniese toestelle en die vraag na meer effektiewe masjiene in elekriese voertuigstelsels. Die AFPM masjien is beter as die Silindriese Radiale Fluksie Motor wat die volgende aspekte betref: die kort raamwerk; kompakte konstruksie; hoë effektiwiteit; borsellose konstruksie; goeie aanvangsdraaimoment; en hoë-krag digtheid. Die algemene vorms van faling en ook die tipiese werkstoestande van die AFPM word verder bespreek. Hierdie navorsingsprojek fokus op die prototipe AFPM masjien wat ontwikkel is deur die Elektriese Ingenieurs Departement van die Universiteit van Stellenbosch. Die masjien onder bespreking wek 300 kW per uur op en is 95% effektief teen 'n spoed van 2300 rpm. Hierdie masjien word gebruik om die termiese kenmerke van geometries-gelyksoortige masjiene te illustreer.

Die termiese eienskappe is bepaal deur die gebruik van twee numeriese rekenaarmodelle. Eerstens is 'n vloeistofmodel spesiaal ontwerp en eksperimenteel geverifieer. Die doel van die vloeistofmodel was om die massa vloeitempo van lug deur enige geometries-gelyksoortige AFPM masjien te bereken. Die vloeistofmodel is verder gebruik om die uitwerking van verskillende magneetdiktes en aksiale gapings tussen die stator en die rotorplate op die massa vloeitempo van lug deur die masjien te ondersoek. Die vloeistofmodel is geverifieer deur eksperimentele toetsing wat gedoen is op 'n halfskaal Perspex model. Tydens die toetsing het magneetdiktes gewissel tussen 2.5 mm, 5.0 mm en 7.5 mm en die aksiale gapings tussen 6.5 mm, 7.5 mm en 9.5 mm. Die vloeistof model het 'n korrelasie van binne 10 % van die eksperimentele massa vloeistempo getoon. Die resultate van hierdie toetse het getoon dat die magneetdiktes en die aksiale gapings tussen die stator en die rotorplate geen noemenswaardige uiterking op die massa vloeitempo van lug gehad het nie. Die vloeistofmodel is gebaseer op een-dimensionele, gestadigde, onsamedrukbare vloei.

Die tweede numeriese model was 'n termiese model. Hierdie model is gebruik om die transiënte temperatuur respons van die AFPM masjien te bereken. Die model is gebaseer op 'n twee-dimensionele , transiënte eindige-verskil oplossingstegniek.
Eksperimentele temperature gemeet op die prototipe AFPM masjien is gebruik om die termiese model te verifeer. Die eksperimentele en teoretiese temperature het binne 5.8% met mekaar gekorrelleer. Die termiese model is gebruik om die uitwerking van geometriese veranderinge op die temperatuur in die AFPM masjien te ondersoek. Daar is gevind dat hierdie geometriese

veranderinge geen noemenswaardige uitwerking op die temperature van die AFPM masjien gehad het nie. Daar is ook vasgestel dat 'n vermeerdering in die lug massa vloeitempo verby 1 kg/s geen verdere uitwerking het op die verlaging van die temperatuur gehaad het nie. Die stator is ge-identifiseer as die mees kritiese komponent aangesien dit sy maksimum temperatuur limiet bereik het voor enige ander komponent, Hittepype is oorweeg as 'n alternatiewe termiese bestuurstegniek. Die plasing van die pype is tot die stator beperk. Verdere simulasies is uitgevoer om die uitwerking van die hittepyp eienskappe op die hoeveelheid hitte wat verwyder word van die stator te ondersoek.

Aanbevelings is gemaak m.b.t die termiese bestuur van die huidige en moontlike toekomstige prototipes van AFPM masjiene. Daar is aanbeveel dat daar in meer besonderhede ondersoek ingestel word na die gebruik van hittepype. Die rede hiervoor is dat daar in hierdie studie net gebruik gemaak is van een tipe hittepyp en dat die plasing daarvan beperk is tot binne die stator.

Dedication

This thesis is dedicated to my loving family. Your kindness, generosity and understanding have, and always will, continue to serve as an example for my friends and myself. To each and every one of you, thank you.

Acknowledgments

To Mr Dobson, thank you for all your enthusiasm, dedication and your unique opinions on life which only made my work all that more enjoyable.

To all the people who contributed to the success of my studies. Thank you.

Contents

Nomenclature

A	area [m^2]
c	specific heat [J/kgK]
C_m	moment coefficient
d	diameter [m]
d	length [m]
f	Darcy friction factor
g	gap width [m]
g	gravitational constant [m/s^2]
G	volumetric flow rate [m^3/s]
G^*	gap ratio
h	convective heat transfer coefficient [W/m^2K]
h_{fg}	latent heat of vaporisation [J/kg]
i	variable
k	energy loss coefficient
k	thermal conductivity [W/mK]
K	wick permeability
l	length [m]
M	frictional moment [Nm]
m	mass [kg]
m	variable
$\dot{m}$	mass flow rate [kg/s]
n	variable
N	variable
Nu	Nusselt number
p	static pressure [Pa]
$\dot{Q}$	heat transfer rate [W]
$\bar{q}$	conduction heat flux vector [W]
r	length [m]
r	radius [m]
r^*	dimensionless radius
Re	Reynolds number
T	temperature [K]
t	time [s]

u	internal energy [J]
V	velocity [m/s]
V	volume [m^3]
$\dot{W}$	rate of work done [W]
x	quality
Z	elevation [m]
z	length [m]

Greek symbols

δ	boundary layer thickness [m]
ν	viscosity [m^2/s]
η	efficiency
ε	emissivity
μ	figure of merit [kW/cm^2]
ω	rotational velocity [rad/s]
σ	surface tension [N/m]
μ	dynamic viscosity [kg/ms]
α	void fraction
ρ	density [kg/m^3]
σ	Stefan-Boltzmann constant [W/m^2K^4]

Subscripts

1,2....	control volume variables
ave	average
cap	capillary
E	east facing
eff	effective
eq	equivalent
int	internal
max	maximum
N	north facing
S	south facing
W	west facing

Superscripts

*	dimensionless variable
m	variable denoting element position
n	variable denoting variable position

Abbreviations and acronyms

AFPM	Axial Flux Permanent Magnet Machine
PV	Photovoltaic
DC	Direct Current
NdFeB	Neodymium-Iron-Boron

List of tables **Page**

List of figures **Page**

1. Introduction and objectives

Axial Flux Permanent Magnet (AFPM) machines have very high power densities. A 300 kW prototype AFPM machine was developed by the Electrical Engineering Department of the University of Stellenbosch. The prototype machine has an outside diameter of 720 mm, the width across the rotors is 82 mm and has a rated power of 300 kW at 2300 rpm. Of the 300 kW approximately 7kW is lost due to eddy current losses in the stator.

This research project considers the thermal management of these machines with the consideration of using heat pipes as a cooling technique. The thermal response of the AFPM machine is determined by the magnitude of the eddy current losses and any external radiation sources. The impact of these heat loads on the operating temperature of the AFPM machine is affected by the thermal characteristics of the materials used in the construction of the AFPM machine. The Electrical Engineering Department of the University of Stellenbosch has been experiencing problems with the operating temperatures in the AFPM machine and approached the Mechanical Engineering Department with regard to the overheating of the stator. It is anticipated that these machines will be used in wind turbines, where the outside rotor diameter will be in the region of 2 m and the machine will have a rotational speed of 200 rpm. The thermal management and control of these machines is an important design consideration.

The prototype AFPM machine is used to demonstrate how these machines should be thermally managed and controlled to attain the desired operating temperatures of the different components for various operating conditions. The thermal management was investigated using numerical computer program models developed during the course of this research project. These models are used to determine the mass flow rate of air through the AFPM machine and the transient temperature response of the components of the AFPM machine. The verification of these models was done with experimental work. Comparisons of different geometries and their effect on the mass flow rate of air and operating temperatures are accomplished using the numerical models, for example, the gap ratio between the stator and the rotor plates that has a significant effect on the convective heat transfer coefficient on the surface of the stator and rotor plates. These comparisons will serve as a means of understanding and interpreting the thermal characteristics of AFPM machines.

Heat pipes present an alternative option to cooling the AFPM machine. Where an insufficient air mass flow rate exists. The numerical program allows the designer to investigate the cooling

effect of a heat pipe as well as to compare different heat pipe thermal properties. Conclusions and recommendations are given to provide insight into future AFPM machine thermal management and control.

2. The Axial Flux Permanent Magnet (AFPM) Machine

This chapter considers the Axial Flux Permanent Magnet (AFPM) machine. A background of the machine is presented as well as its common failure modes and typical operating conditions.

2.1 Background research on AFPM machines

The majority of applications that consume electrical energy use energy produced from non-renewable, greenhouse gas-producing supplies, such as coal and oil. The reduction in greenhouse gas production, in the near future, may not come from the use of renewable energy, but rather from more efficient electricity generation. It was recently reported that 90% of Australia's energy needs were generated by non-renewable sources of energy, such as coal and gas (Chandler and Patterson, 2001). Electric machines are utilized in power generation and consumption. This fact highlights the need for high-efficiency electric motors such as the AFPM machine. In comparison with the cylindrical radial flux motor, the AFPM machine is better in a number of aspects, for instance where a short frame, compact construction and high-power density is required.

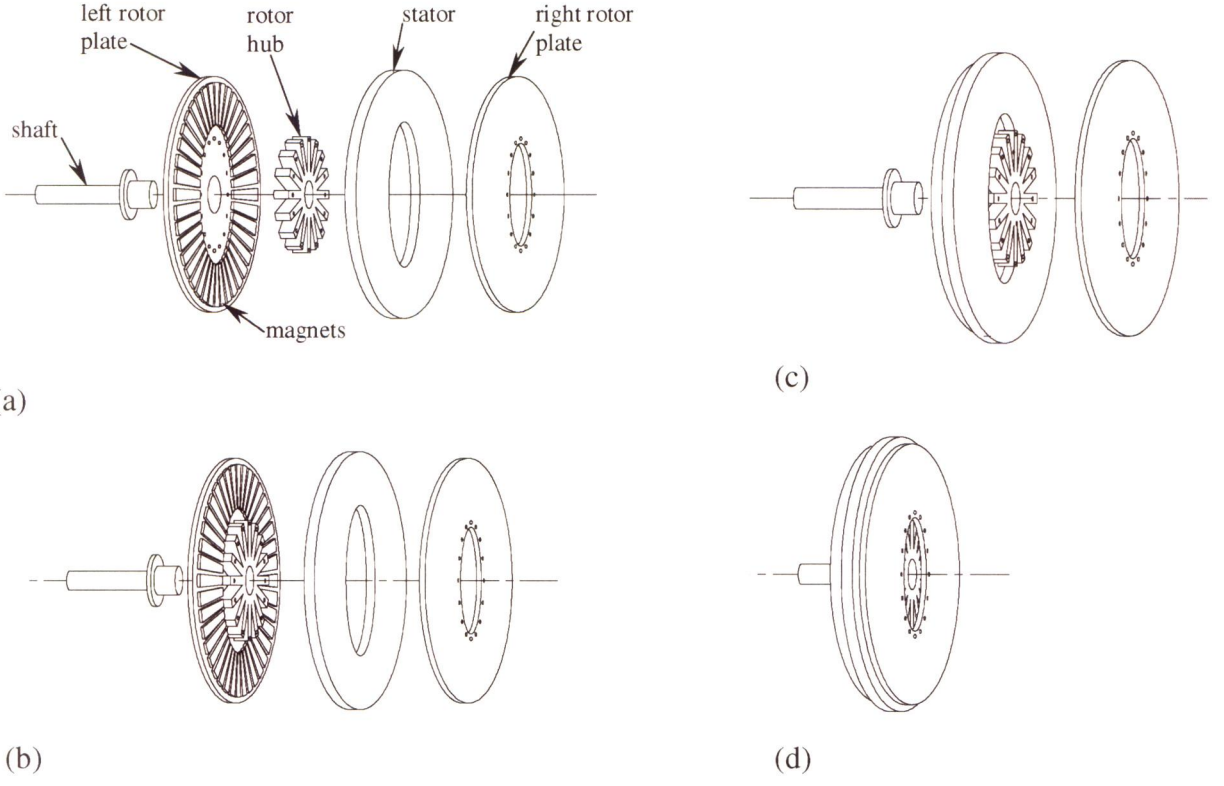

Figure 2.1 Configuration of the AFPM machine (a) Exploded view; (b) Partial assembly of the left rotor plate and the rotor hub; (c) Partial assembly of the left rotor plate, rotor hub and the stator; (d) Complete assembly.

The use of rare earth permanent magnet materials such as Samarium Cobalt ($SmCo_5$) and the recently introduced Neodymium-Iron-Boron (NdFeB) magnets provides higher levels of torque if designed properly (Swamy et al, 1995). Figure 2.1 shows the basic assembly of the prototype AFPM machine. Figures 2.1 (b) to (d) show the assembly of the AFPM machine. The rotor plates and the rotor hub are held together by 16 bolts that extend from the right rotor plate, through the rotor hub and into the left rotor plate. The stator is held in place by an external frame (not shown). The AFPM machine is secured by this frame.

The features of high efficiency, brushless construction and good starting torque have led to an increased demand for these motors in water pumping systems operated by photovoltaic (PV) array (Swamy et al, 1995). The photovoltaic water pumping system consists of a solar cell PV array, MOSFET based inverter and a brushless permanent magnet DC motor coupled to a pump and controller. These motors can successfully pump the water even despite a variation in the input DC voltage due to the variation of solar insolation. The use of these motors in ceiling fans combined with new aerodynamic blades, decreases the power consumption and therefore the electricity charges by a factor of two to three (Schmidt et al, 2001). A 6 kW axial flux brushless DC machine was used as the drive motor for the Fuji Xerox Desert Rose solar racing car. The motor included an adjustable airgap and was capable of driving the car at speeds of above 90 km/h (Chandler et al, 2001).

The prototype machine, see figure 2.2, has a diameter of 860 mm and an axial length of 105 mm. It has a power rating of 300 kW at 2300 rpm and operates at an efficiency of 95% (Wang, 2002) at rated speed and power. The permanent magnets used are made of Neodymium-Iron-Boron (NdFeB) and have a temperature limitation of 149 °C. The coils of the stator are bound together with a composite material, which distorts at temperatures higher than 100 °C. The permanent magnets are located on the surface of the rotor plates.

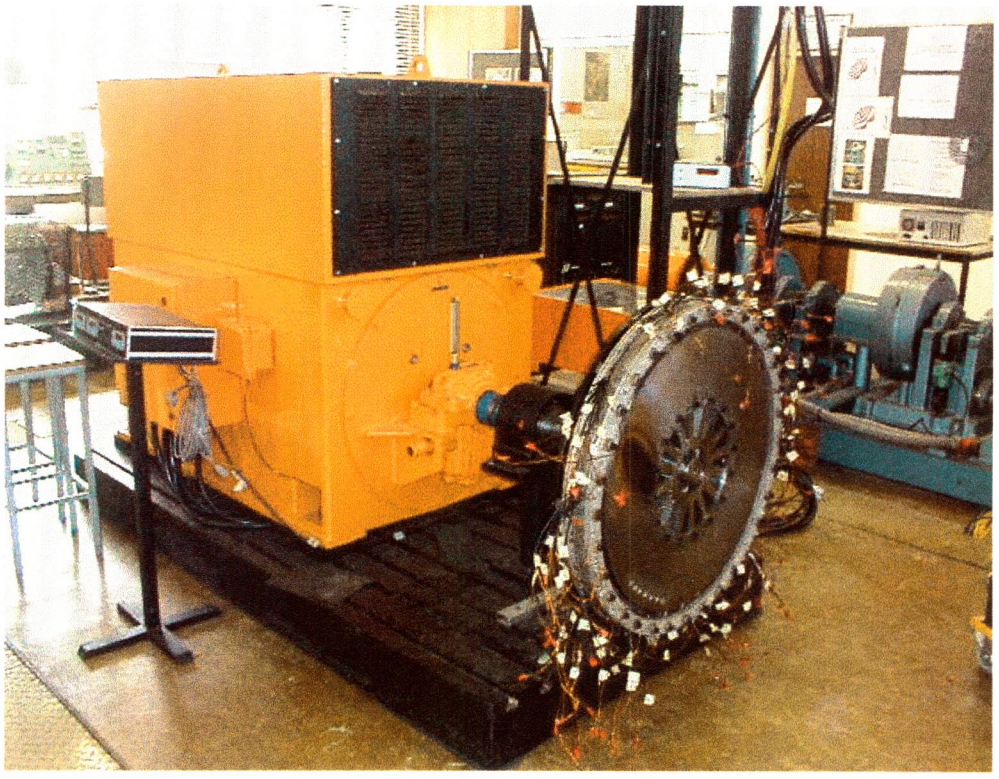

Figure 2.2 The 300 kW AFPM machine.

2.2 Common modes of failure

Typical failure modes of the AFPM machine are listed below

Stator coils:

- Burning of the coils due to high temperatures that are caused by overloads.
- Increase in mechanical strain caused by temperature fluctuations and gradients.

Permanent magnets:

- The performance of the magnets deteriorates due to too high temperature.
- With the temperature of the magnet exceeding the limitation, the magnets can be demagnetised. This demagnetisation is irreversible.
- The permanent magnets are compressed powder and may shear off the rotor plates due to the high centrifugal forces causing catastrophic damage to the AFPM machine.

2.3 Typical operating conditions

Currently the prototype machine is being tested in a large laboratory with no immediate obstructions to the airflow path external to the machine. The operation of these machines may necessitate the machine being enclosed in a shroud to ensure that the warmer air exiting the machine does not return to the inlet. The AFPM machine may be coupled to a diesel or petrol engine, figure A.1, which will have to be considered in the thermal management system. Provision would have to be made for the proper channelling of fresh air from the environment through the machine and back to the environment.

3. Thermo-fluid modelling

In this section the theoretical thermo fluid model is explained. The thermo fluid model consists of two separate parts, namely a thermal model and a fluid model. The fluid model is used to simulate the flow channel through the AFPM machine, the object of which is to determine the air mass flow rate for a given geometry and rotational speed. The thermal model simulates the transient temperature response of the AFPM machine for varying boundary conditions, geometry and internal heat generation.

3.1 Fluid flow model

The fluid behaviour in the AFPM machine is similar to that observed in a centrifugal or radial fan. Air is drawn into the machine by the radial blades of the rotor hub. It is most likely that the inlet will be in the form of a pipe, with fresh air entering from an external source. The air will enter through the inlet pipe in an axial direction and will exit in a radial direction at the outlet of the rotor hub. The air is then forced out into a radial channel as is seen in figure 3.1. The development of the air stream is achieved through the rotation of the rotor hub and the rotor plates. A degree of viscous pumping will also occur. Where viscous pumping is defined as the radial flow between a rotating plate and a stationary plate, neither of which have radial blades.

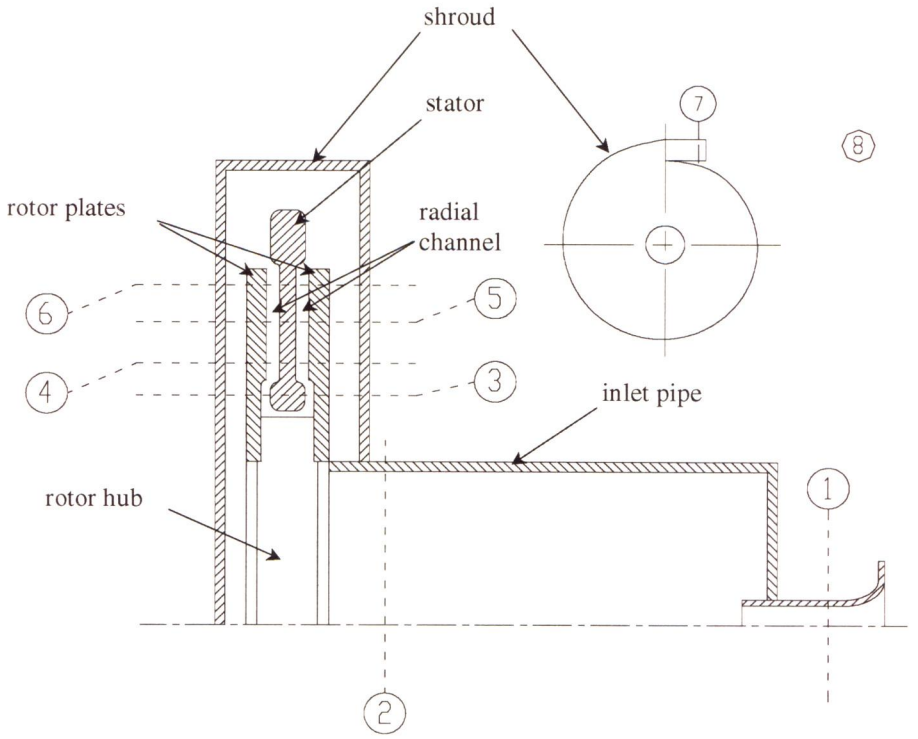

Figure 3.1 Flow channel of the AFPM machine.

3.1.1 Fluid flow channel

The fluid flow channel can be seen in figure 3.1, as well as the locations of the pressure tapings that were made during the experimental work. Calculations for the fluid flow model are based on one-dimensional, steady state, incompressible flow.

The general energy equation for a control volume with one inlet and one outlet, assumed one-dimensional, as shown in figure 3.2 is (Sayers, 1990, p19)

$$\dot{Q}_{in} + \dot{W}_{in} = \dot{m}\left[\left(p_2/\rho_2 - p_1/\rho_1\right) + \left(V_2^2 - V_1^2\right)/2 + g\left(Z_2 - Z_1\right) + \left(u_2 - u_1\right)\right] \tag{3.1}$$

where the subscripts 1 and 2 refer to the inlet and outlet respectively. For steady flow with no heat transfer and ignoring gravity, this equation can be rearranged and reduced to the form

$$\Delta p = p_2 - p_1 = \frac{\rho V_1^2}{2} + \frac{\rho \dot{W}_{in}}{\dot{m}} - k_1 \frac{\rho V_1^2}{2} - \frac{\rho V_2^2}{2} \tag{3.2 a}$$

where the term $k_1 \dfrac{\rho V_1^2}{2}$ describes the irreversible change in energy from potential and kinetic energy into internal energy, based on the average velocity at point 1, that results in an increase in the fluid temperature. Point 8 of figure 3.1 is a point in the atmosphere away from the inlet and outlet, for the purpose of explaining the method let point 0 be a point away from the inlet and point 8 a point away from the outlet. Applying equation (3.2 a) to the section from point 0 to point 1, the following equation is obtained:

$$p_1 - p_0 = \frac{\rho V_0^2}{2} + \frac{\rho \dot{W}_{in}}{\dot{m}} - k_1 \frac{\rho V_1^2}{2} - \frac{\rho V_1^2}{2}$$

This is repeated to each of the remaining sections to give the following equations:

$$p_2 - p_1 = \frac{\rho V_1^2}{2} + \frac{\rho \dot{W}_{in}}{\dot{m}} - k_2 \frac{\rho V_2^2}{2} - \frac{\rho V_2^2}{2}$$

$$p_3 - p_2 = \frac{\rho V_2^2}{2} + \frac{\rho \dot{W}_{in}}{\dot{m}} - k_3 \frac{\rho V_3^2}{2} - \frac{\rho V_3^2}{2}$$

$$p_4 - p_3 = \frac{\rho V_3^2}{2} + \frac{\rho \dot{W}_{in}}{\dot{m}} - k_4 \frac{\rho V_4^2}{2} - \frac{\rho V_4^2}{2}$$

$$p_5 - p_4 = \frac{\rho V_4^2}{2} + \frac{\rho \dot{W}_{in}}{\dot{m}} - k_5 \frac{\rho V_5^2}{2} - \frac{\rho V_5^2}{2}$$

$$p_6 - p_5 = \frac{\rho V_5^2}{2} + \frac{\rho \dot{W}_{in}}{\dot{m}} - k_1 \frac{\rho V_6^2}{2} - \frac{\rho V_6^2}{2}$$

$$p_7 - p_6 = \frac{\rho V_6^2}{2} + \frac{\rho \dot{W}_{in}}{\dot{m}} - k_1 \frac{\rho V_7^2}{2} - \frac{\rho V_7^2}{2}$$

$$p_8 - p_7 = \frac{\rho V_7^2}{2} + \frac{\rho \dot{W}_{in}}{\dot{m}} - k_1 \frac{\rho V_8^2}{2} - \frac{\rho V_8^2}{2}$$

This set of 8 equations combined with the fact that $p_8 = p_0$ leads to the following equation:

$$0 = \sum \frac{\rho \dot{W}_{in}}{\dot{m}} - \sum_{i=1}^{8} k_i \frac{\rho V_i^2}{2} \qquad (3.2\ b)$$

Using the equations given in appendix D, along with equation (3.2 b), the only unknown is the mass flow rate, which is solved by trial and error as shown in section 3.1.2.

3.1.2 Numerical solution method

An interval halving technique is used to find the actual mass flow rate in equation (3.2 b). This method is easily illustrated with help of figure 3.3. The solution method starts with an upper, $\dot{m}_{up}$, and lower, $\dot{m}_{low}$, boundary value for the mass flow rate.

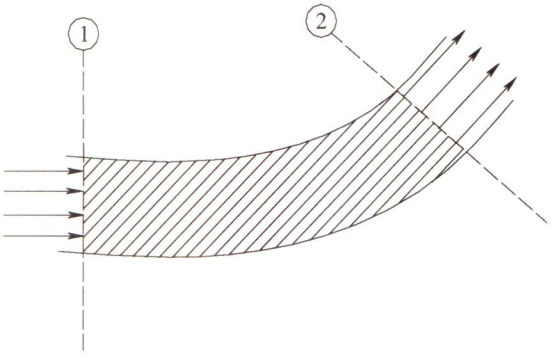

Figure 3.2 Control volume analysis.

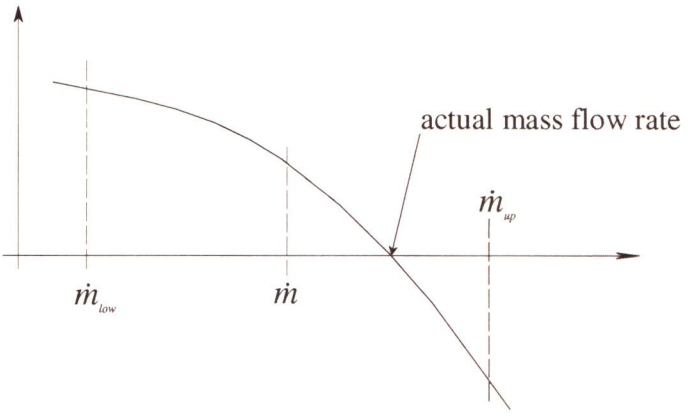

Figure 3.3 Interval halving solution method.

The first mass flow rate used in the solution method is then the average between these boundary values.

$$\dot{m} = (\dot{m}_{up} + \dot{m}_{low})/2 \tag{3.3}$$

From this mass flow rate the pressure at each point is calculated according to the equations given in appendix D. If the calculated pressure at point 8 is higher than 1 atm and point 8 is located away from the exit, then the actual mass flow rate lies between $\dot{m}$ and $\dot{m}_{up}$. For this reason the lower boundary is assigned the value of $\dot{m}$.

$$\dot{m}_{low} = \dot{m} \tag{3.4}$$

If the pressure at point 8 is lower then 1 atm then the actual mass flow rate lies between $\dot{m}$ and $\dot{m}_{low}$. For this reason the upper boundary is assigned the value of $\dot{m}$.

$$\dot{m}_{up} = \dot{m} \tag{3.5}$$

This process is repeated until the mass flow rate is found that gives a pressure of 1 atm at point 8. This is the mass flow rate of air through the AFPM machine.

3.2 Thermal Model

The transient thermal response of the AFPM machine was calculated using a numerical solution method. Numerical solution methods are particularly useful when the shape of the solid to be analysed is irregular or when the thermal properties are temperature and position dependant. This is exactly the case of the AFPM machine. Numerical methods commonly used are the finite-difference method, the finite element method, the control volume method, and to a lesser degree, boundary element approaches to solving the governing thermal equations. The finite-difference method is the most widely used method in thermal analysis. Its popularity is due to the fact that the mathematical concepts of approximating a continuous domain with a network of discrete points (called a mesh) are relatively simple. The partial derivatives of the governing heat conduction equation are replaced by finite differences using the Taylor series. In general, first and second order derivatives are estimated using second-order difference approximations. For these reasons the finite-difference method is used in solving the heat transfer problem of the AFPM machine

3.2.1 The Finite-difference solution method

Figure 3.4 shows the AFPM machine with its respective polar coordinate axes. The AFPM machine has θ symmetry; this is useful as a cross section can be taken through the machine and the subsequent heat transfer equations can be derived for the *z* and *r* axes only.

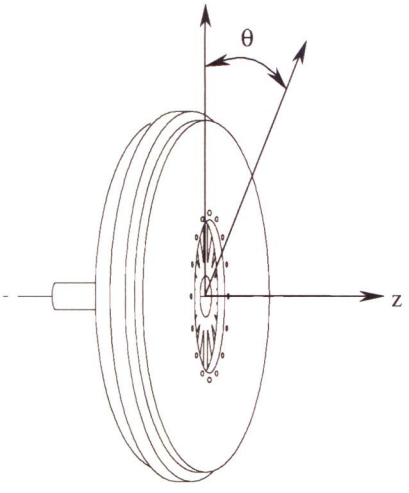

Figure 3.4 Polar coordinate system.

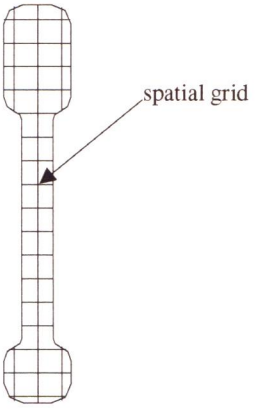

Figure 3.5 Spatial discretization of the stator.

The heat conduction equation is given by Mills (1995) as

$$\bar{q} = -k\nabla T \tag{3.6}$$

Where $\bar{q}$ is the conduction heat flux vector, ∇T is the gradient of the scalar temperature field and k is the thermal conductivity. The first step in the finite-difference method is to discretize the spatial and time coordinates to form a mesh of nodes. Figure 3.5 shows the spatial discretization of the stator. In the next step finite-difference approximations are made to the derivatives appearing in the heat conduction equation to convert the differential equation to an algebraic difference equation. Alternatively, the difference equation can be constructed by applying the energy conservation principle to an elemental volume. The energy conservation principle is given by (Mills, 1995, p 4)

$$\Delta U = \dot{Q}\Delta t + \dot{Q}_v\Delta t \tag{3.7}$$

Where ΔU is the change in internal energy, Δt is the time interval, $\dot{Q}$ is the nett heat transfer into the system and $\dot{Q}_v$ is the total internal heat generated within the system. Consider the spatially discretized grid, figure 3.6, where a finite control volume surrounds the node (m,n) within the solid. The control volume has dimensions of Δr by Δz and depth Δd.

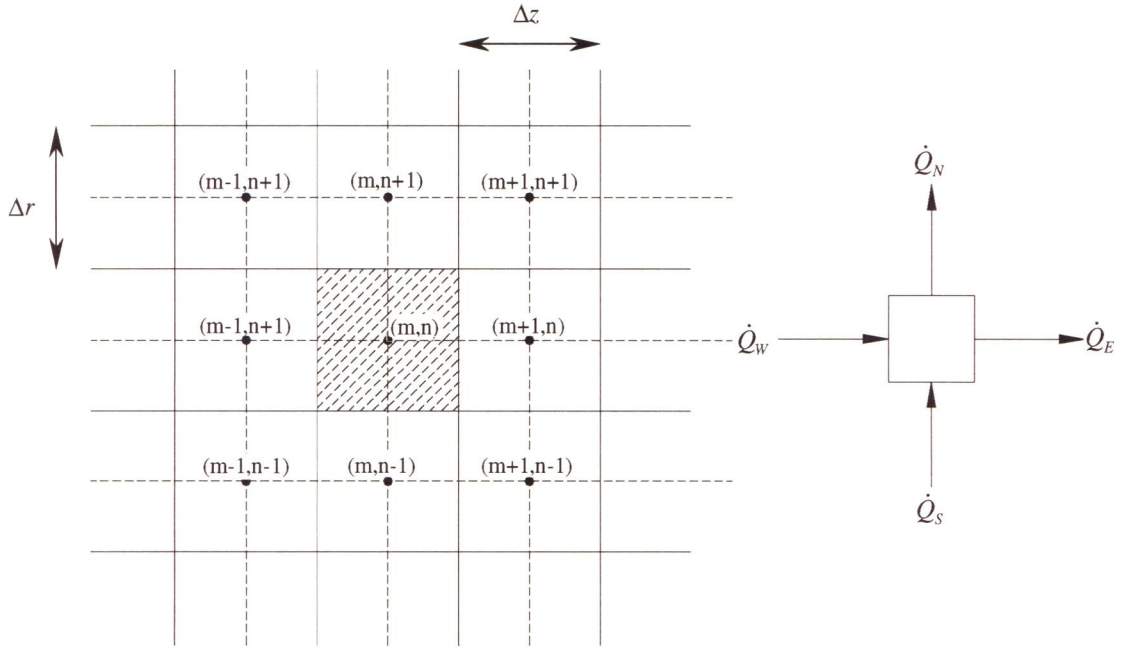

Figure 3.6 Finite control volume Δr by Δz by Δd surrounding node (m,n).

The increase in internal energy from time step i to step $(i+1)$, assuming isotropic materials, is

$$\Delta U = \rho c\left(\Delta z \cdot \Delta r \cdot \Delta d\right)\left(T_m^{i+1} - T_m^i\right) \tag{3.8}$$

For convenience the faces of the element are denoted with the use of compass directions (N, S, E and W). The conduction over the time interval Δt, with directions as in figure 3.6, is

$$\dot{Q}_N \Delta t = -k(\Delta z \cdot \Delta d)\frac{T^i_{m,n+1} - T^i_{m,n}}{\Delta r}\Delta t \tag{3.9}$$

$$\dot{Q}_W \Delta t = -k(\Delta r \cdot \Delta d)\frac{T^i_{m,n} - T^i_{m-1,n}}{\Delta z}\Delta t \tag{3.10}$$

$$\dot{Q}_S \Delta t = -k(\Delta z \cdot \Delta d)\frac{T^i_{m,n} - T^i_{m,n-1}}{\Delta r}\Delta t \tag{3.11}$$

$$\dot{Q}_E \Delta t = -k(\Delta r \cdot \Delta d)\frac{T^i_{m+1,n} - T^i_{m,n}}{\Delta z}\Delta t \tag{3.12}$$

where the heat fluxes have been evaluated at time step *i*. Substituting equations (3.8 to 3.12) into equation (3.7), dividing by Δt and rearranging gives

$$T^{i+1}_{m,n} = T^i_{m,n} + \frac{\Delta t}{\rho c(\Delta z \cdot \Delta r \cdot \Delta d)}\left(\dot{Q}_W + \dot{Q}_S - \dot{Q}_N - \dot{Q}_E + \dot{Q}_{\text{int}}\right) \tag{3.13}$$

where Q_{int} is the internal heat generated for this element. In this explicit method, no iteration is required. Using the given initial temperatures at time $t = 0$, $T^0_{m,n}$, the new temperatures, $T^1_{m,n}$, can be calculated. This process is repeated, marching forward in time. Although simple, the explicit method does have a major drawback: the allowable size of the time step is limited by stability requirements.

3.2.2 Heat transfer modes

Evaluation of the heat transfer coefficients is an integral part of the thermal model. Assumptions made concerning the thermal model are outlined below and discussed in more detail in appendices C and E.

Radiation

The analysis of radiation exchange between real surfaces is based on the diffuse gray surface model. Due to the complexity of calculating the form factor between any two arbitrarily aligned surfaces, the radiation exchange within the AFPM machine was modelled with a simpler approach. The surfaces within the AFPM machine are seen to be relatively large and within close proximity of each other. Consider the radiation exchange between the surface of the magnets and the stator as shown in figure 3.7. In the method used an average temperature of all the elements on the magnets, T_m, and those on the stator, T_s was calculated at each time step. The form factor between these discs was taken to be unity. This approximation of the form factor is justified if

one considers that there is not much opportunity for any radiation to 'escape' out at the sides between the discs. The total radiation exchange between the two surfaces is given by

$$\dot{Q}_{sr} = \frac{\sigma\left(T_s^4 - T_m^4\right)}{\frac{1-\varepsilon_s}{\varepsilon_s A_s} + \frac{1}{A_s F_{sm}} + \frac{1-\varepsilon_m}{\varepsilon_m A_m}} \tag{3.14}$$

where σ is the Stefan-Boltzmann constant, ε is the emissivity of the surface, A is the surface area, and F_{sm} is the form factor between the stator and the magnets (equal to unity). The subscripts s and m refer to the stator and rotor plate respectively. The radiation exchange per element on the surface of the stator is given by

$$\dot{Q}_s = \frac{\dot{Q}_{sr}}{N_s} \tag{3.15}$$

where N_s is the number of elements on the surface of the stator. The radiation exchange per element on the surface of the magnets is given by the same equation except that the subscript s is replaced with m.

Convection

Within the AFPM machine there are different types of convective heat transfer coefficients that must be accounted for. The rate of heat transfer by convection is a function of surface geometry and temperature, the air temperature and velocity and the air thermo physical properties. The two rotating rotors also play a role in the cooling of the AFPM machine. Each convective heat transfer coefficient must be accurately determined through theoretical and experimental investigation. The convective heat transfer coefficients on the surface of the rotor plates and the stator are evaluated as follows:

- Heat transfer from the surface of the rotor plates

There is forced flow, otherwise known as superposed flow, between the rotor plates and the stator. The convective heat transfer coefficient is dependant on the distance between the rotor and the stator and the rotational speed of the AFPM machine. Obtaining a theoretical value for this convective heat transfer coefficient is difficult and often involves the solution of the Navier Stokes equations. Considering the scope of this research project it was decided to use experimental data from the literature. A case study was used in which the experimental setup was similar to that found in the AFPM machine. This case study is shown in detail in appendix E. The resulting correlation for the local Nusselt number on the surface of the rotor is given by equation E.14 and is repeated here for convenience

$$Nu(r^*, G) = a + br^* + cr^{*2} + dG + eG^2 + fr^*G + gr^*G^2 + hr^{*2}G + ir^{*2}G^2$$

where r^* is the dimensionless radius, G is the volumetric flow rate and the values of the constants *a, b, c, d, e, f, g, h, i* are given in table E.1.

- Heat transfer from the surface of the stator

The convective heat transfer coefficient on the surface of the stator is dependant on the peripheral Reynolds number and the gap ratio between the rotor and the stator. A case study was used to establish a correlation for this convective heat transfer coefficient. The local Nusselt number as a function of the gap ratio and the peripheral Reynolds number is given by equation E.13 and is repeated here for convenience.

$$Nu = 9.83 \cdot 10^{-3} (r/b)^{-0.28} \cdot \mathrm{Re}^{0.755}$$

Conduction

The magnets and the rotor hub of the AFPM machine do not exhibit θ symmetry and were therefore modelled by an equivalent solid disc. The solid discs used to model these components consisted of air and the respective materials that the components were manufactured from. For this reason the thermal properties of these solid discs were compensated for according to the following equations. A void fraction for each element is calculated by

$$\alpha = \frac{V_{steel}}{V_{air} + V_{steel}} \tag{3.16}$$

where V_{steel} is the volume of steel in the element and V_{air} is the volume of air. An equivalent conductivity for each element is given by

$$k_{eq} = \alpha k_{steel} + (1-\alpha) k_{air} \tag{3.17}$$

The specific heat must be calculated on a mass basis and a quality fraction for an element in the magnets is defined as

$$x = \frac{m_{steel}}{m_{steel} + m_{air}} \tag{3.18}$$

The specific heat for an element in the magnets is given by

$$c_p = x c_{p,steel} + (1-x) c_{p,air} \tag{3.19}$$

When conduction occurs between dissimilar materials, for instance between the shaft and the rotor hub or the magnets and the rotor plates, the conduction coefficient between elements on either side of this interface is determined by

$$k_{eq} = \frac{(k_1 \Delta z_1 + k_2 \Delta z_2)}{\Delta z_1 + \Delta z_2} \tag{3.20}$$

where the subscripts *1* and *2* refer to the different elements and Δz refers to the length or height of the element depending on in which direction the conduction takes place.

3.2.3 Thermal characterization of the AFPM machine

In order to investigate the effect of different geometrical and physical conditions on the temperature response of the AFPM machine the operating conditions were varied accordingly. The effects of changing the operating conditions were all compared to one base case, as summarised in table 3.1. The stator is the only component that produces heat. The copper wires that are embedded in the stator generate the heat. This and the fact that the stator has the lowest limiting temperature, 100 °C, is the reason that the stator was the first component to reach its limiting temperature. The copper wires are most densely populated at the inner radius of the stator, which was also found to be the point of maximum temperature in the stator (see figure 3.8).

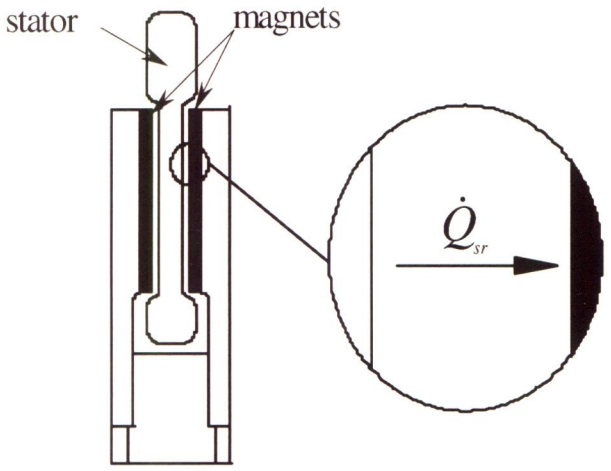

Figure 3.7 Radiation exchange between the magnets and the stator.

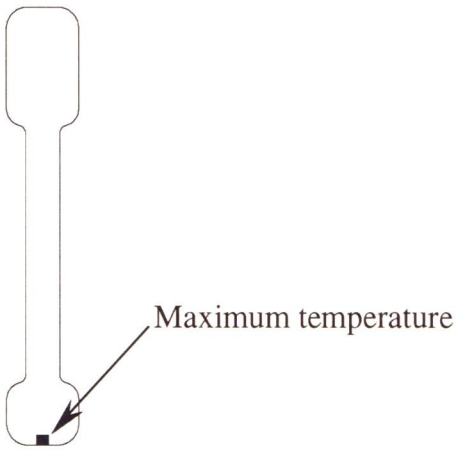

Figure 3.8 Position of the maximum temperature within the stator.

Table 3.1 Base case values

Criteria	Value
Rotational speed [rpm]	2300
Internal heat generation [kW]	7
Emissivity	0.9
Shroud	Yes
Heat pipe	No
Gap ratio, G^*	0.0123
Surrounding air temperature [K]	293
Inlet air temperature [K]	293

As described in section 3.2.1 the transient response of the AFPM machine is calculated by applying equation 3.13 to each of the elements in the model. Figure 3.9 shows the transient response of the base case. At the time of publication the prototype AFPM machine had been tested only once. In this test the rotational speed was 1500 rpm and the total stator internal heat generation was approximately 6 kW. Four thermocouples were placed at the internal radius of the stator, as shown in figure 3.8. After 30 minutes the equilibrium temperature at this point was 355 K. This was an average temperature taken from all four thermocouples. This test result was used to experimentally verify the thermal model of the AFPM machine. The same operating conditions were used in the thermal model and the corresponding temperature obtained from the model was 373.7 K, which shows a difference of 5.8 % from the experimental value. Figure 3.10 shows the calculated transient response for this condition along with the experimental response of the stator. A further transient response simulation was done where the internal heat generated in the stator was switched off after 2000 seconds (see figure 3.11). This simulates the machine from start up, to the point where thermal equilibrium is reached and the internal heat generation is turned off and the temperatures return to their initial values.

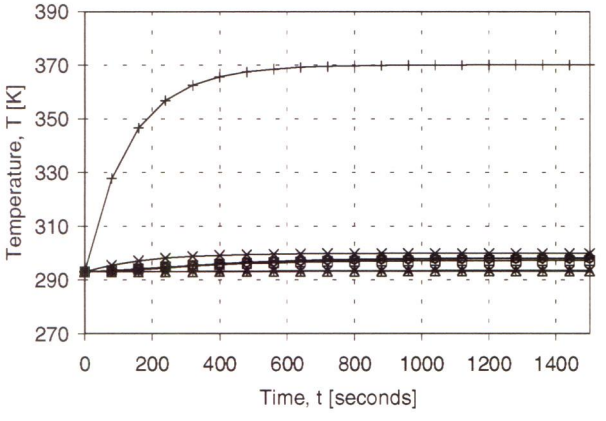

Figure 3.9 Transient response for the base case.

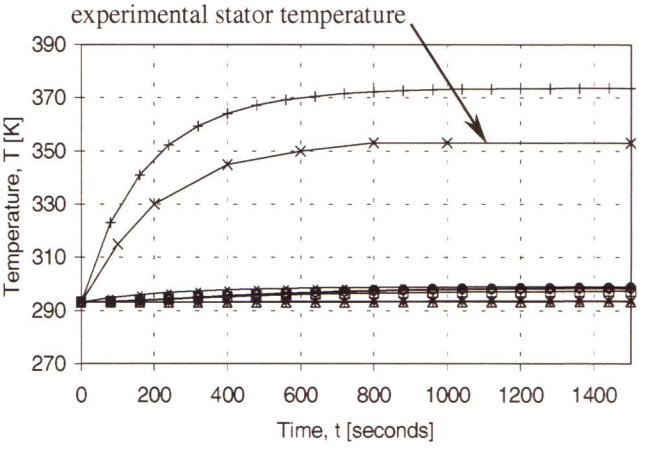

Figure 3.10 Experimental verification of the thermal model.

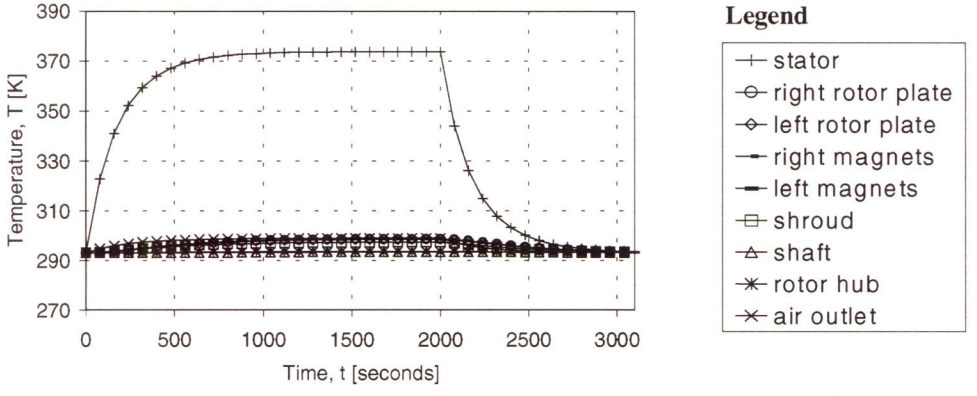

Figure 3.11 Transient response for start up and cooling of the AFPM machine.

Further simulations were done, using the thermal model, where six different characteristics of the AFPM machine were changed and the effect of these changes investigated. The characteristics investigated are discussed in the following sections.

Gap ratio

The convective heat transfer coefficients on the surface of the stator and the rotor plates are dependant on the gap ratio. The gap ratio will have an effect on how much heat is lost from the stator by convection, and ultimately on the maximum temperature in the stator. This effect was investigated using the thermal model. A constant mass flow rate of 0.5 kg/s was used with varying gap ratios (figure 3.12). The gap ratio was varied from 0.00137 to 0.02739, which corresponds to axial gaps between the rotor plates and the stator of 0.5 mm to 10 mm and average convective heat transfer coefficients of 297.1 W/m^{2}K to 141.9 W/m^{2}K respectively. From the results it is clear that there is a non-linear relationship between the gap ratio and the maximum stator temperature.

The effect of the gap ratio for different mass flow rates is shown in figure 3.13. The gap ratios shown are 0.00822, 0.01232 (base case) and 0.01918, which correspond to axial gaps of 3 mm, 4.5 mm and 7 mm and average convective heat transfer coefficients of 189.3 W/m^{2}K, 171.5 W/m^{2}K and 154.4 W/m^{2}K respectively. The solid horizontal line in figure 3.13 is 373 K (100 °C), which is the distortion temperature of the stator. From figure 3.13 it can be seen that increasing the mass flow rate above 1 kg/s has no significant effect on the maximum temperature of the stator.

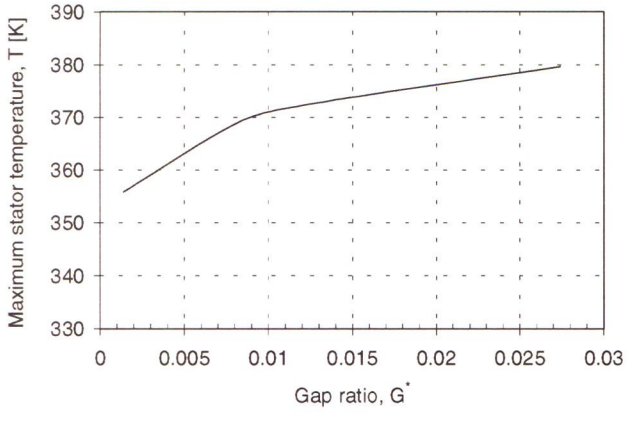

Figure 3.12 The effect of gap ratio on the maximum stator temperature.

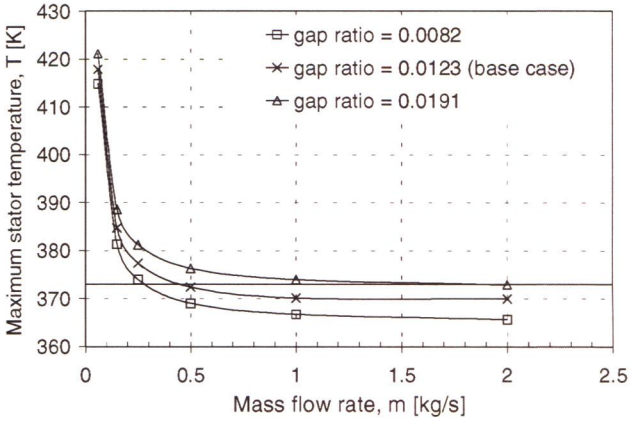

Figure 3.13 The effect of gap ratio on the maximum stator temperature for different mass flow rates.

Shroud

Radiation and convection occurs between the shroud and the AFPM machine as well as between the shroud and the external environment. The convection on the inside of the shroud is forced convection, whereas that on the outside is natural convection. The shroud was modelled to be 10 mm thick and constructed from steel. Figure 3.14 shows the effect of using a shroud (base case), compared to the current situation where there is no shroud around the AFPM machine.

Emissivity

The emissivity of the materials used in the AFPM machine can be changed by treating the component surfaces with special paints. This can effect the final temperature in all of the components. For the base case the emissivity is assumed to be 0.9 for all the surfaces. Two additional simulations were done where the emissivity of all the surfaces was changed to values of 0.2 and 0.5. The effect of changing the emissivity is shown in figure 3.15. It was found that lower values of emissivity led to higher temperatures in the stator.

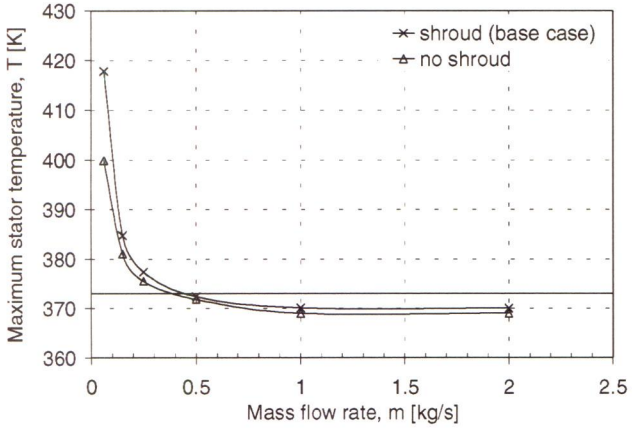

Figure 3.14 The effect of a shroud on the maximum stator temperature.

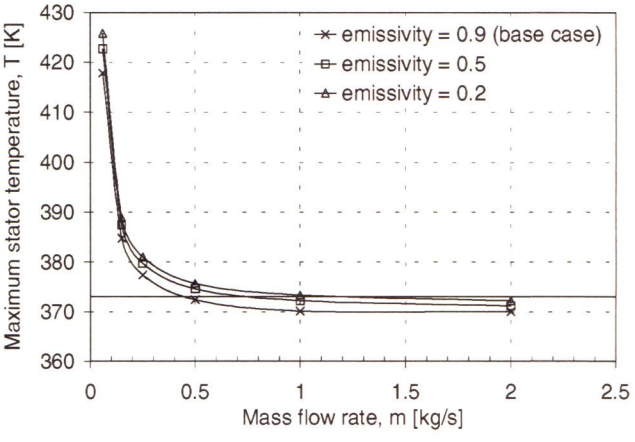

Figure 3.15 The effect of different emissitivities on the maximum stator temperature.

Surrounding air temperature

Depending on the location of the AFPM machine, the surrounding air temperature can vary significantly. To investigate this effect simulations were done where the surrounding temperature was changed between 273 K, 293 K (base case) and 323 K while the inlet air temperature was kept constant at 293 K. The results are shown in figure 3.16 where it can be seen that the change in surrounding temperature has no significant effect on the maximum temperature in the stator.

Inlet air temperature

The inlet air temperature to the AFPM machine will vary depending on the location of the machine and will therefore affect the temperature field of the AFPM machine. Simulations were done where the inlet air temperature was changed between 273 K, 293 K (base case) and 323 K while the surrounding air was kept constant at 293 K. From the results of the simulations (figure 3.17) it is clear that the inlet air temperature has a significant effect on the maximum temperature of the stator.

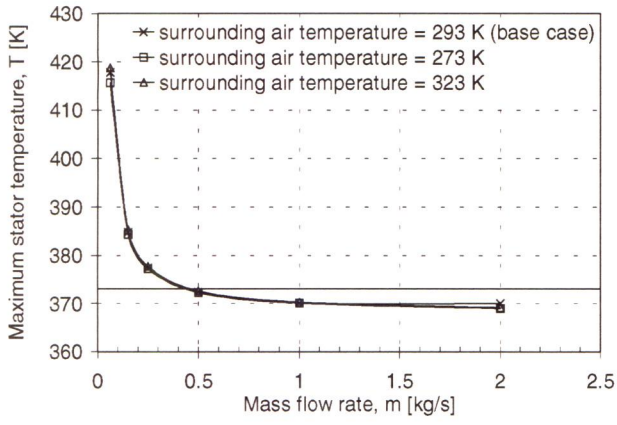

Figure 3.16 The effect of the surrounding air temperature on the maximum stator temperature.

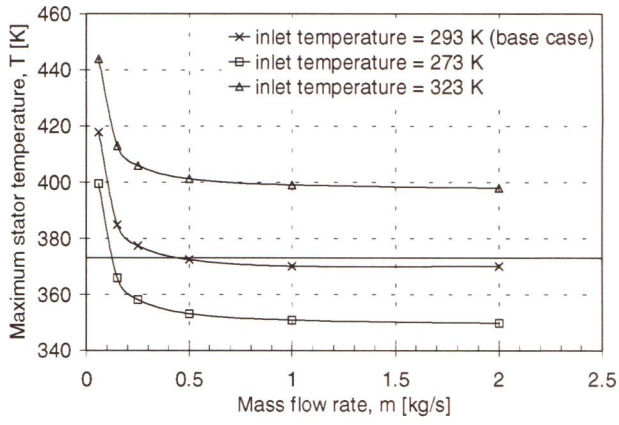

Figure 3.17 The effect of the inlet air temperature on the maximum stator temperature.

Heat pipe

Cooling the AFPM machine purely by air may not be sufficient to keep critical components, such as the stator, from exceeding the limiting temperatures. Increasing the mass flow rate of air above 1 kg/s has no significant effect on the final temperature of the stator, as can be seen in the above results. A heat pipe presents an alternative means to remove the heat from the AFPM machine. The heat pipe in the AFPM machine was modelled as explained in section G.8 of appendix G. It was assumed that the heat pipe was configured as shown in figure 3.18. In this configuration the heat removed by the heat pipe is dumped back into the atmosphere through the use of a finned surface. The finned surface is cooled by air moving over the fins, which is kept at the same temperature as the air entering the AFPM machine.

The first aspect of the heat pipe that was considered was the position of the heat pipe within the stator. Three possible locations of the heat pipe were investigated using the thermal model. These locations are shown in figure 3.19.

A - The inner radius of the stator

B - The mid radius of the stator

C - The outer radius of the stator

For these simulations the heat pipe diameter was kept constant, at 10 mm, and the convective heat transfer coefficient on the inside of the heat pipe was 1000 W/m^2K.

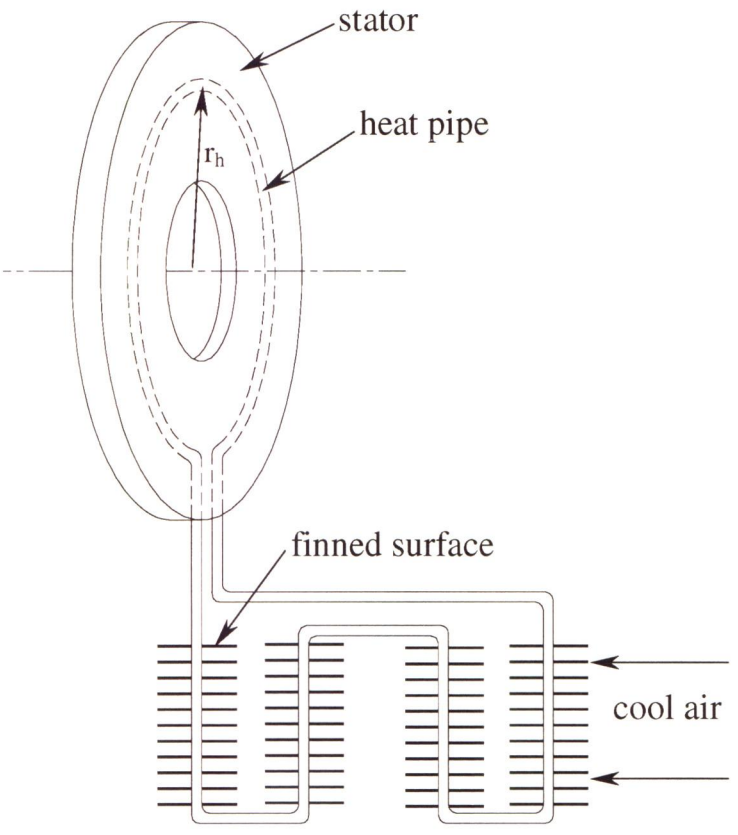

Figure 3.18 Configuration of the heat pipe.

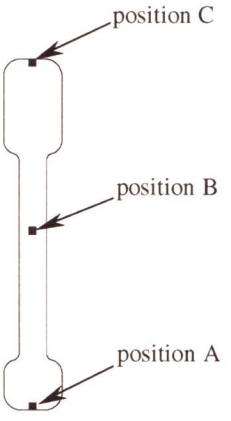

Figure 3.19 Possible locations of the heat pipe within the stator.

Depending on the position of the heat pipe within the stator, the surface area whereby heat is transferred from the stator to the heat pipe will vary. For the three positions being considered the associated areas are listed in table 3.2.

Table 3.2 Exposed area of the heat pipe within the stator for each position

Position	r_h [m]	Area [m^2]
A	0.216	0.04263
B	0.318	0.06277
C	0.420	0.0829

Where r_h is the radius of the heat pipe within the stator (see figure 3.18). The results for the three positions are shown in table 3.3. For these simulations the heat pipe diameter was kept constant (10 mm) and the convective heat transfer coefficient on the inside of the heat pipe was 1000 W/m^2K. The finned surface consisted of aluminium annular fins, with an outside radius of 20 mm and the total length of the finned section was 1.6 m. The fin efficiency was 95 % and had a total exposed fine area of 1.873 m^2. From the results shown, the most heat was removed by the heat pipe when it was positioned at B, although position A yielded the lowest temperature. For subsequent simulations the heat pipe was positioned at A.

Table 3.3 Results for the three different positions of the heat pipe within the stator

Position	Heat removed by the heat pipe [W]	Maximum temperature in the stator [K]
A	1055	345.31
B	1153	364.9
C	890	370.8

The properties of the heat pipe play an important role in the amount of heat that is removed from the stator. It is important that these properties and their sensitivities are known. The first property that was investigated was the diameter of the heat pipe. Simulations were done where the diameter of the heat pipe was varied from 2 mm to 15 mm. Figure 3.20 shows the maximum temperature in the stator and the heat that is removed by the heat pipe for varying diameters.

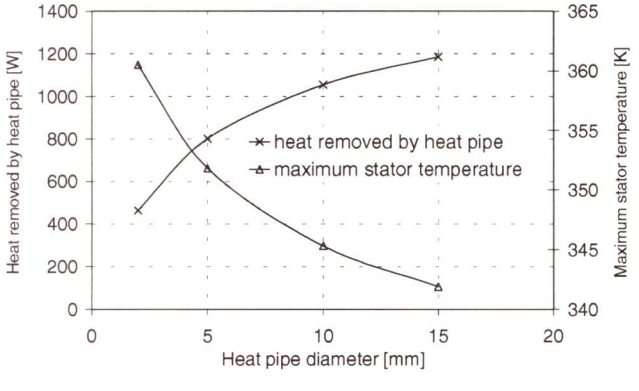

Figure 3.20 The effect of different diameter heat pipes on the maximum stator temperature and the heat removed by the heat pipe.

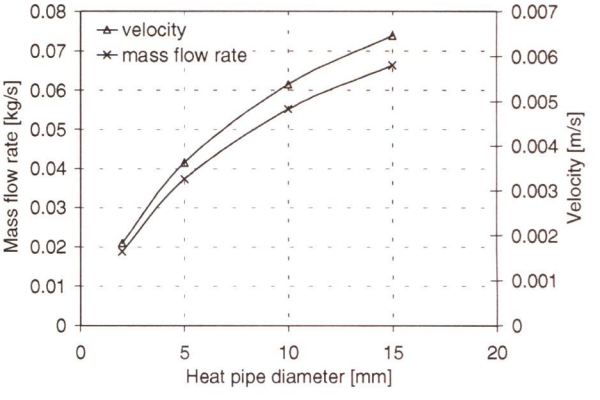

Figure 3.21 Required mass flow rate and associated axial velocity for different diameter heat pipes.

With the heat removed by the heat pipe known, it is possible to calculate the required mass flow rate of water in the heat pipe to remove this heat. Figure 3.21 shows the required mass flow rates and axial velocities associated with the varying diameter. The pressure drop over the heat pipe can be found from the mass flow rate and diameter of the heat pipe (see figure 3.22). The calculations were based on a total heat pipe length of 3 m.

The convective heat transfer coefficient on the inside surface of the heat pipe can vary depending on the geometry of the pipe used. Simulations were done where the convective heat transfer coefficient was varied from 200 W/m^{2}K to 2000 W/m^{2}K (see figure 3.23).

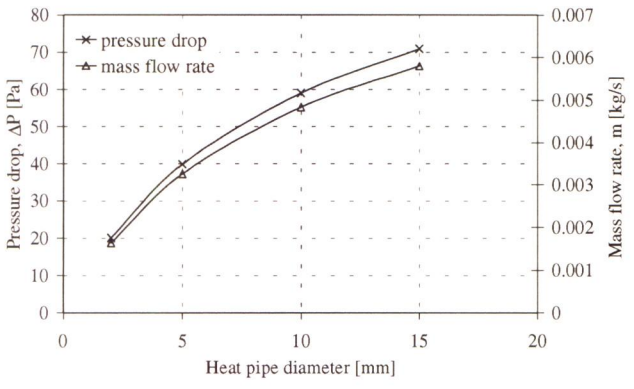

Figure 3.22 Pressure drop over the heat pipe for different diameters.

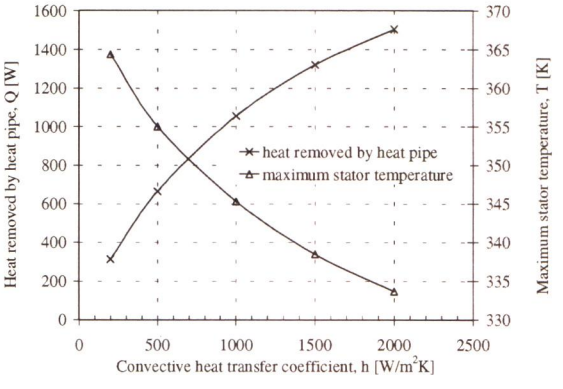

Figure 3.23 Effect of different convective heat transfer coefficients on the heat removed by the heat pipe and the maximum stator temperature.

Figure 3.24 shows a comparison of the base case to the case where a heat pipe is used for different mass flow rates of air through the AFPM machine. The heat removed by the heat pipe is also shown. As can be seen the use of a heat pipe has a significant effect on the maximum temperature in the stator, reducing it from 372 K to 345 K.

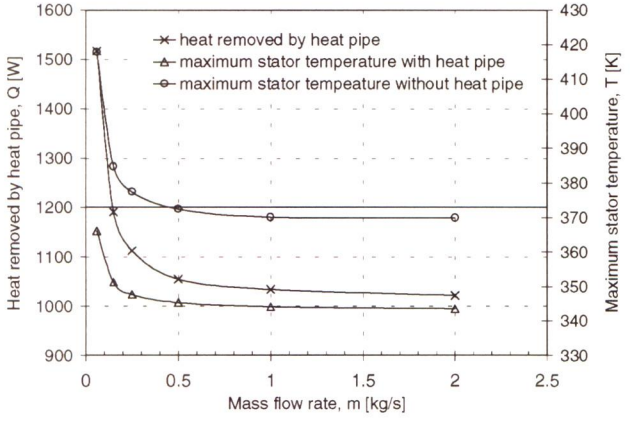

Figure 3.24 The effect of using a heat pipe for different mass flow rates.

4 Experimental set up and results

For the experimental work a half scale model of the AFPM machine was constructed. The model differed from the AFPM machine in that the model had a shroud and the AFPM machine had no shroud. The current AFPM machine is standing in a benign environment and did not necessitate a shroud. The assembly drawing as well as the detailed drawings of the model can be seen in appendix F. One of the objectives of the experimental work was to investigate the effect of the magnet thickness and axial gap between the magnets (rotor plates) and the stator on the mass flow rate of air through the machine. The magnets are situated on the periphery of the rotor plates and in the case of the Perspex model the magnets are held in place by screws. Three different magnet sizes were constructed with thicknesses of 2.5 mm, 5 mm and 7.5 mm. The axial gap between the magnets (rotor plates) and the stator was varied by placing different sized spacers between the rotor plates and the rotor hub. Three different sized spacers were constructed and had thicknesses of 1.2 mm, 2 mm and 3 mm. Figure 4.4 shows the position of the magnets and the spacers in the experimental set up. Different combinations of magnets and spacers were used during the experimental procedure.

4.1 Experimental set up

The experimental set up is shown in figure 4.1. The model of the AFPM machine was driven by an electric motor. The pressure readings were made with the use of a Betz manometer (model no. 11904DGK and serial number 164402). An inlet pipe was connected to the inlet of the AFPM model and a bellmouth was attached to the pipe to measure the flow rate. Figure 4.2 shows a picture of the AFPM model without the inlet pipe. A cellphone is stuck on the outside of the shroud to indicate the scale. It is possible to see the radial blades of the rotor hub, the magnets attached to the rotor plate, the stator and the points where the pressure tappings in the stator exit the stator and then go out through the shroud.

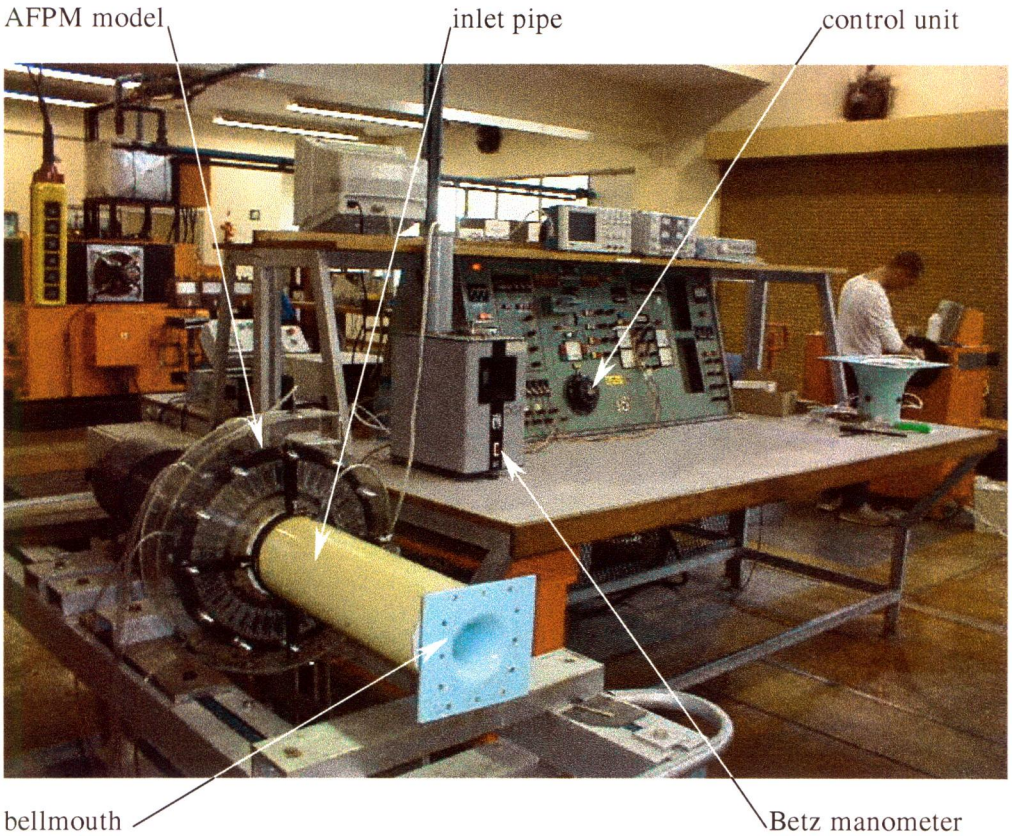

Figure 4.1 Experimental set

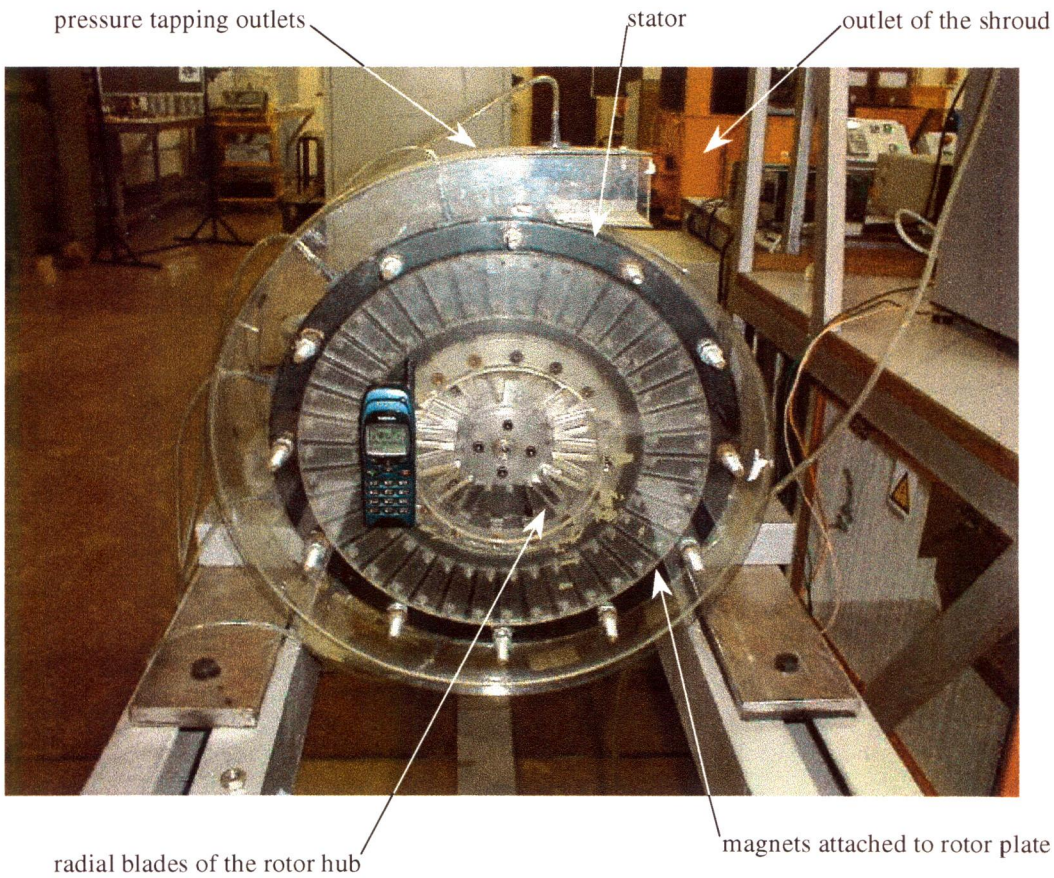

Figure 4.2 The AFPM model

Pressure tappings were made at various locations, figure D.1. The stator was constructed from wood which allowed pressure tappings to be made at radii of 115 mm, 132.5 mm 152.5 mm and 170 mm . The pressure tappings were constructed by drilling a hole from the top of the stator and then one from the side, this is illustrated in figure 4.3. Each of the rotor plates had 40 magnets attached to it. The magnets were interchangeable thus allowing magnets of different thicknesses to be used. The spacing between the rotor plates and the stator was changed by placing spacers of different thicknesses between the rotor hub and the rotor plates (see figure 4.4). In total there were three different variables at which testing was done. They were as follows:

1. Rotor speeds, [rpm]
2. Stator-Rotor clearance gap, [mm]
3. Permanent Magnet thickness, [mm]

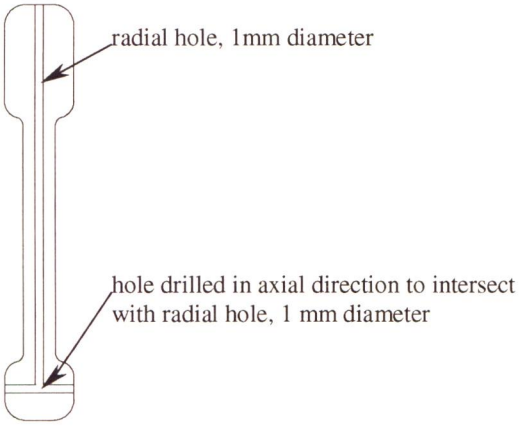

Figure 4.3 Pressure tappings in the stator.

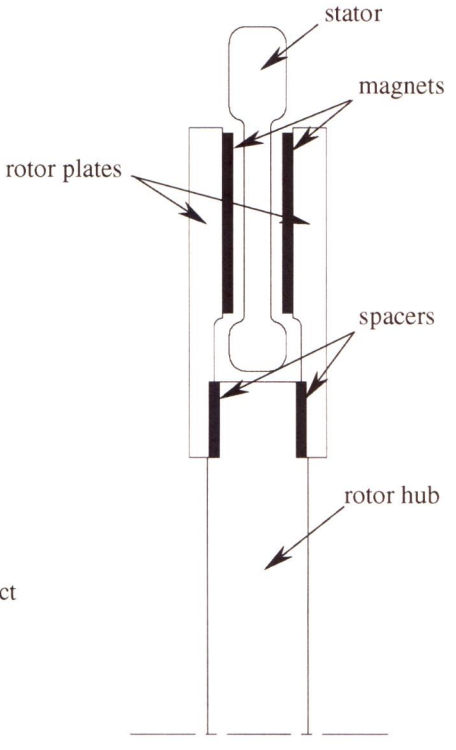

Figure 4.4 Position of the magnets and spacers.

For each possible combination of variables the pressure distribution was measured and the mass flow rate calculated. For each set up the speed was varied from 200 rpm to 2300 rpm, a minimum of 5 different speeds was tested within the range. In total 65 tests were carried out. In each test 7 different pressures were measured at locations as shown in figure D.1. This gave a total of 455 pressure measurements.

4.2 Experimental results

Figure 4.5 shows a graphical interpretation of one of the tests done on the AFPM model. For this test there were no magnets attached to the rotor plates and there was no spacer between the rotor hub and the rotor plates. Readings of the pressures were taken at each of the locations with the use of the Betz manometer while the speed was kept constant at 2100 rpm. With the experimental pressure readings obtained, the fluid flow model was used to calculate the corresponding theoretical pressures at each of the locations; these pressures were plotted against each other for each location. The fluid flow model is explained in more detail in Appendix D. Three further cases are illustrated in figures 4.6 to 4.8. The pressure readings at low rotational speeds was difficult as the pressures were low and not easily read off the Betz Manometer. This resulted in a resolution problem as shown in figure 4.7. Each of these figures illustrates some of the typical results obtained for different magnet thicknesses, spacer thicknesses and rotational speeds.

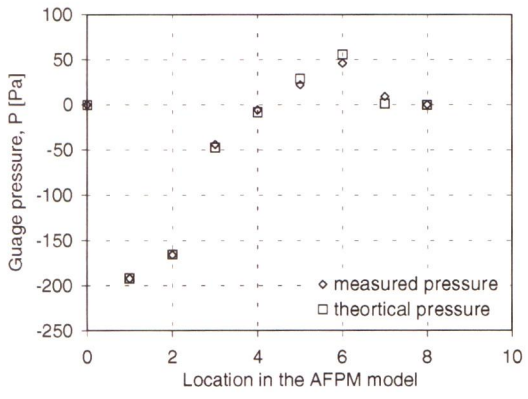

Figure 4.5 Comparison of theoretical and measured pressures for no magnets, no spacer and rotational speed of 2100 rpm.

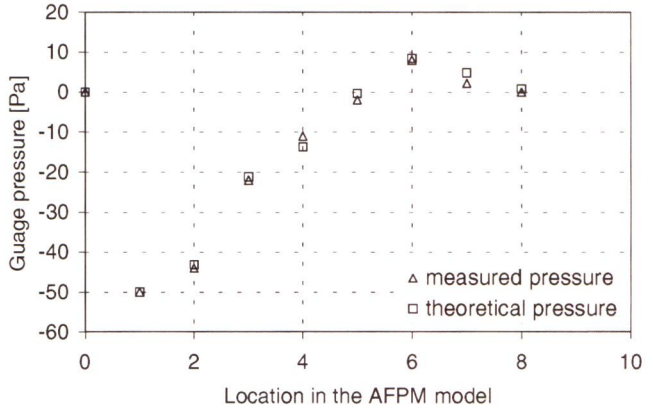

Figure 4.6 Comparison of theoretical and measured pressures for the 2.5 mm magnets, 2 mm spacer and rotational speed of 953 rpm.

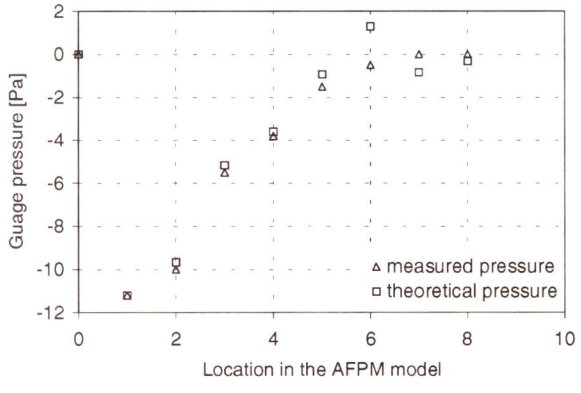

Figure 4.7 Comparison of theoretical and measured pressures for the 5.5 mm magnets, 3 mm spacer and rotational speed of 426 rpm.

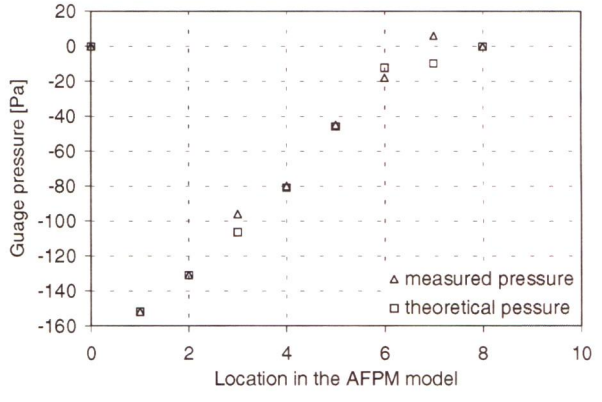

Figure 4.8 Comparison of theoretical and measured pressures for the 7.4 mm magnets, 3 mm spacer and rotational speed of 1438 rpm.

The combined data of all the tests are shown in figures 4.9 and 4.10. Figure 4.9 shows a comparison of the measured pressures with the theoretical pressures for all the tests conducted. Figure 4.10 shows the comparison of the theoretical and measured mass flow rates for all the tests conducted.

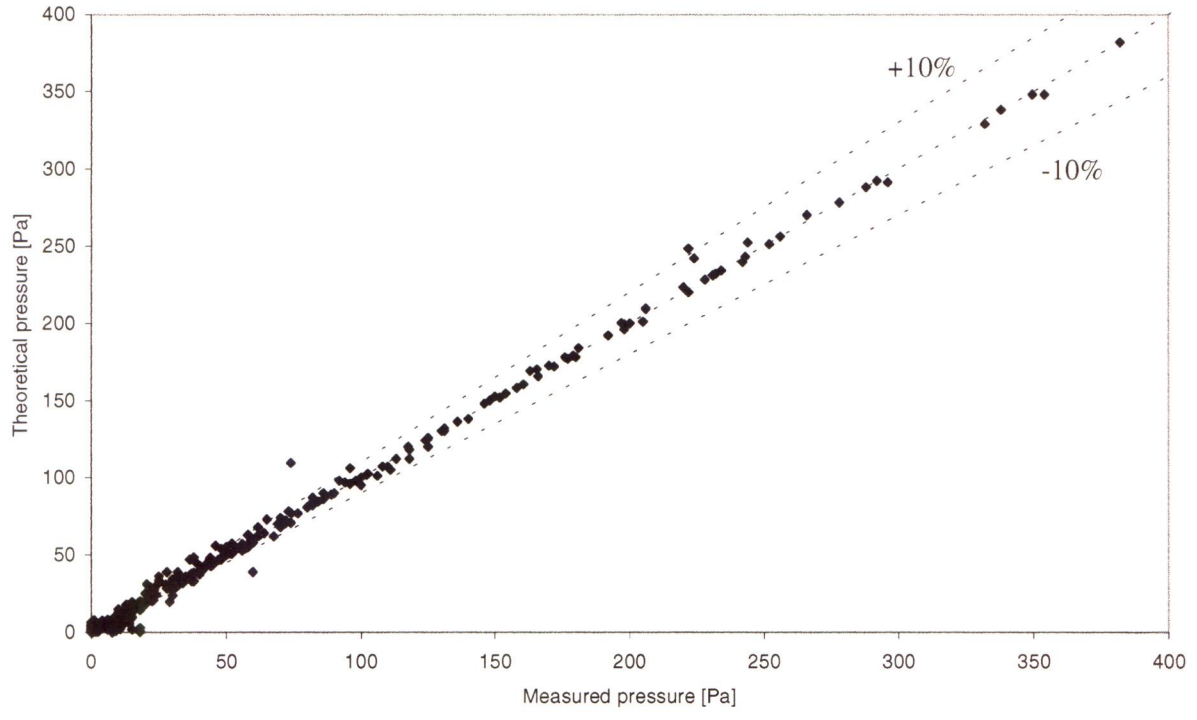

Figure 4.9 Comparison of the theoretical and experimental pressures for all the tests.

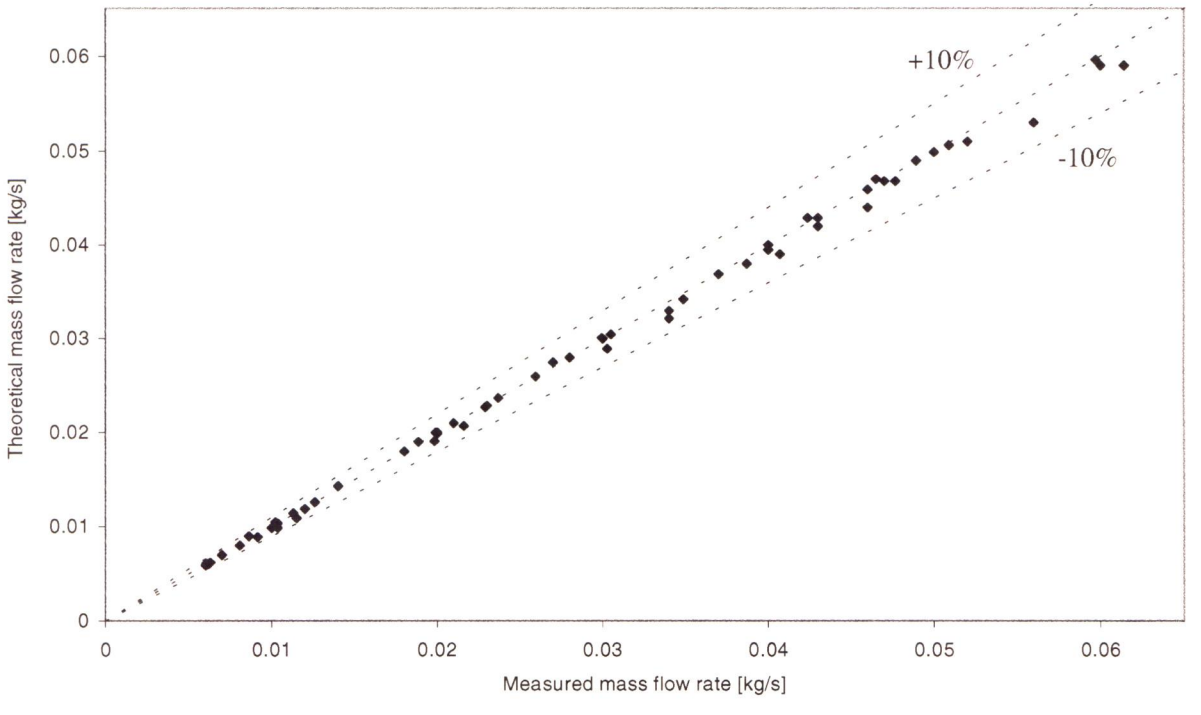

Figure 4.10 Comparison of the theoretical and experimental mass flow rates for all the tests.

From figures 4.9 and 4.10 it is seen that a good prediction of the pressures and mass flow rates can be obtained by using the fluid flow model. The comparison of the theoretical and experimental mass flow rates at low values shows good correlation.

4.3 AFPM flow analysis

The purpose of the experimental testing done on the AFPM machine model was not only to validate the fluid flow model but also to investigate the effect of changing critical dimensions of the machine. The AFPM machine can be viewed as a fan. The performance of a fan is easily illustrated with the use of its fan characteristic curve. Similarly the performance of the AFPM machine can be illustrated with the use of a characteristic curve. The first investigation was to determine if the thickness of the magnets and the axial gap between the rotor plates and the stator had any effect on the performance of the AFPM machine. Figure 4.11 shows the results for the case where there were no magnets and the axial gap between the stator and the rotor plates was changed between 6.5, 7.5, 8.5 and 9.5 mm. These axial gaps were attained by placing different thickness spacers between the rotor hub and the rotor plates (see figure 4.4). The pressure difference was the difference between the pressure at point 7 and the pressure at point 2. As figure 4.11 shows in the case where there are no magnets, the axial gap between the rotor plates and the stator has no effect on the performance of the AFPM machine.

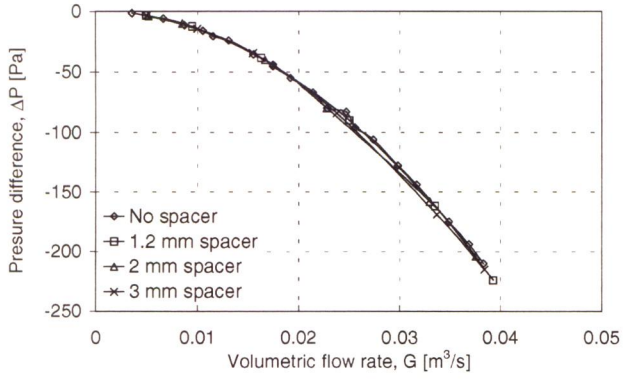

Figure 4.11 AFPM characteristic for no magnets.

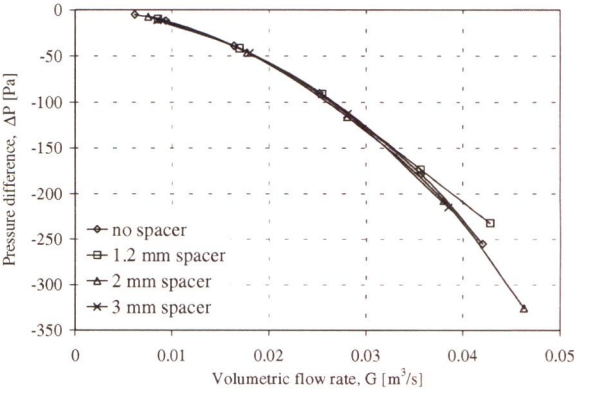

Figure 4.12 AFPM characteristic for 2.5 mm magnets.

In the case where the 2.5 mm magnets are used (figure 4.12) the axial gap between the rotor plates and the stator has no effect on the performance of the AFPM machine. Figures 4.13 and 4.14 show the results for the 5.5 and 7.5 mm magnets respectively. Once again the effect of the magnet thickness and axial gap was negligible.

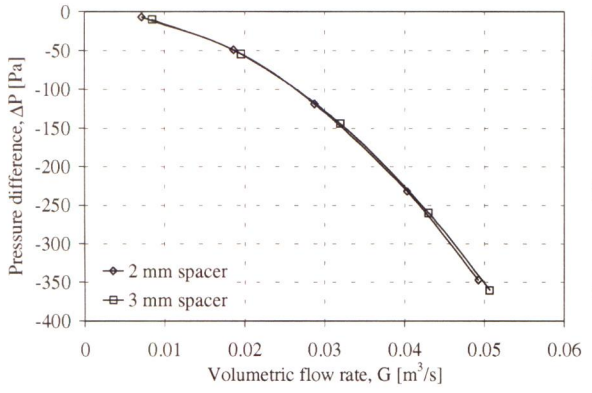

Figure 4.13 AFPM characteristic for 5 mm magnets

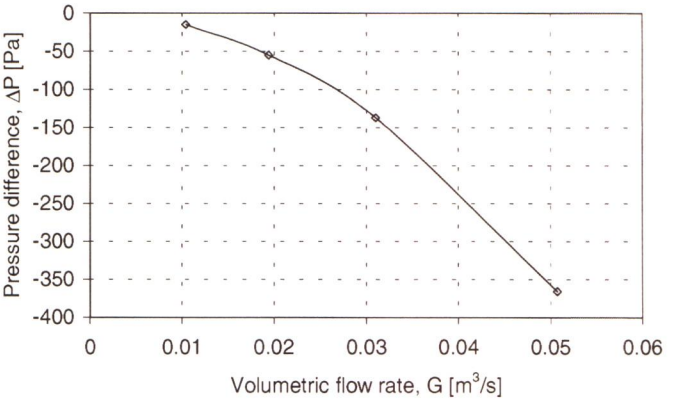

Figure 4.14 AFPM characteristic for 7.5 mm magnets

From the above results it is clear that the axial gap between the rotor plates and the stator had no effect on the performance on the AFPM machine. The above results can be combined into one characteristic for each set of magnets. These can then be combined in order to investigate the effect of the magnet size on the performance of the AFPM machine (see figure 4.15).

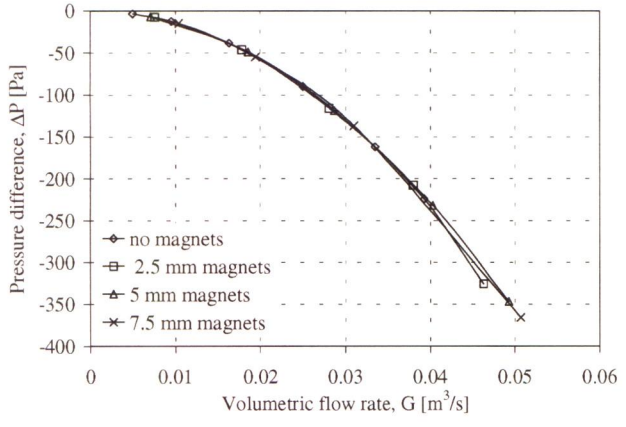

Figure 4.15 AFPM characteristic for all magnets

The overall result is that neither the size of the magnets nor the size of the gap between the stator and the rotor plates had an effect on the flow rate through the AFPM machine. The size of the gap between the rotor plates and the stator however, plays a critical role in the electrical performance of the AFPM machine.

When the pressure distribution through the AFPM machine as well as the velocity at each of the points is known, it is possible to calculate the energy of the air at any point. The amount of energy lost or gained between any two points can be calculated. Figure 4.16 shows the cumulative loss and gain in energy starting from point 0 and ending at point 8 where all the

energy gained is lost to the atmosphere. This calculation was done at a rotational speed of 2390 rpm with the 2.5 mm magnets and the 2 mm spacer. Figure 4.17 shows the actual loss and gain between the points. It is possible to see where the largest gain and loss in energy occurs in the AFPM machine.

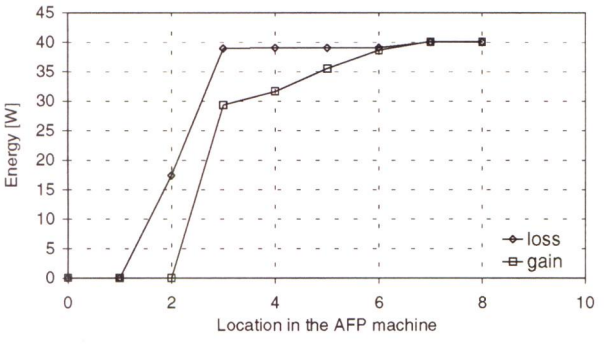

Figure 4.16 Cumulative loss and gain of energy through the AFPM machine

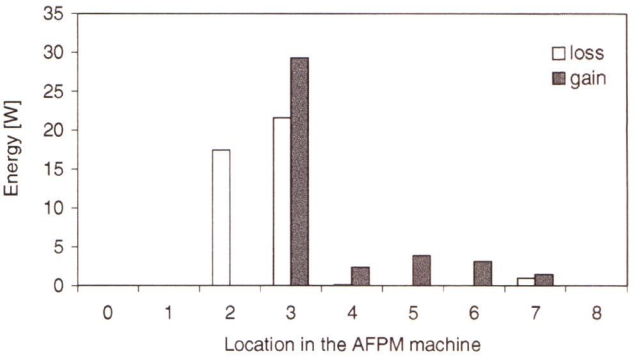

Figure 4.17 Loss and gain of energy through the AFPM machine

In the fluid flow model it was assumed that the temperature of the air was constant, equal to the temperature of the inlet air. This is in fact not the case: as the air travels through the flow channel, the temperature of the air increases. Depending on the operating conditions the outlet temperature can differ from the inlet temperature by as much as 35 °C. This change in temperature has an effect on the air density and viscosity, which in turn has an effect on the calculated velocities, pressures and mass flow rate. The effect of neglecting the air temperature was investigated for three different cases. In these simulations the thermal model was used to establish the average air temperatures for the relevant flow sections. This was done for three different rotational speeds; the results are shown in table 4.1.

Table 4.1 Average air temperatures in Kelvin for different rotational speeds.

Section	368 rpm	1432 rpm	2370 rpm
0-1	293	293	293
1-2	293	293	293
2-3	295.5	293.8	293.4
3-4	306.2	301.6	297.8
4-5	315.3	305.7	304.2
5-6	321.7	311.4	307.8
6-7	320.2	310.8	306.6
7-8	320.2	310.8	306.6

These average air temperatures were then used in the fluid flow model to calculate the mass flow rate. The results are summarised in table 4.2. Column A indicates the calculated mass flow rate with the assumption that the temperature remains constant throughout the flow channel. Column B shows the calculated results when the temperatures from the thermal model are used in the fluid flow model. The percentage difference between the two is also shown.

Table 4.2 Comparison of mass flow rates for constant air temperature and varying air temperature

Rotational speed [rpm]	**A**	**B**	**% Difference**
368	0.0664	0.0616	7.22
1432	0.264	0.2384	9.69
2370	0.448	0.3984	11.07

5 Discussions and conclusions

In this research project, "Thermal Management of an Axial Flux Permanent Magnet Machine Considering Heat Pipes", the background research, thermo-fluid modelling techniques, heat pipe theory, rotor-stator systems and experimental results was presented. The background research gave an introduction to the AFPM machine and the reasons why these machines are preferred to the conventional cylindrical radial flux motors. The prototype AFPM machine developed by the Electrical Engineering Department of the University of Stellenbosch was used as an example to illustrate the thermal characteristics of these machines.

A theoretical thermo fluid model of the AFPM machine was configured and showed good correlation with the experimental work. The thermo fluid model was divided into two sections. Firstly a fluid flow model was set up from which the pressure distribution and mass flow rate of air through the machine was obtained. Secondly a theoretical thermal model was set where the calculated mass flow rate was used to obtain the temperature distribution in the machine. The thermal model allows the user to define the size of the machine, the material properties and the size of the discretisation mesh. The thermal model made use of axial symmetry and allowed for different environmental conditions.

A possible change in ambient conditions was accommodated for during the experiments. All fluid flow experiments were completed within the course of one calendar month. Both the fluid and thermal models were able to accommodate different ambient conditions.

5.1 Fluid flow model

In the fluid flow model one simulation program was written to simulate the pressure distribution and mass flow rate of air in the half scale model of the AFPM machine. The model of the AFPM machine had a rotor diameter of 360 mm and was driven by a separate DC motor. Air is drawn in through the inlet pipe. The air enters the inlet pipe through a bellmouth which was used to measure the flow rate. The air moves from the inlet pipe to the radial blades of the rotor hub where its direction is changed from an axial to a radial direction. The air is split into two separate channels as it moves around the stator. Between the rotor plates and the stator the air moves over the magnets. There are 40 magnets attached to each of the rotor plates. It is here where the air experiences a viscous pumping effect. The air moves into the shroud and is taken through the

shroud outlet to the atmosphere. A schematic illustration of the fluid flow channel can be seen in figure D.1.

The fluid flow model was divided into 8 sections. For each section the energy,momentum and continuity equations were solved. An iteration process was used to find the pressure distribution and subsequent mass flow rate of air through the machine. The energy loss coefficients in the machine were determined experimentally. The loss coefficient over section 2 to 3 was found to be dependent on the geometrical changes made during the experiments. The remaining loss coefficients were found to be independent of the geometrical changes.

The results as seen in figures 4.16 and 4.17 show that the radial blades of the rotor hub result in the largest energy loss. This is due to the fact that the blades are radial and not curved, which increases the *shock* and *slip* in the blade passage. The blades of the rotor hub are made to be radial as the AFPM machine will operate as a motor and generator. When operating as a motor the AFPM machine uses electrical energy and converts it into rotational movement. When operating as a generator the AFPM machine is driven by an external motor and converts this rotational movement into electrical energy. These two operating modes require that the machine turn in opposite directions and hence the radial blades.

It was found, during the experimental work, that a certain amount of air was found to 'leak' between the inlet pipe and enter into the cavity between the rotor plates and the shroud. This 'leakage' could not be measured but by putting a few water drops in the clearance space it was found to be if anything very small. The fluid model was based on an assumption that the air temperature remained constant throughout the flow channel. This is, however not the case. Simulations were done where the temperature distribution of the air obtained from the thermal model was used in the fluid flow model and the error in using this assumption was found to be at its highest 11.07 %.

It can be concluded that the pressure distribution and mass flow rate of air in the theoretical fluid flow model correlated to within 10% to the pressure distribution and mass flow rates obtained from the experimentally tested model of the AFPM machine. This level of accuracy was attained by choosing the energy loss coefficients so that the pressures at the various points would match.

5.2 Thermal Model

The thermal model consisted of two separate programs. The first program was used to establish the geometry of the AFPM machine, set the material properties and generate the mesh used to calculate the nodal temperatures. The thermal model was based on a two-dimensional finite difference method. Components which were anisotropic were modelled by isotropic components in which the material properties were suitably adjusted. The thermal model considered in this research project differed from the actual AFPM machine in that the thermal model was shrouded.

Correlations were used to determine the convective heat transfer coefficients on the surface of the rotor plates and the stator. These correlations were taken from published papers. The correlation for the convective coefficient on the surface of the stator gave results that did not correspond to the experimental values. This is because the correlation was for a limited range of mass flow rates that did not lie in the range of mass flow rates investigated in this research project. The correlation for the convective heat transfer coefficient on the surface of the rotor plates was used for the stator and this yielded results that were in agreement with those obtained experimentally.

The thermal model was used to investigate the effect of different operating conditions and machine geometries on the operating temperatures in the AFPM machine. These effects were all compared to one base case and it was through these comparisons that an understanding and interpretation of the thermal characteristics of these machines could be drawn. The conditions that were investigated were; the gap ratio between the rotor plates and the stator, the effect of a shroud, the surrounding air temperature, the inlet air temperature, the surface emissivity of the components and the effect of placing a heat pipe in the stator.

The convective heat transfer coefficient on the surface of the rotor plates and the stator is dependant on the gap ratio. Simulations were done where this ratio was changed from 0.00137 to 0.02739, which corresponds to axial gaps between the rotor and the stator of 0.5 mm to 10 mm and average convective heat transfer coefficients of 297.1 W/m^2K and 141.9 W/m^2K respectively. It was found that for gap ratios below 0.012 the effect of the gap ratio was more significant. The maximum stator temperature for a gap ratio of 0.00137 was 355.8 K and that for a gap ratio of 0.02739 was 379.59 K. This shows a 23.79 K change in temperature, and although the relationship is not exactly linear, one can assume a change of 2.5 °C for every millimetre gap between the rotor plates and stator. This applies only when the mass flow rate of

air is over 1 kg/s, for mass flow rates below 1 kg/s the effect of the gap ratio was found to decrease.

Simulations were done where the effect of having a shroud around the AFPM machine was investigated. The shroud would be used to prevent the warm air that exits the machine from re-entering the inlet and thus causing the operating temperatures to increase. The current prototype AFPM machine is operated under benign conditions and did not necessitate a shroud. For air mass flow rates above 1 kg/s the maximum stator temperature in the case of no shroud was 369 K and that in the case with a shroud was 370 K. The results showed that a shrouded AFPM machine would not have higher operating temperatures then an unshrouded AFPM machine. These results were calculated with the assumption that there is no re-circulation of the air.

The effect of the surrounding air temperature was investigated. The surrounding air temperature can vary depending on the location of the AFPM machine. For example if the AFPM machine is used in regions of high ambient temperatures, the operating temperatures of the AFPM machine would be different to when it is operating in conditions where the surrounding temperature is lower. In the simulations the surrounding air temperature was changed from 273 K to 323 K with an inlet temperature of 293 K, which corresponded to maximum stator temperatures of 369 K and 370.3 K for mass flow rates above 1 kg/s. As these results show the effect of the surrounding air temperature was not significant and this also applied for mass flow rates below 1 kg/s.

The effect of the inlet air temperature was investigated. The inlet temperature of the AFPM machine can vary due to the environmental conditions as well as due to the external cooling of the inlet air. It may be that the inlet air is cooled by an external apparatus prior to entering the AFPM machine. In the simulations the inlet air temperature was also varied from 273 K to 323 K and the corresponding maximum stator temperatures were 350 K and 399 K, which was one of the more significant results. As a rough guide one can assume that for every degree the inlet air temperature is lowered the maximum stator temperature will drop by the same amount.

Simulations were done whereby the emissivity of the surfaces in the AFPM was changed from 0.2 to 0.9. It was found that the lower values of emmisitivity gave higher operating temperatures in the AFPM machine. Applying surface paints to the various components can change the emissivity of the surface. The maximum stator temperature for an emissitivity of 0.2 was 375.7 K and that for an emissitivity of 0.9 was 370.1 K.

The possible use of a heat pipe was investigated. The best position for the heat pipe was found to be at the inner radius of the stator (see figure 3.16). This is where the maximum temperature in the stator occurs, due to the densely clustered copper wires in this region. The copper wires in the stator produce heat due to the eddy current losses. Various geometries of the heat pipe were also investigated. The diameter of the heat pipe is an important criterion to consider. Larger pipe diameters meant: larger surface areas were possible, lower mass flow rates of liquid were required, which in turn meant lower axial velocities and pressure drops in the heat pipe. Overall, a larger heat pipe diameter results in lower maximum stator temperatures. Two problems associated with the size and location of the heat pipe are that it must be constructed from a non-metallic material to prevent interference with the magnetic flux present and it has to be 'threaded' in between the copper wires. IF the heat pipe is located at the inner radius of the stator, where the copper wires are most densely clustered, there may be a formidable problem. Heat pipe diameters of 2 and 10 mm gave maximum stator temperatures of 360.51 K and 341.9 K respectively. This shows roughly a decrease of 2.3 K for every 1 mm increase in diameter of the heat pipe. These results are for a constant convective heat transfer coefficient of 1000 W/m^2K inside the heat pipe.

The convective heat transfer coefficient on the internal surface of the heat pipe is also an important criterion of the heat pipe. Simulations were done where this variable was changed from 200 to 2000 W/m^2K, which gave maximum stator temperatures of 343.3 K and 333.68 K respectively. The convective heat transfer coefficient is determined by the thermophysical properties of the fluid used and the velocities found in the heat pipe. The overall effect of a heat pipe was found to reduce the maximum stator temperature from 370 to 345 K. This is for the heat pipe that was positioned at the inner radius of the stator, a convective heat transfer coefficient of 1000 W/m^2K and a pipe diameter of 10 mm.

5.3 General

The results presented in this research project give valuable insight into the thermal management of AFPM machines. Various combinations of geometrical configurations, material thermal properties, environmental conditions, and the use of a heat pipe were investigated by using the developed numerical models. The results show that the maximum stator temperature was most sensitive to the temperature of the air entering the AFPM machine, the gap ratio between the rotor plates and the stator, and the surface emissivity of the components. The effect of the shroud and the temperature of the surrounding air were found to be negligible. This shows how

important it is to have a proper understanding of the thermal characteristics of these machines. A heat pipe was also considered to remove the heat, which was generated internally within the stator. The inclusion of the heat pipe gave the lowest operating temperatures.

In conclusion, it can be said that the design of AFPM machines requires a detailed knowledge of the thermal characteristics of these machines. To manage and control the operating temperatures the effects of geometry, material properties and environmental conditions must be known.

6 Recommendations

The possible future use of heat pipes as a cooling mechanism should be considered in more detail. The heat pipe considered in this project was based on the assumptions that the heat pipe remained at a constant temperature, equal to that of the air that cooled the finned surface. Different values of this temperature could also be specified in the simulation program. It was also assumed that the internal resistance of the heat pipe were negligible. The only resistance taken into account was the convective resistance on the outer wall of the heat pipe. The overall resistance of the finned surface was also taken into account. It is recommended that the results obtained from the thermal model for the heat pipe are only used as a guideline for the selection of the heat pipe size and the required area of the finned surface.

The fluid flow model of the AFPM machine correlated well with experimental data at high rotational speeds. At low rotational speeds it was found that the correlation between the calculated and experimental pressures was not as good. This is ascribed to three possible reasons. The static pressures associated with low rotational speeds are very low and reading these pressures was difficult. The sensitivity of the measuring equipment (Betz Manometer) was insufficient and small changes in static pressures could not be noted. The speed controller of the electric motor which drove the experimental AFPM model was not very stable at low speeds, the fluctuations in rotational speeds was found to be as high as 150 rpm for speeds below 500 rpm. These problems can be overcome by using more sensitive measuring equipment and a more stable speed controller. It is recommended that for low speed applications the fluid flow model should include a second set of loss coefficients specifically determined for the low speeds.

The thermal model did not take the re-circulation of air into account because re-circulation can be eliminated by the proper design of the inlet and outlet. This re-circulation can be eliminated by locating the inlet as close as possible to the radial blades of the rotor hub as well as adopting an inlet of the type shown in figure 6.1. In this configuration the overlap between the rotor plate and the inlet pipe will limit the amount of air that is re-circulated.

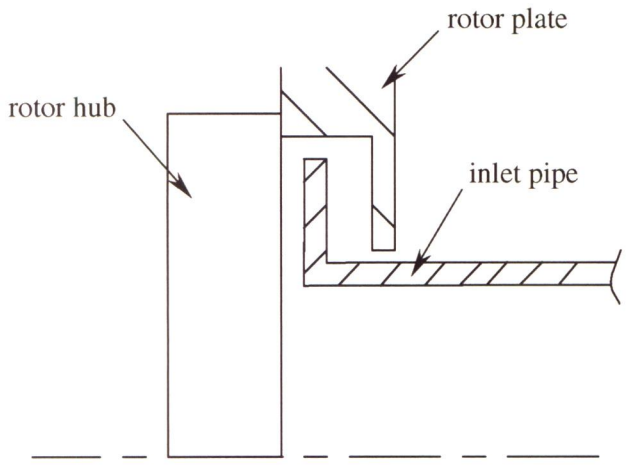

Figure 6.1 Possible inlet configuration to limit the re-circulation of air.

From the experimental tests done on the AFPM model it was found that the magnet thickness had no effect on increasing the air mass flow rate. It is recommended that the magnets are "covered" or embedded in the rotor plates. This will reduce the windage losses of the AFPM machine and will have a secondary benefit in that the magnets can be more securely fastened to the rotor plates and thus prevent them from shearing off. It is important that the magnets are covered by a non-metallic material as to prevent any interference with the magnet field. Consideration was not made to the spacing of the magnet, namely the possible variations in the magnet and gap angle as shown in figure D.8. It was not known whether this would have an effect on the flow rate of air through the AFPM machine and should be considered.

The experimental tests also showed that the flow rate of air through the AFPM machine was determined primarily by the rotor hub. This leads to the recommendation that the design of the rotor hub must be more carefully considered. Currently the blades of the rotor hub are radial and impart large energy loss coefficients. The blades were designed in this way as the AFPM machine is designed to work in both directions of rotation. The rotational directions are changed when the AFPM machine acts as a generator and when it acts as a motor. Research should be conducted into the possibility of designing blades which can work in both directions.

From the results presented in this thesis it is clear that the most effective way to cool the AFPM machine and hence control the operating temperatures is by lowering the temperature of the inlet air. This will have to be achieved by the use of a refrigeration cycle. The extra power required to drive this refrigeration cycle could be taken from the AFPM machine itself. A portion of the

extra power required could be compensated for by reducing the windage losses in the AFPM machine as discussed previously.

The determination of the amount of heat produced in the stator due to the eddy current losses is not an arbitrary task and was not in the scope of this thesis. The amount of heat produced depends entirely on the electrical design of the machine and its specified speed and power. One of the objectives of this thesis was to investigate the thermal implications of the AFPM machine when operating at low speeds. This objective could not be met due to the reason mentioned above. Once the amount of heat produced in the stator is known, the thermal model can be used to determine the thermal response of the AFPM machine.

At the start of this research project the stator in the AFPM machine had been destroyed by a magnet that sheared off the rotor plates and cut through the copper wires in the stator. Experimental temperatures taken during this testing was limited to four thermocouples placed in the mid radius of the stator. Only one set of temperature readings were taken and are shown in figure 3.10. The validity of these readings is unknown as the tests were not conducted by the author. A subsequent stator was constructed using a different epoxy. It was found that this epoxy destroyed the insulation of the copper wires and was therefore not used. A third stator was then constructed, once again with a different epoxy. It was found that this epoxy did not meet the thermal specifications of the manufacturer. At the conclusion of this thesis no further testing of the AFPM machine had been conducted. It is recommended that further experimental values are used to validate the thermal model. Careful consideration should be made to the placement of the thermocouples in the stator. Attention should also be paid to determining accurate thermo physical data of the epoxy used. It is also recommended that the mass of the epoxy and the copper wires be measured during the construction, as this is a vital input in the thermal model. In the simulations done during the course of this thesis only approximate values were used for the mass of the epoxy and copper wires.

The following points should be considered as guidelines when using the thermal model:

- The material properties of all the components must be well documented.
- The thermal model is based on the assumption that all materials are isotropic. Anisotrpoic materials were not considered in this thesis. The rotor hub and stator were modelled as isotropic materials by compensating the thermo physical data.
- The thermal model can be used to simulate a complete operating cycle of the machine. The transient temperature response from start up to shut down can be determined.

- Algorithms developed by the author do the meshing of the AFPM machine in the thermal model. These algorithms are not perfect and it may be found that certain mesh sizes will cause instabilities and will cause the program to stop. Care should be taken when meshing the components. The order of the meshing should be followed as outlined in appendix A.
- The computational time of the thermal model is determined by the mesh size. Smaller mesh sizes result in a higher resolution of temperature field but will also increase the computational time required.
- Two text files are generated by the program and should be well scrutinized by the user. The first text file shows the actual temperature response of selected elements. The second text file shows an energy balance for each component. At the last time step of the simulation the thermal model calculates the heat transfer entering and leaving each component. This heat transfer is divided into the heat transfer by conduction, radiation and convection. An energy balance is then calculated and shown. This text file should be viewed to determine whether or not thermal equilibrium has indeed been reached.
- The thermal model does not check that the dimensions entered are physically possible. For example it is possible to have the inside radius of the rotor plate being larger then the outside radius. Therefore care should be taken when entering these dimensions.
- A more detailed explanation on the use of the thermal model is given in Appendix A and should be read thoroughly along with the theory outlined in Appendix C before it is used.

The following points should be considered as guidelines when using the fluid model:

- Only geometrically similar models can be modelled. Geometrically similar implies that all dimensions are a fixed ratio to those of the AFPM machine considered in this thesis.
- The rotational speed range should be limited to the range considered in this thesis. Rotational speeds in this thesis were limited to between 200 and 2300 rpm. As mentioned previously the results obtained for speeds below 500 rpm may not be accurate and should be used with caution.
- The fluid model can be used to investigate the effect of small geometry changes in the AFPM machine. The changes considered in this thesis were limited to different magnet thickness and different spacing between the rotor plates and the rotor hub.
- The fluid model was based on one-dimensional incompressible steady flow. The validity of the incompressible flow should be considered before used as a design tool.
- The effect of the magnet and gap angle on the airflow rate through the AFPM machine was not considered. Angles of 6.5° and 2.5° were used for the magnet and gap angle

respectively. Results obtained when using magnet and gap angles other then those used in this thesis should be scrutinized with care.

- A more detailed explanation on the use of the fluid model is given in Appendix B and should be read thoroughly along with the theory outlined in Appendix D before it is used.

7 References

Axcell, B.P. and Thainpong, C, 2001, *Convection to rotating disks with rough surfaces in the presence of an axial flow,* Experimental Thermal and Fluid Sciences, Vol. 25.

Benham, P.P, Crawford, R.J & Armstrong, C.G, 1987, *Mechanics of Engineering Materials, Second Edition,* Addison Wesley Longman, Ltd.

Callister, W.D, 1996, *Materials Science an Engineering Introduction, Fourth Edition,* John Wiley & Sons, Inc.

Cengel, Y.A. and Boles, M.A, 1994, *Thermodynamics, Second Edition,* McGraw-Hill, Inc.

Chandler, P.L. and Patterson, D.J, 2001, *Counting the losses in very high efficiency machine design,* Renewable Energy, Vol. 22.

Djaoui, M, Dyment, A. & Debuchy, R, 2001, *Heat transfer in a rotor-stator system with a radial inflow,* Eur. J. Mech., Vol 20.

Dunn, P.D. and Reay, D.A, 1994, *Heat Pipes,* Pergamon.

Evans, G., Blackledge, J. & Yardley P., 1999, *Numerical Methods for Partial Differential Equaions,* Springer.

Faghri, A, 1995, *Heat Pipe Science and Technology,* Taylor and Francis.

Finney, R L. and Thomas, G B, *Calculus Second Edition*, Massachusetts Institute of Technology, Addison-Wesley Publishing Company.

Greenberg, M.D, 1998, *Advanced Engineering Mathematics, Second Edition,* Prentice-Hall, Inc.

Harmand, S, Watal, B. & Desmet, B, 2000, *Local convective heat exchanges from a rotor facing a stator,* International Journal of Thermal Sciences, Vol. 39.

Hwang, C.C. and Chang, J.J, 2000, *Design and analysis of a high power density and high efficiency permanent magnet DC motor,* Journal of Magnetism and Magnetic Materials, Vol. 209.

Johansen, R, Patterson, D, O'Keefe, C. & Swenson, J, 2001, *The use of an axial flux permanent magnet in-wheel direct drive in an electric bicycle,* Renewable Energy, Vol. 22.

Ketkar, S.P, 1991, *Numerical Thermal Analysis,* ASME.

Kreith, F, 1999, *The CRC handbook of Thermal Engineering,* CRC Press.

Mills, A F, 1995, *Heat and Mass Transfer*, Richard D. Irwin, Inc.

Owen, J.M. and Rogers, R.H, 1995, *Flow and Heat Transfer in Rotating-Disc Systems, Vol. 2: Rotating Cavities,* Research Studies Press, Ltd.

Owen, J.M. and Rogers, R.H, 1995, *Flow and Heat Transfer in Rotating-Disc Systems, Vol. 1: Rotor-Stator Systems,* Research Studies Press, Ltd.

Puri, I.K. and Annamala, K, 2001, *Advanced Thermodynamics Engineering,* CRC Press.

Putta Swamy, C.L. and Singh, B.P, 1995, *Dynamic performance of a permanent magnet brushless DC motor powered by a PV array for water pumping,* Solar Energy Materials and Solar Cells, Vol. 36.

Rohsenhow, W.M. and Hardnett, J.P, *Handbook of Heat Transfer, Third Edition,* McGraw-Hill, Inc.

Sayers, A.T, 1990, *Hydraulic and Compressible Flow Turbomachines*, Library of congress catalogging-in-publication.

Schmidt, K. and Patterson, D.J, 2001, *Performance results for a high efficiency tropical ceiling fan and comparisons with conventional fans,* Renewable Energy, Vol 22.

Shigley, J.E. and Mischke, C.R, 1989, *Mechanical Engineering Design, Fifth Edition,* McGraw-Hill, Inc.

Shih, T.M, 1984, *Numerical Heat Transfer,* Hemisphere Publishing Corporation, 1984.

Swanepoel, G, 2001, Thermal Management of Hybrid Electrical Vehicles Using Heat Pipes, University of Stellenbosch.

White, F.M, 1994, *Fluid Mechanics, Third Edition,* McGraw-Hill, Inc.

Zill, D.G. and Cullen, W.R, 1992, *Advanced Engineering Mathematics,* Wadsworth, Inc.

Appendix A

Thermal model simulation computer program

The thermal simulation program was written in Visual Basic. It consists of two different programs, a geometry program and a calculation program. The geometry program is used to establish the geometry, mesh settings and material properties of the AFPM machine. The calculation program uses the data from the geometry program to calculate the transient response of the AFPM machine. One of the typical operating conditions of the AFPM machine is shown in figure A.1. This shows the AFPM machine acting as a generator when connected to an external energy source, for example a diesel engine. This is important to consider as it determines the boundary conditions for the thermal model. The air supply of the AFPM machine will be drawn from an external source and enter on the right hand side. The presence of the diesel engine on the left side of the AFPM machine will influence the temperature of the surrounding air. Radiation will occur between the diesel engine and the AFPM machine. This will result in an unsymmetrical temperature field about the axis shown in figure A.1. The thermal model is able to accommodate this aspect.

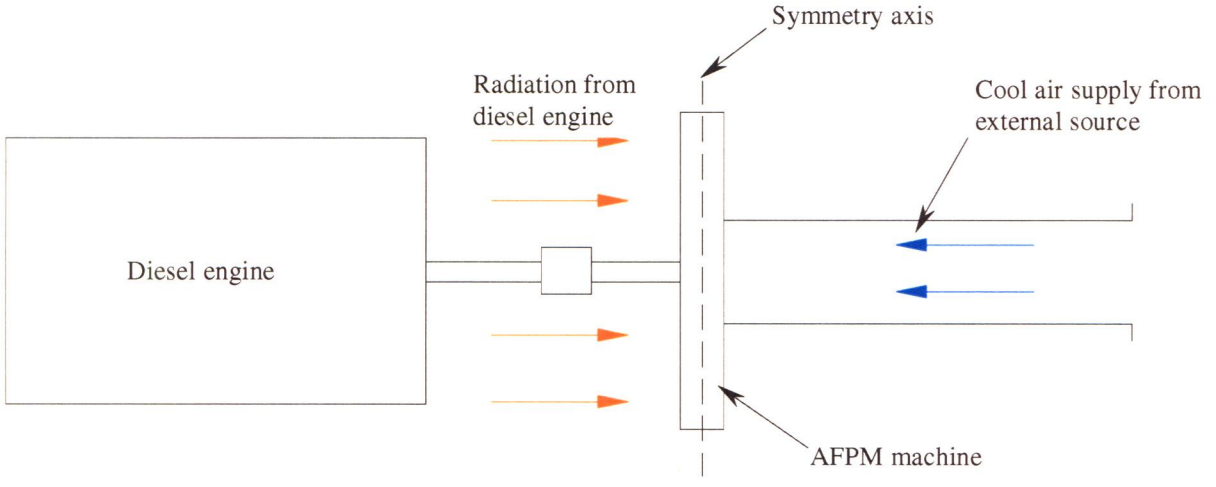

Figure A.1 Typical operating condition of the AFPM machine.

The file *geometry.exe*, which can be found on the supplied CD, will initialise the geometry program. The first window that appears is the main menu, figure A.2. Each component of the AFPM machine is featured here.

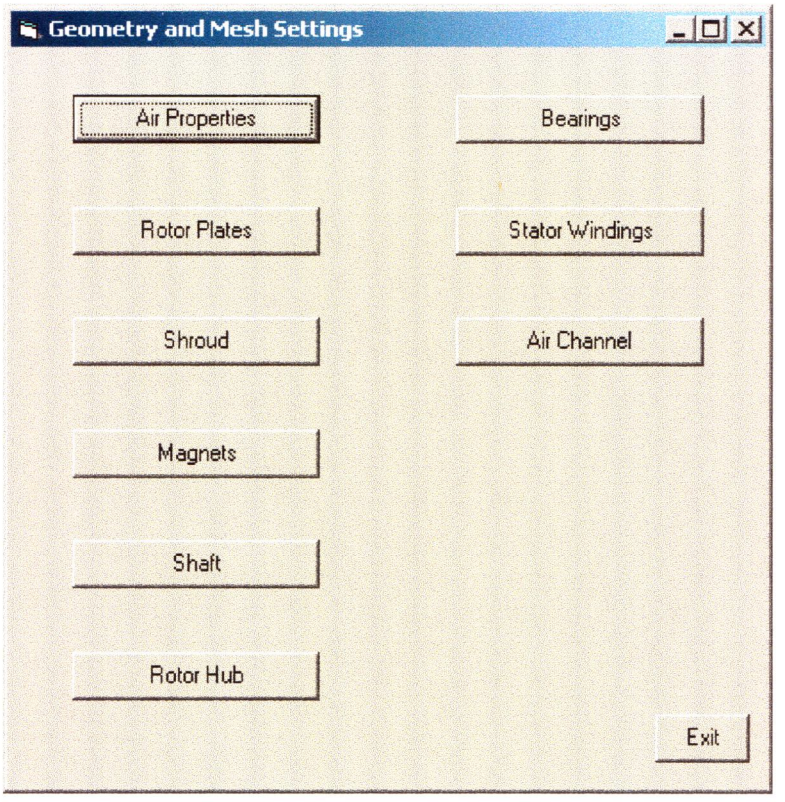

Figure A.2 Main menu of the geometry program

From the main menu the user can select which of the component's properties is to be established. The order in which this is done is important. In order to have a consistent and equal mesh the following order should be used; Air Properties, Rotor plates, Shroud, Magnets, Shaft, Rotor Hub, Bearings, Stator Windings, Air Channel. The main menu has been set out so that this order is easily followed. By clicking on the *Air Properties* button, the window in which the temperature, density, and other properties of the incoming air are set, is activated, figure A.3. The default values for the air properties are shown here. These values will appear each time the program is run. The user should take note of the units used, which are shown alongside each property. Once the properties have been set the output file is created by clicking on the *Generate Output File* button. This action creates a text file in which all the properties are contained. The program will create certain directories on the hard drive of the computer. All the files created are contained in the directory "*c:\afpm*" and can be viewed by the user. Once the output file has been generated the main menu is then reactivated. The user can also return to the main menu at any stage by clicking on the *Exit* button.

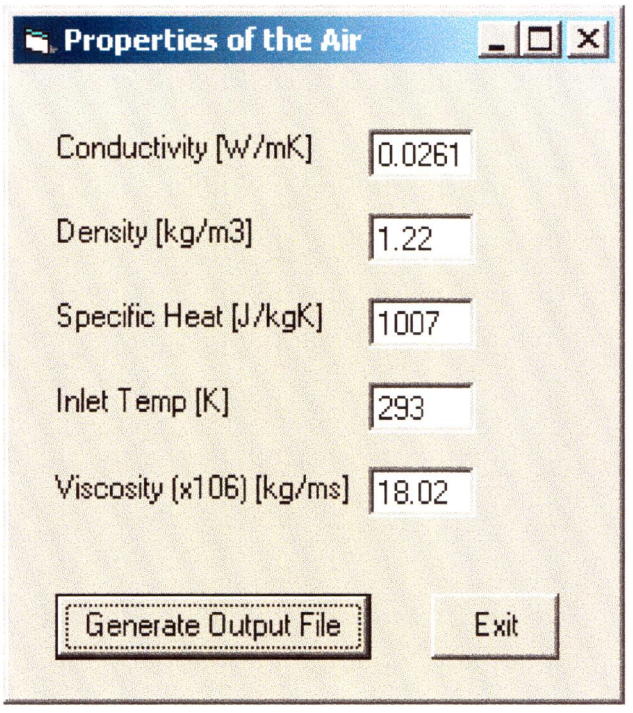

Figure A.3 Air properties window

Once the atmospheric conditions have been set the next step is to set the properties of the rotor plates. The window shown in figure A.4 is activated by clicking on the *Rotor Plates* button from the main menu. The dimensions of the rotor plates are located on the top left of the window. The dimensions which need to be set are the outside radius (Routside), the inside radius (Rinside), the radius at which the thickness changes (Rmiddle), the thickness of the top section (T1) and the thickness of the bottom section (T2). All dimensions are in mm. The material properties are located on the right hand side of the window. These values should be set as desired. The user will notice that the initial temperatures of the rotor plates must also be set, the left and right hand rotor plates can have different initial temperatures. The user can return to the main menu at any stage by clicking on the *Main Menu* button.

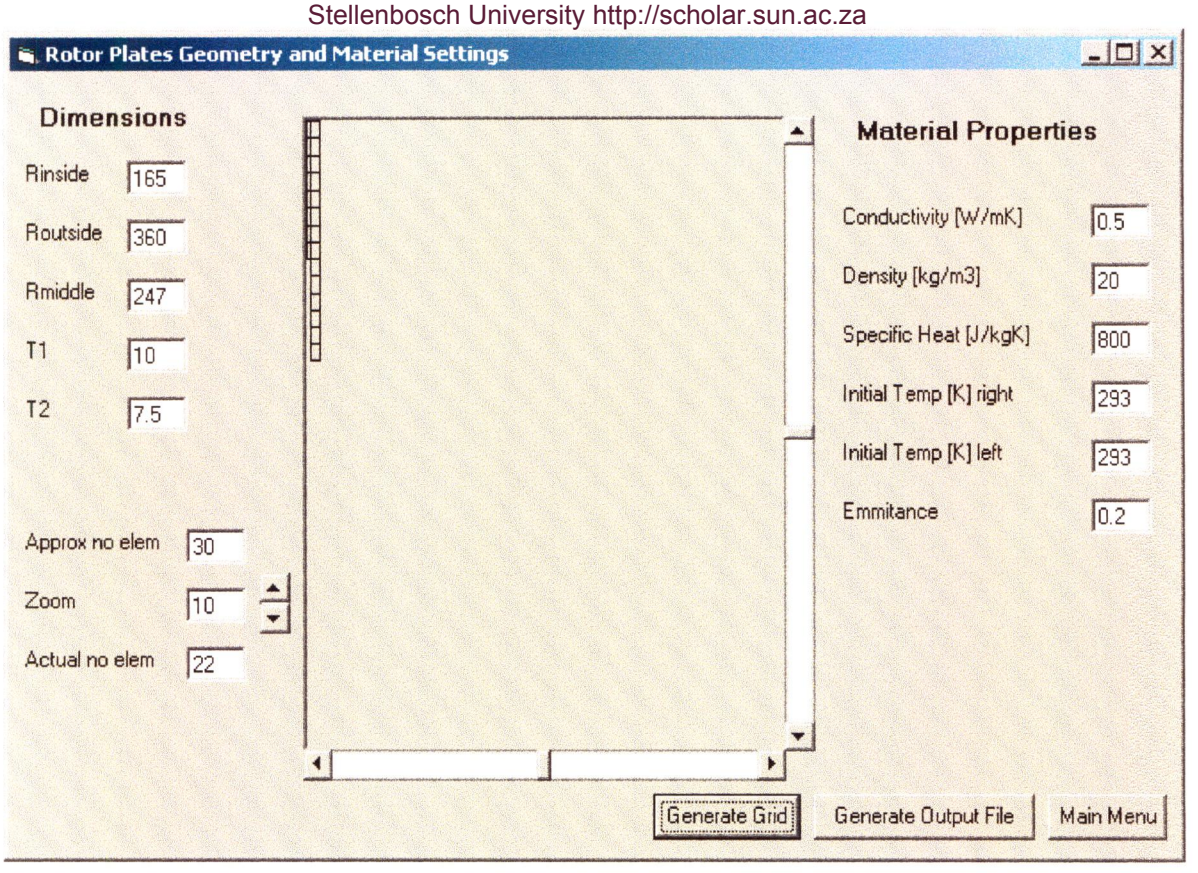

Figure A.4 Rotor plate window

Once the dimensions and material properties are set, clicking on the *Generate Grid* button creates the mesh for the rotor plates. A schematic representation of the rotor plates and the generated grid is displayed. The user sets the approximate number of elements. The actual number of elements is determined by the program, which calculates the most appropriate element size. The schematic representation may be moved within the window by using the vertical and horizontal scroll bars. Changing the zoom factor changes the size of the schematic, see figure A.5. Clicking on the *Generate Output File* button creates the various output files for the rotor plates. The output files typically contain each element's position, size, orientation etc. that will then be used by the calculation program. This must only be done once the material properties and dimensions have been set and the mesh is displayed on screen.

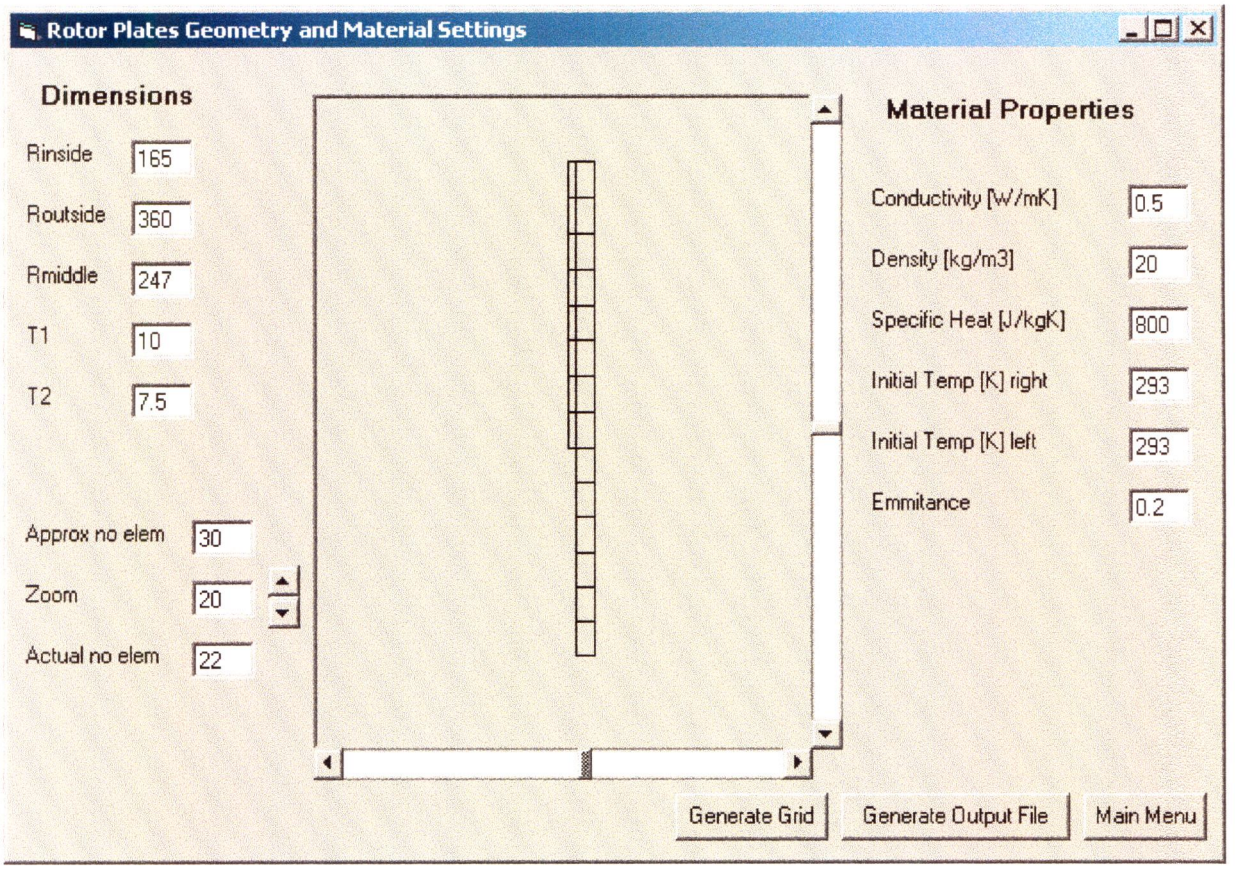

Figure A.5 Effect of the zoom factor and scroll bars

The properties of the shroud are set by following the above-mentioned steps, figure A.6. The size of the elements in the rotor plates will influence the size of the elements in the shroud. The purpose of this is so that elements in the shroud will be aligned with elements in the rotor plates (this simplifies the heat transfer calculations quite significantly). The dimensions of the shroud which have to be set are; the outside radius (Routside), the thickness of the shroud (Thickness), the inside radius of the right hand side (Rhole), the inside radius of the left hand side (Rshaft) and the distance between the left and right hand sides (Gap).

The properties of the magnets are set in the same manner, figure A.7. The size and position of the elements in the magnets are affected by those in the rotor plates. This ensures that the elements are aligned and of the same size. The dimensions of the magnets that need to be set are; the inside radius (Rinside), the outside radius (Routside) and the thickness of the magnets (Thickness).

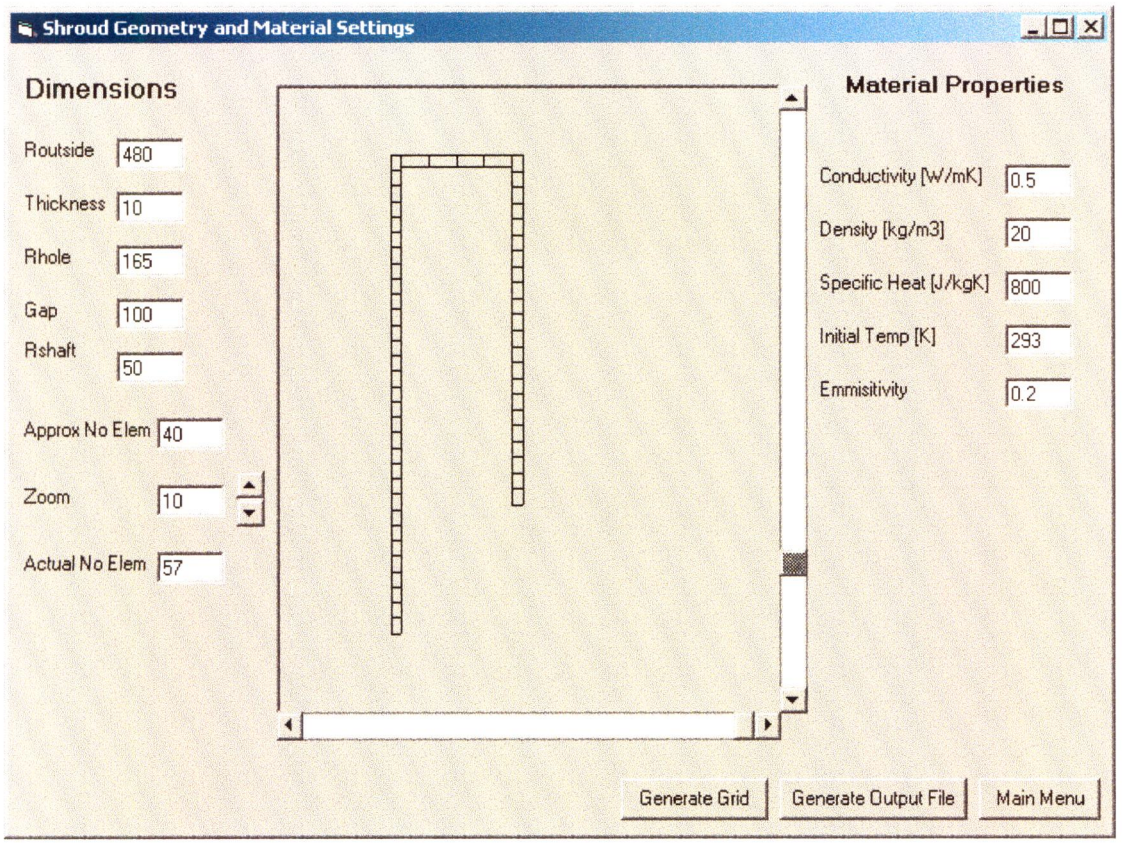

Figure A.6 Shroud settings

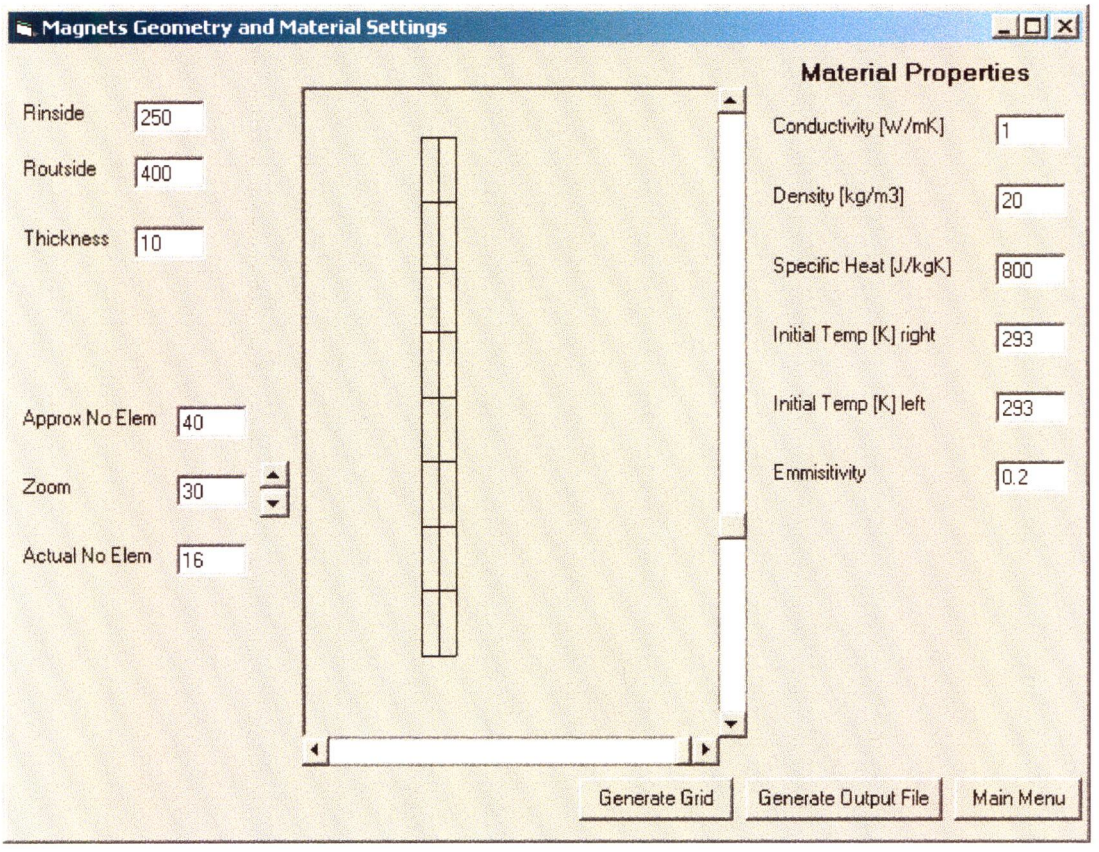

Figure A.7 Magnet settings

The shaft in the thermal model is modelled as in figure A.8. There are three regions where the diameter and length can be different. The right side of the shaft fits into the hole of the rotor hub and conduction occurs over the interface of these two components. The dimensions which need to be set for the shaft are; the radius of the right hand region (R1), the radius of the middle region (R2), the radius of the left hand region (R3), the axial length of the right hand region (A), the axial length of the middle region (B) and the axial length of the left hand region (C).

The rotor hub is a complex object to model. In the thermal model it is simplified to a solid disc, section 3.2.2. The material properties are calculated according to equations 3.17-20. This process takes into account the air that exists between the radial blades of the rotor hub. The radial blades of the rotor hub increase the exposed area between the air and the rotor hub. The dimensions for the rotor hub, which need to be set are; the inner radius (Rinside), the outer radius (Routside), the radius at which the radial blades start (Rmiddle), the width of the rotor hub (Thicknes), the number of radial blades (Num blades) and the thickness of the radial blades (Blade Thickness).

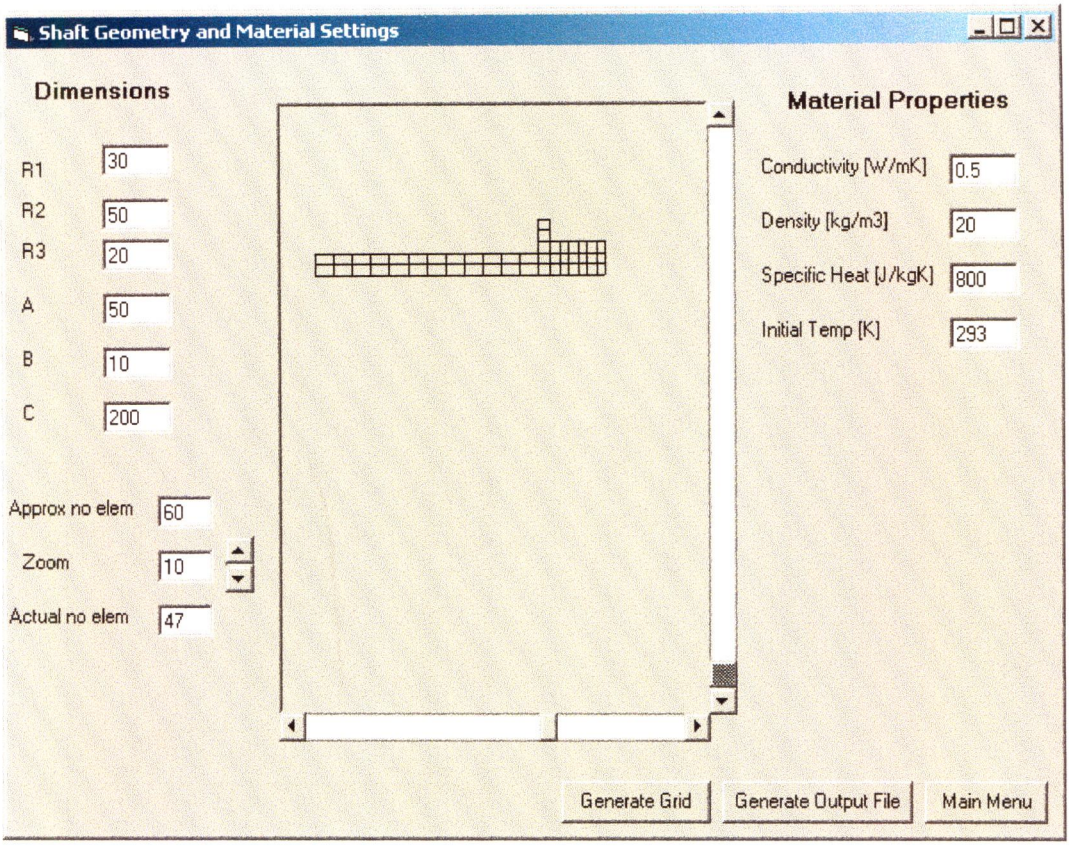

Figure A.8 Shaft settings

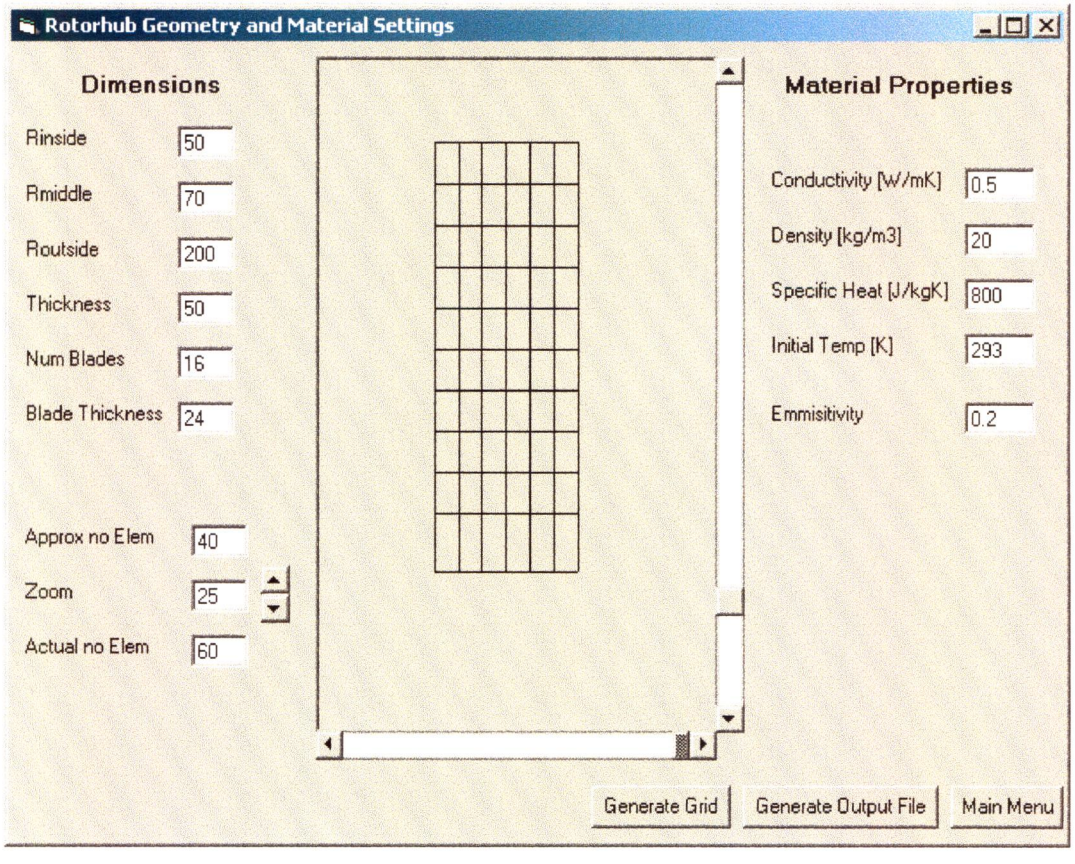

Figure A.9 Rotor hub settings

The bearings of the AFPM machine are located external to the machine itself. The thermal model of the bearings is simplified to that shown in figure A.10. The dimensions of the bearings which need to be set are; the inside radius (Rinside) and the outside radius (Routside)

The stator windings, figure A.11, consist of copper wire embedded in an epoxy. Heat is generated in the wires due to eddy current losses. The material properties of the stator are calculated according to the relative amounts of copper and epoxy in the stator. The equations outlined in section 3.2.2 are used to calculate the material properties of the stator. The dimensions of the stator which need to be set are; the inside radius (Rinside), the outside radius (Routside), the height of the middle section (L), the thickness of the middle section (T), the width of the stator (D) and the height of the top section of the stator (H). Figure A.12 shows a more refined grid on the stator. Although this increases the resolution of the temperature field the computing time is significantly affected by the number of elements.

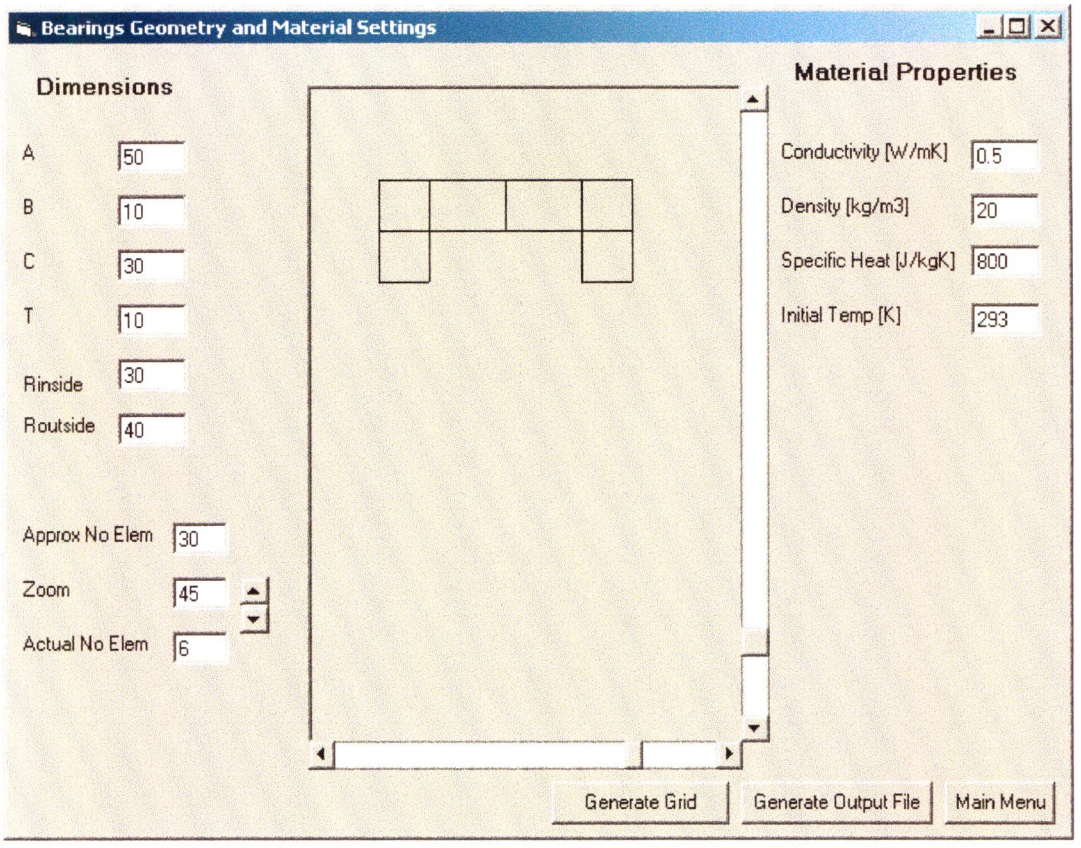

Figure A.10 Bearings settings

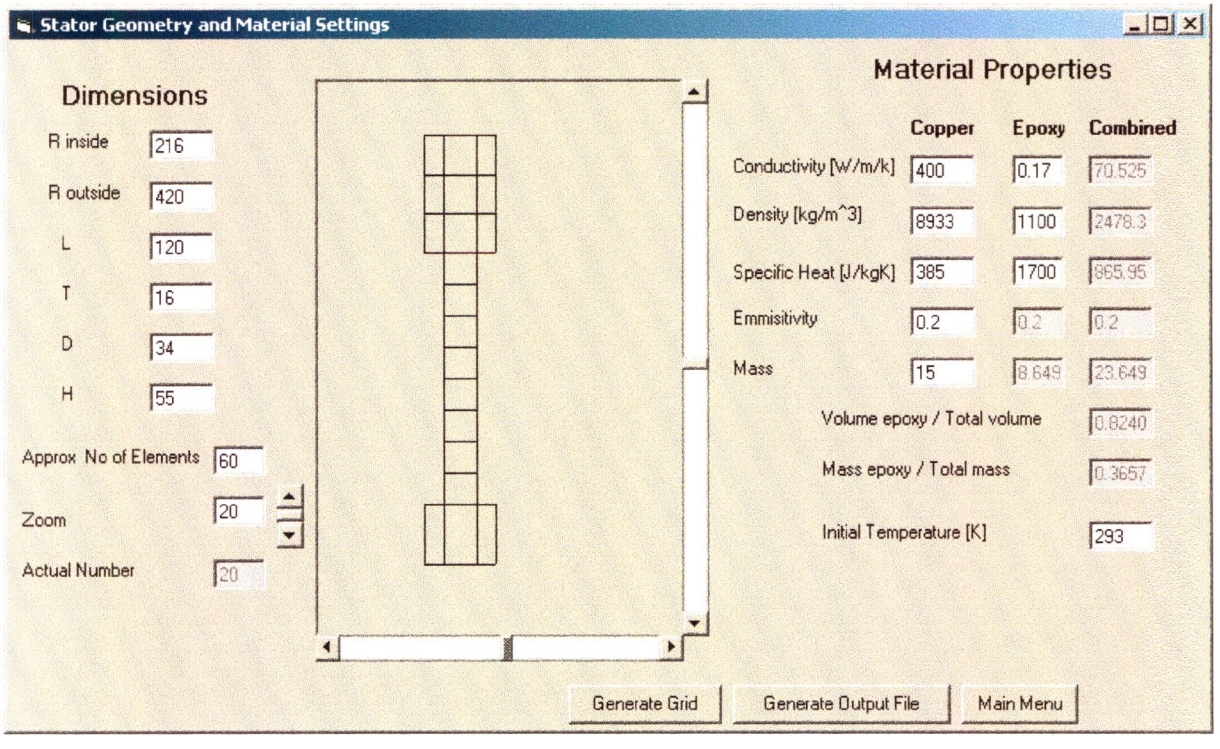

Figure A.11 Stator settings

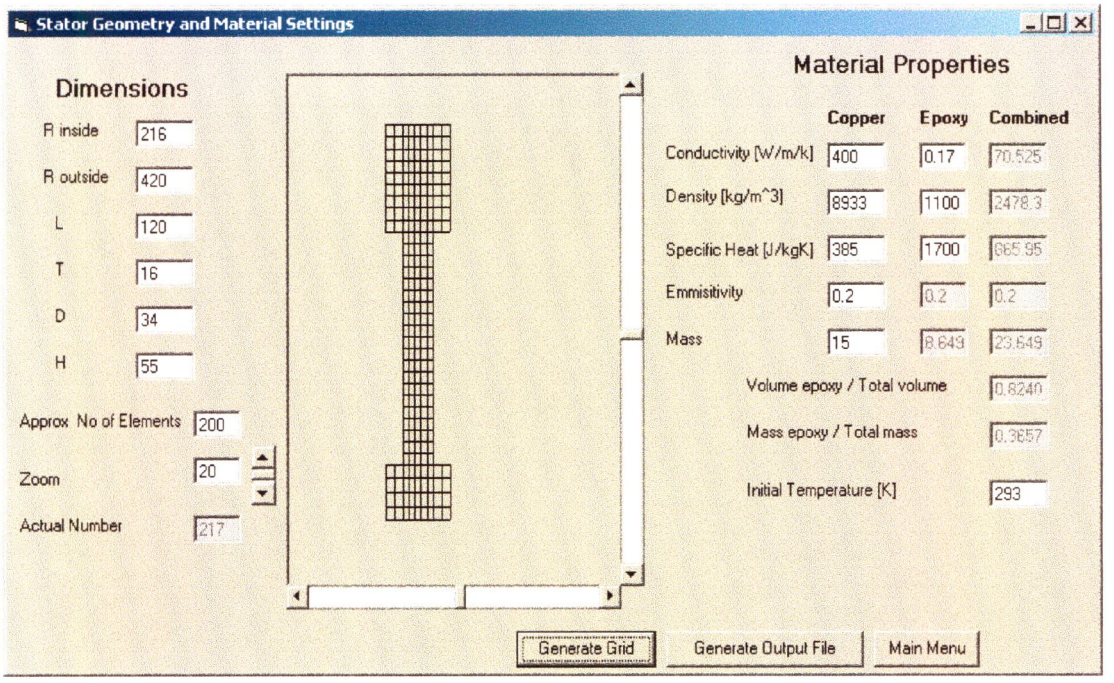

Figure A.12 Grid refinement on the stator

The air channel through the AFPM machine, figure A.13, is determined by the size of the geometry of the above-mentioned components. The mesh size is determined by the size of the elements in other components.

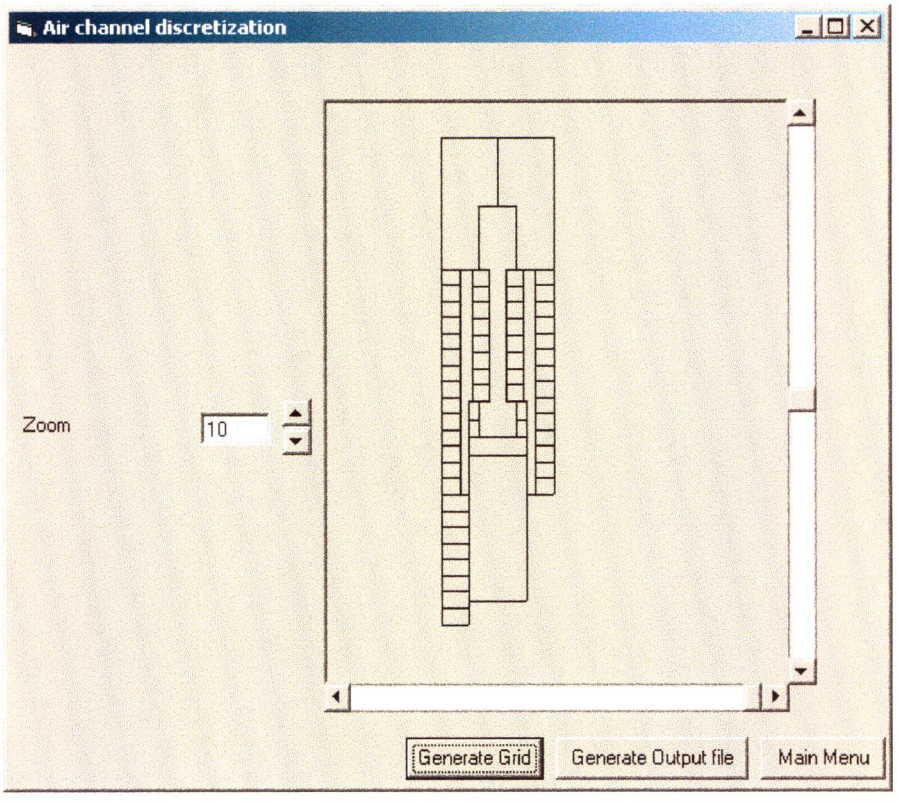

Figure A.13 Air channel

Once the geometry of the AFPM machine has been established the calculation program is used to calculate the transient response and is initialised by running the file *calculation.exe*. The opening window is shown in figure A.14. Various options for the simulation must be set. By clicking on the button *Output Files* the user will set the conditions for the output file. This text file contains the response of the individual components. These components must be selected as well as the frequency at which the response must be written to the file, figure A.15. The output file is named *response.text* and is located in *c:\afpm\output*. By clicking on the *Options* button, further options for the simulation can be set, figure A.16. Specifying the maximum and minimum temperatures sets the graphs scale. Any combination of components can be selected by the check boxes on the left hand side; only the transient response of the selected components will be plotted. There is also an option to display the elemental temperatures of a selected component. The input variables for the calculation which must be set are; the mass flow rate of air, the rotational speed of the rotor plates, the time increment, the total time for the simulation and the total internal heat generation for the stator. Other options which can also be set are: whether or not the specified heat pipe must be considered, if the radiation must be calculated and which equation must be used for the convective heat coefficient on the surface of the stator.

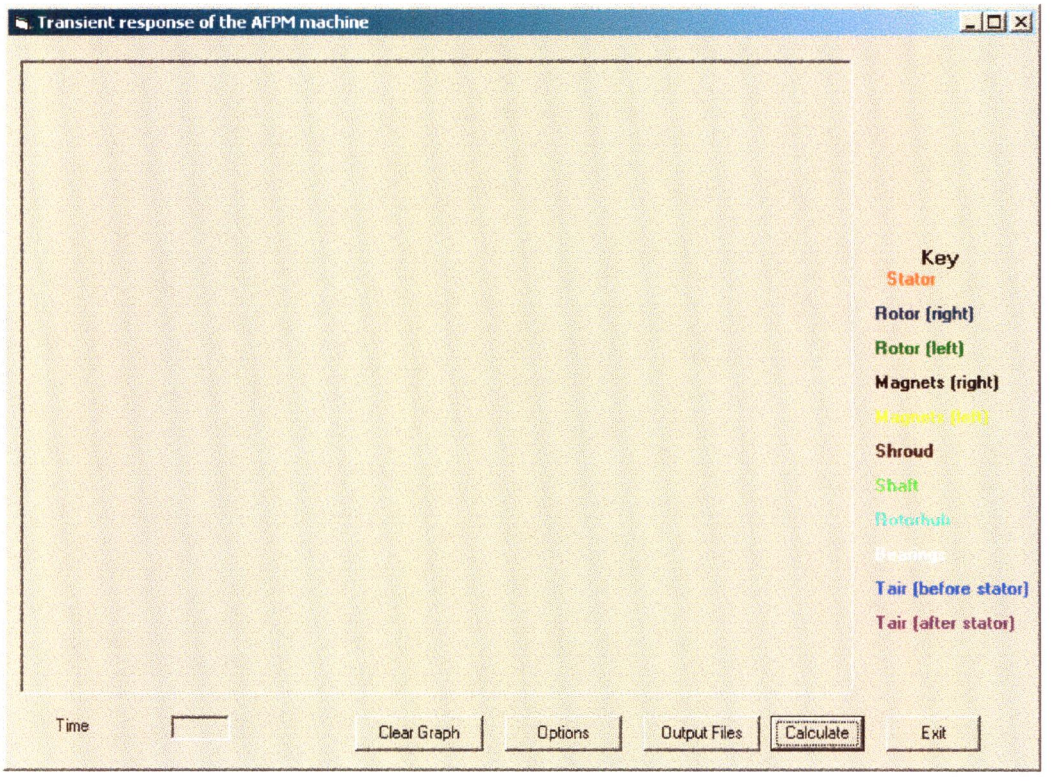

Figure A.14 Calculation window

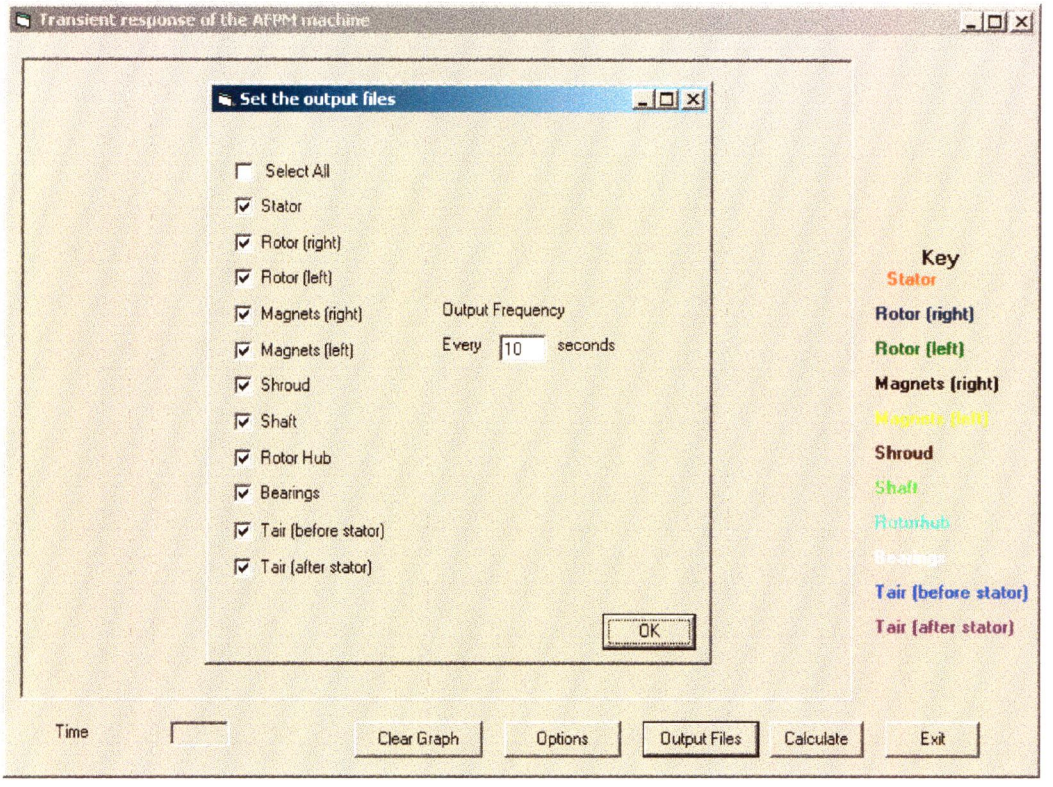

Figure A.15 Output file conditions

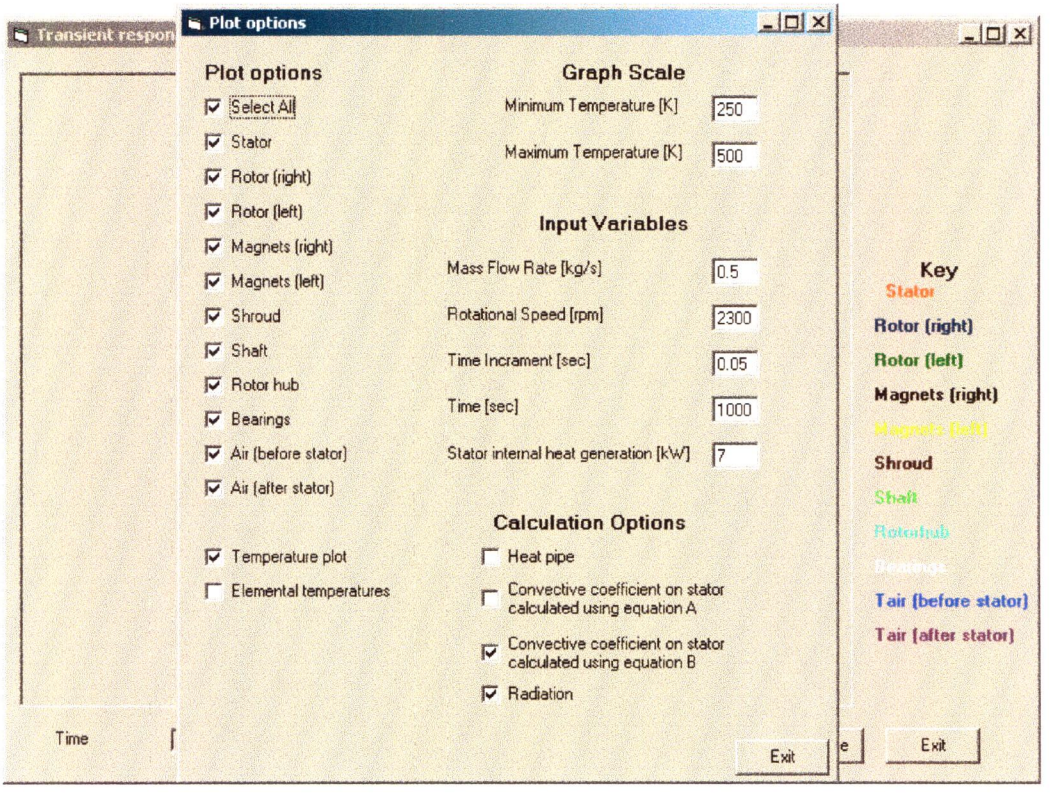

Figure A.16 Options for the current simulation

Figure A.17 shows a typical transient plot of the AFPM machine. The components are distinguished according to the key. Figure A.18 shows an elemental response for the stator.

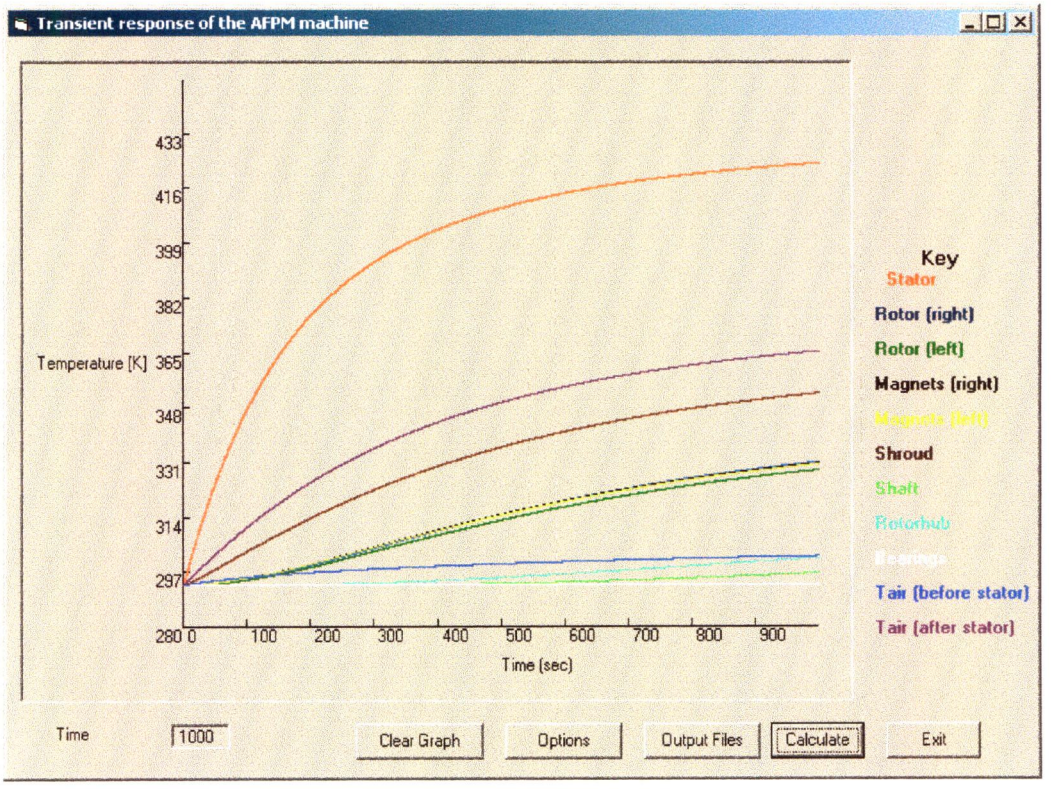

Figure A.17 Typical transient plot for the AFPM machine.

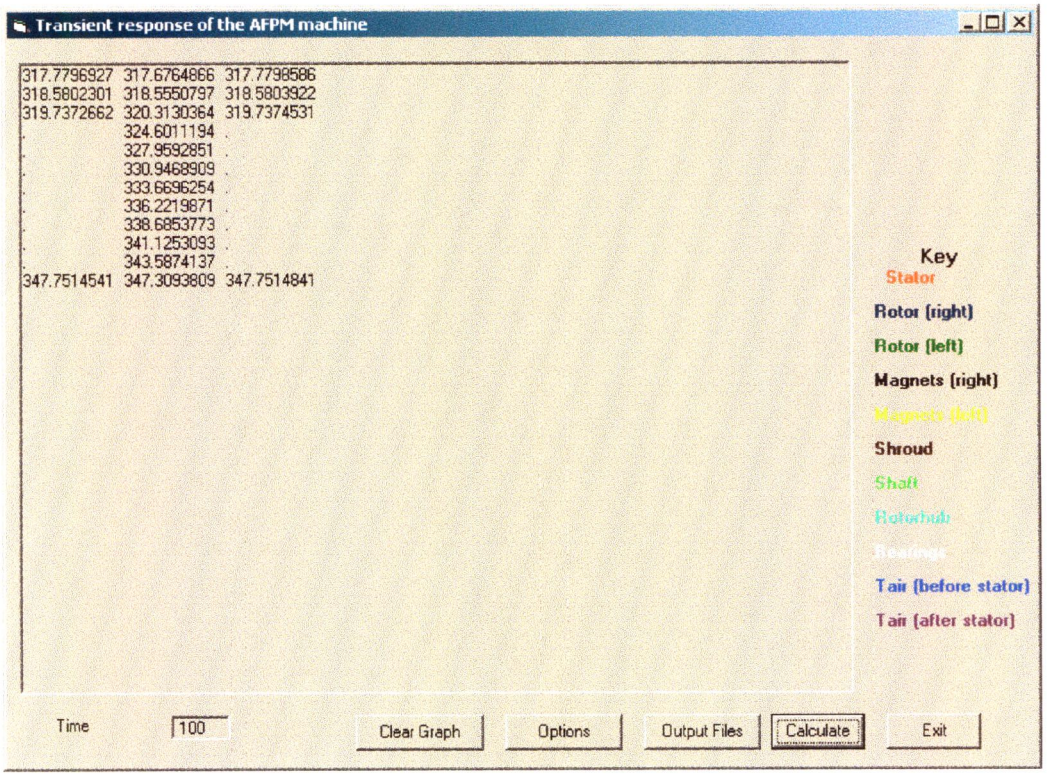

Figure A.18 Elemental temperature plot for the stator

Once the simulation is complete, an additional output file is created, *Final_time_step_analysis.text*, which is located in *c:\afpm\output*. This text file contains calculations made as at the final time step. At the final time step an energy balance is done on each component to determine whether it is in thermal equilibrium or not. The results of these calculations are shown in the text file.

Appendix B

Fluid flow model simulation computer program

The simulation program for the fluid flow model was written in visual basic. The program can be initialised by running the file *fluid.exe* located on the CD supplied. The opening window is seen in figure B.1. The first step in the fluid flow model is to set the boundary conditions for the iteration process, as described in section 3.1.4. The lower mass flow boundary must be lower than the anticipated value, say for example 0.000001 kg/s. Conversely the upper mass flow boundary must be higher than the anticipated value. The *Maximum error for P8* is used by the program to determine when the iteration process must be stopped. After each iteration the pressure at point 8 is subtracted from the pressure at point 0. If the absolute value of this difference is less than the value for the maximum difference, then the iteration process is stopped.

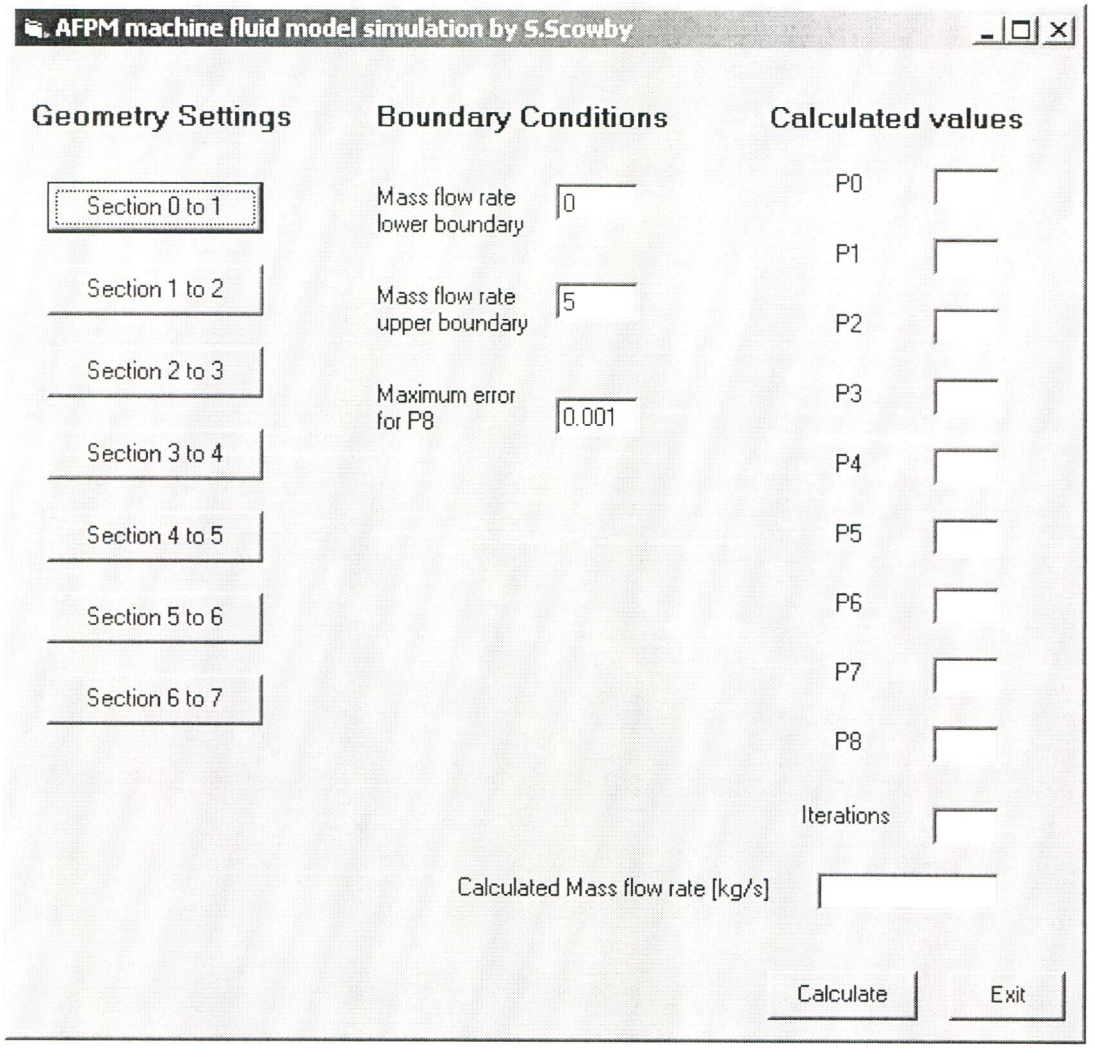

Figure B.1 Fluid simulation program

The next step in the fluid flow model is to set the geometry of the AFPM machine. The fluid flow model is based on the equations outlines in appendix D. The sections in the fluid flow model correspond to those shown in figure D.1. Section 0 to 1, figure B.2, is used to set the atmospheric conditions as well as the diameter of the bell mouth. The density is calculated using the ideal gas laws and the temperature and pressure entered by the user. The reference pressure refers to the pressure at point 0, all pressures are calculated relative to this pressure. The geometry of section 0 to 1 is shown in figure D.2. The dimensions for section 1 to 2 are shown in figure B.3, the dimensions are the same as those in figure D.3.

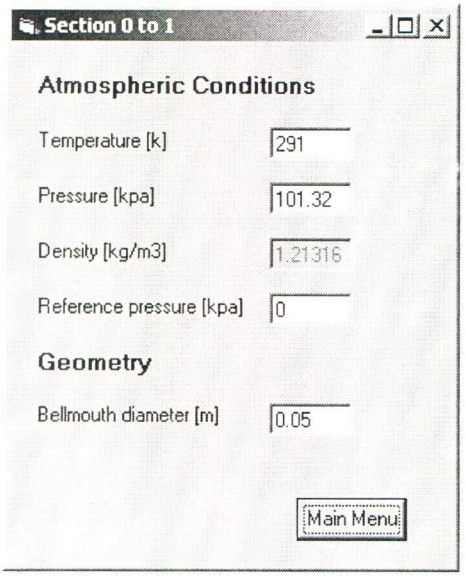

Figure B.2 Section 0 to1

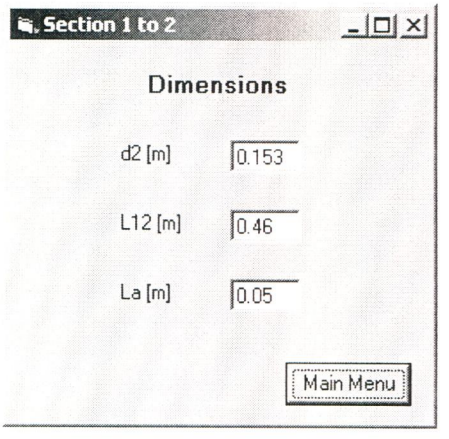

Figure B.3 Section 1 to 2

The dimensions for section 2 to 3, figure B.4, refer to the dimensions shown in figure D.5. The second entry, *Width of hub*, refers to dimension *h, Core diameter* refers to dimension d_c, *Blade width* refers to dimension *w,* all of figure D.4. *Stator thickness* refers to the thickness of the bottom piece of the stator. The dimensions for section 3 to 4 are shown in figure B.5. *Step* refers to the change in thickness of the rotor plates. *Stator thickness* refers to the thickness of the stator in the middle section. *Magnet angle* and *Gap angle* refer to the angles shown in figure D.8. The remaining sections are shown in figures B.6-8. The dimensions in these sections refer to the dimensions shown by the corresponding sections in appendix D.

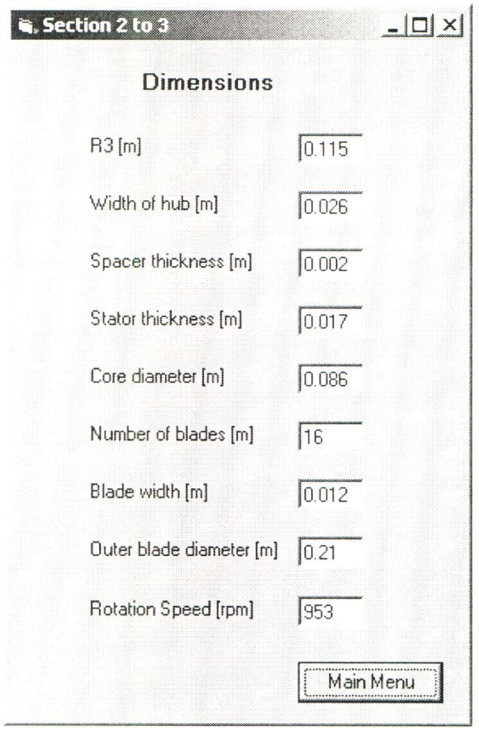

Figure B.4 Section 2 to 3

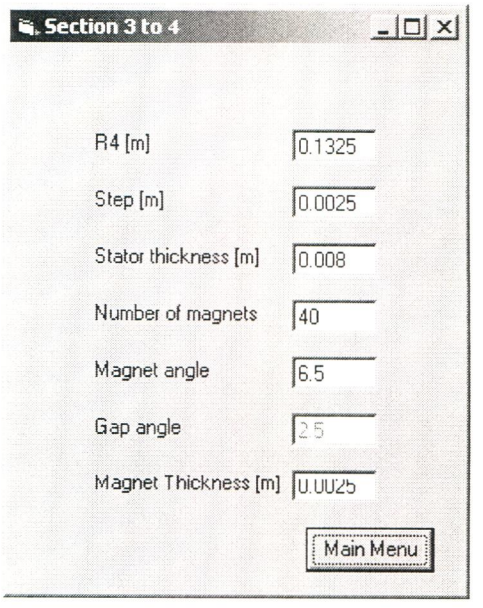

Figure B.5 Section 3 to 4

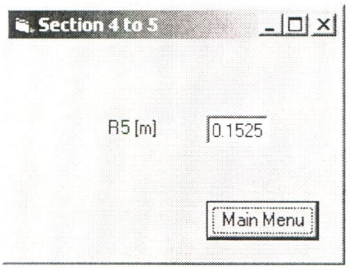

Figure B.6 Section 4 to 5

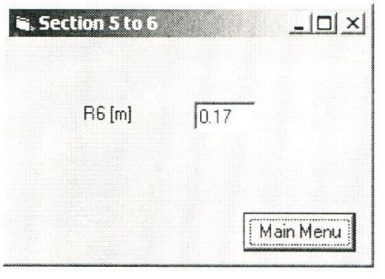

Figure B.7 Section 5 to 6

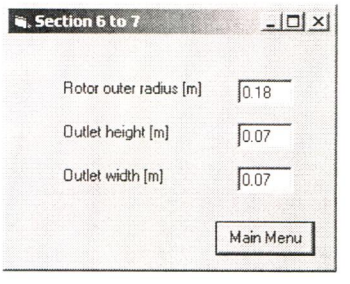

Figure B.8 Section 6 to 7

Once all the dimensions and the boundary conditions have been set, the pressures at each point as well as the mass flow rate are calculated by clicking on the button *Calculate*, figure B.9

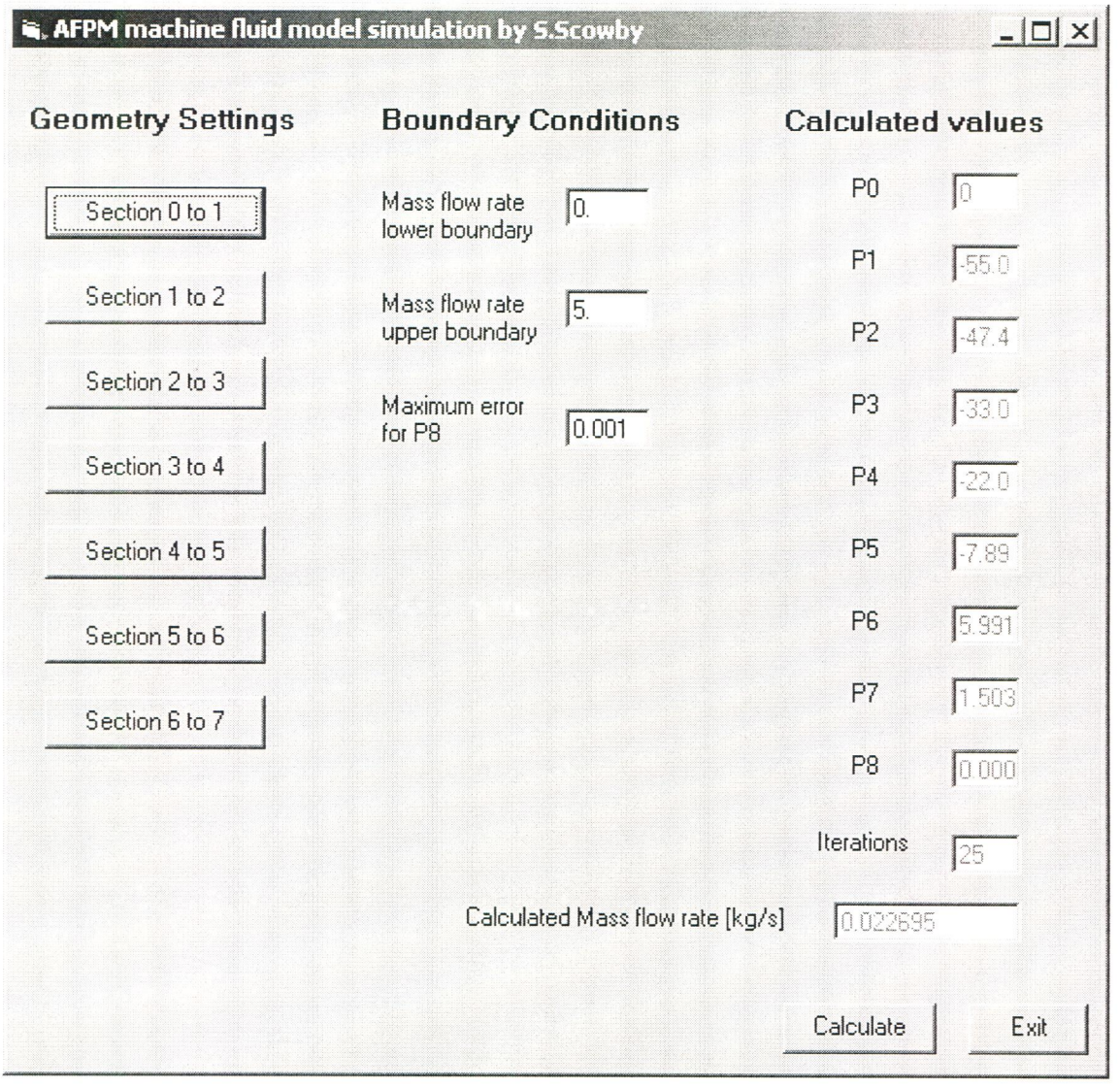

Figure B.9 Calculated pressures and mass flow rate

Thermal model

C.1 Introduction and objectives

The temperature distribution in the AFPM machine is calculated using the finite difference method as described in section 3.2.1. The thermal model allows the user to specify different mesh sizes. A finer mesh will result in a higher temperature resolution but will also increase the time required to complete the simulation. The temperature for each element at any time step is calculated according to equation 3.13. There are only two different types of elements in the thermal model, a boundary element and an internal element. Boundary elements have at least one of their surfaces exposed to the surrounding air whereas an internal element is surrounded by other elements either from the same component or from a different component. Should the internal element lie next to an element of another component then the conduction across this interface must be calculated according to an adjusted thermal conductivity. The objective of this section is to explain, in detail, the equations used in calculating the transient temperature response of the AFPM machine. This will be achieved by explaining the equations governing three typical elements, of the type mentioned above. Figure C.1 shows a cross section of the AFPM machine and the location of the selected elements.

C.2 Internal elements

Consider an internal element located within the stator surrounded by similar elements, element A of figure C.1. The governing equations of this element will be explained in detail as an example of any internal element found in the AFPM machine thermal model. The stator consists of two different materials, the copper wires and the epoxy used to bond the wires together. The material properties of any element in the stator are calculated according to the following equations: a void fraction for any element in the stator is calculated by

$$\alpha = \frac{V_{copper}}{V_{epoxy} + V_{copper}} \tag{C.1}$$

where V_{copper} is the volume of copper in the element and V_{epoxy} is the volume of epoxy. These volumes are dependant on the radius of the element within the stator; at the inner radius of the stator the copper wires are more densely populated and this will result in a higher void fraction than an element located at the outer radius of the stator. The calculation of the thermal

conductivity of these elements is calculated based on the volume ratio (void fraction) of the respective materials. With this in mind, the thermal conductivity of any element in the stator is calculated by

$$k_{eq} = \alpha k_{copper} + (1-\alpha)k_{epoxy} \tag{C.2}$$

The calculation of the the specific heat of these elements must be calculated based on the ratio of masses of the respective materials. A quality fraction for any element in the stator is given by

$$x = \frac{m_{copper}}{m_{copper} + m_{epoxy}} \tag{C.3}$$

where m_{copper} is the mass of copper and m_{epoxy} is the mass of epoxy. From this quality fraction the specific heat of any element in the stator is given by

$$c_{p,eq} = xc_{p,copper} + (1-x)c_{p,epoxy} \tag{C.4}$$

The stator is the only component in the AFPM machine that is manufactured from two different materials. Due to the fact that the thermal model was based on θ symmetry, certain components were modelled by solid discs, such as the rotor hub and magnets, as explained in section 3.2.2. The material properties of elements in these components were calculated using the equations explained above.

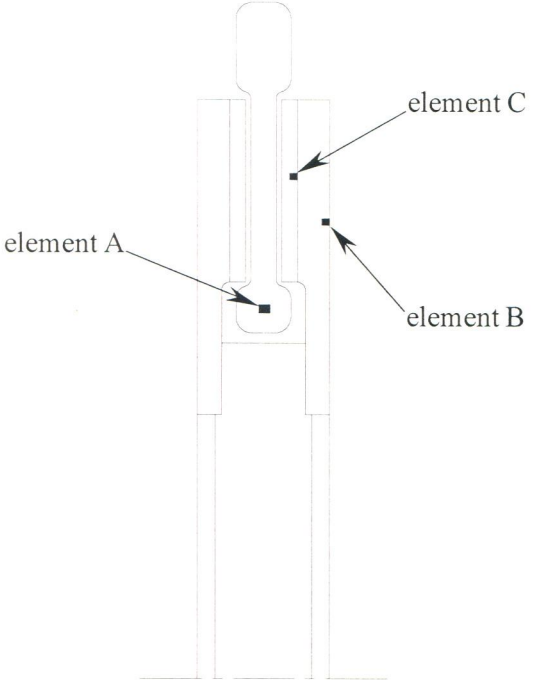

Figure C.1 Cross section of the AFPM machine and the selected elements

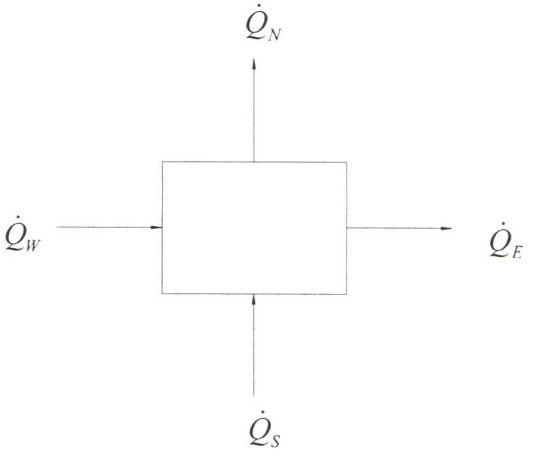

Figure C.2 An internal element in the stator and its associated heat fluxes

Consider the heat fluxes associated with this element, as shown by figure C.2. For convenience the faces of the element are denoted with the use of compass directions (N, S, E and W). Because

element A is an internal element, all of the heat fluxes entering/leaving this element are due to conduction only. Using the equivalent conduction of each internal element, as given by equation (C.2), the conduction heat fluxes are evaluated by

$$\dot{Q}_N = -k_{eq}(\Delta z \cdot \Delta d)\frac{T^i_{m,n+1} - T^i_{m,n}}{\Delta r} \tag{C.5}$$

$$\dot{Q}_W = -k_{eq}(\Delta r \cdot \Delta d)\frac{T^i_{m,n} - T^i_{m-1,n}}{\Delta z} \tag{C.6}$$

$$\dot{Q}_S = -k_{eq}(\Delta z \cdot \Delta d)\frac{T^i_{m,n} - T^i_{m,n-1}}{\Delta r} \tag{C.7}$$

$$\dot{Q}_E = -k_{eq}(\Delta r \cdot \Delta d)\frac{T^i_{m+1,n} - T^i_{m,n}}{\Delta z} \tag{C.8}$$

where $T^i_{m,n}$ is the temperature of the element being considered, $T^i_{m,n+1}$ is the element above $T^i_{m,n}$, $T^i_{m-1,n}$ is the element to the left of $T^i_{m,n}$, $T^i_{m,n-1}$ is the element below $T^i_{m,n}$, and $T^i_{m+1,n}$ is the element to the right of $T^i_{m,n}$. All these temperatures are taken from the previous time step. Δr *and* Δz are the width and height of the element, as shown in figure 3.6. Δd is the depth of the element, calculated according to

$$\Delta d = \pi D_{m,n} \tag{C.9}$$

where $D_{m,n}$ is the diameter at which the element is located. The copper wires in the stator produce internal heat due to the eddy current losses. The internal heat generated in any element, $\dot{Q}_{\text{int}}$, in the stator is dependent on its position, because the copper wires are more densely populated at the inner radius, the internal heat generation for an element at the inner radius will be higher than for an element located at the outer radius of the stator.

With all the heat transfer rates evaluated, the temperature of any internal element in the stator, at the current time step is

$$T^{i+1}_{m,n} = T^i_{m,n} + \frac{\Delta t}{\rho c(\Delta z \cdot \Delta r \cdot \Delta d)}\left(\dot{Q}_W + \dot{Q}_S - \dot{Q}_N - \dot{Q}_E + \dot{Q}_{\text{int}}\right) \tag{C.10}$$

Equations (C.5-9) are applied to any internal element in the AFPM machine thermal model. If the component is manufactured from a composite material or if the component does not exhibit θ symmetry, then the material properties are calculated according to equations (C.1-4).

C.3 Boundary Elements

Consider an element located on the surface of the rotor plates, element B of figure C.1. The governing equations of this element will be explained in detail as an example of any boundary

element found in the AFPM machine thermal model. The rotor plates consist only of one material and they exhibit θ symmetry and therefore it is not necessary to make any adjustments to the material properties. The heat fluxes associated with this element are shown in figure C.3. This element is subjected to all three types of heat transfer modes. Radiation occurs from the exposed surface of the element to the surface of the opposite facing element on the adjacent component. Convection occurs from the exposed surface of the element to the surrounding air. Conduction takes place between the element and the surrounding elements in the rotor plate. The conduction heat fluxes from the North, West and South faces are evaluated according to

$$\dot{Q}_N = -k(\Delta z \cdot \Delta d)\frac{T^i_{m,n+1} - T^i_{m,n}}{\Delta r} \tag{C.11}$$

$$\dot{Q}_W = -k(\Delta r \cdot \Delta d)\frac{T^i_{m,n} - T^i_{m-1,n}}{\Delta z} \tag{C.12}$$

$$\dot{Q}_S = -k(\Delta z \cdot \Delta d)\frac{T^i_{m,n} - T^i_{m,n-1}}{\Delta r} \tag{C.13}$$

The heat flux from the East face consists of a radiation heat flux and a convection heat flux.

$$\dot{Q}_E = \dot{Q}_{E,convection} + \dot{Q}_{E,radiation} \tag{C.14}$$

The convection from the exposed surface of the element to the surrounding air cell is given by

$$Q_{E,convection} = h_{m,n} A_{E_{m,n}} (T^{i-1}_{m,n} - T^{i-1}_{air}) \tag{C.15}$$

where h is the convective heat transfer coefficient, $A_{E_{m,n}}$ is the exposed surface area on the East face of the element, $T^{i-1}_{m,n}$ is the temperature of the element at the previous time step and T^{i-1}_{air} is the temperature of the surrounding air element at the previous time step. $A_{E_{m,n}}$ is determined by

$$A_{E_{m,n}} = \Delta r(\pi D_{m,n}) \tag{C.16}$$

The determination of the convective heat transfer coefficient, $h_{m,n}$, is non trivial and involves solving the Navier Stokes equations. For this research project, the experimental data from two case studies was used to establish empirical equations for the convective heat transfer coefficient. These case studies are explained in sections E.5 and E.6. The convective heat transfer coefficient on the surface of the stator is given by

$$Nu(r,G^*) = a + br^* + c(r^*)^2 + dG^* + e(G^*)^2 + fr^*(G^*) + gr^*(G^*)^2 + h(r^*)^2 G + i(r^*)^2 (G^*)^2 \tag{C.17}$$

where the values of the constants are shown in table E.2. The convective heat transfer coefficient on the surface of the rotor plates is given by

$$Nu = 9.83 \cdot 10^{-3} (G^*)^{-0.28} \cdot \mathrm{Re}_\theta^{\,0.755} \tag{C.18}$$

Both of these correlations are seen to be dependant only on the dimensionless gap ratio, G^*, and the dimensionless radius, r^*. When equation C.17 was used in the thermal model the results did not correlate well with experimental data. Equation C.18 was then used for the convective heat

transfer coefficient on the surface of the stator and the results correlated well. The peripheral Reynolds number is evaluated according to

$$\mathrm{Re}_\theta = \frac{\rho \omega b^2}{\mu} \tag{C.19}$$

Where b is the outer radius of the rotor plates. The dimensionless Gap ratio is dependent not only on the radial position of the boundary element but also its location within the AFPM machine. The gap ratio of a boundary element between the rotor plates and the shroud and the gap ratio of a boundary element between the rotor plates and the stator will differ. The convective heat transfer from the exposed surface of a boundary element is evaluated according to equations (C.15-19).

The radiation from the East surface is briefly discussed in section 4.2.2 and is expanded here for completeness. With element B in mind, consider the radiation between this element and the opposing elements on the surface of the shroud. The shroud is not shown in figure C.1. Say, for example, that there are 10 elements on this surface of the rotor plates and 10 elements on the surface of the shroud. These two surfaces can be approximated by an enclosure of 20 surfaces. Assume that these surface act according to the definition of a diffuse gray surface. The irradiation of surface i is

$$G_i = \sum_{n=1}^{20} J_n F_{in} \tag{C.20}$$

where J_n is the radiosity of surface i and is given by

$$J_i = \varepsilon_i E_{bi} + (1-\varepsilon_i) G_i \tag{C.21}$$

where E_{bi} is the black body emissive power. If all the temperatures are specified then $E_{bn} = \sigma T_n^4$. Substituting equation C.21 into C.20 gives

$$J_i = \varepsilon_i E_{bi} + (1-\varepsilon_i) \sum_{n=1}^{20} J_n F_{in} \tag{C.22}$$

Equation C.22 is a system of 20 linear equations in the 20 unknowns J_i. Upon solving and obtaining J_i, the radiant heat transfer from each surface is obtained from

$$\dot{Q}_i = \frac{\varepsilon_i A_i}{1-\varepsilon_i} (E_{bi} - J_i) \tag{C.23}$$

This normally would not present any calculation difficulty assuming that the form factor between each element and the remaining 19 elements is known. The form factor is defined as the fraction of radiation leaving a black surface A_1 that is intercepted by surface A_2. The form factor is a geometrical concept that depends only on the size, shape and orientation of the surfaces. The calculation of the form factor requires the evaluation of a double surface integral

$$F_{12} = \frac{1}{A_1}\int_{A_1}\int_{A_2}\frac{\cos\theta_1 \cos\theta_2}{\pi L^2} dA_2 dA_1 \qquad \text{(C.24)}$$

where θ_1 is the angle subtended by the normal of the differential area and the line connecting the two differential areas, θ_2 is the corresponding angle on the second differential area and L is the length of the connecting line as shown in figure C.4. Unless the geometry is very simple, analytical evaluation of this double integral is a challenging mathematical problem. The radiation in the thermal model was not modelled according to this method; a simpler yet efficient method was used and is illustrated in the following paragraphs.

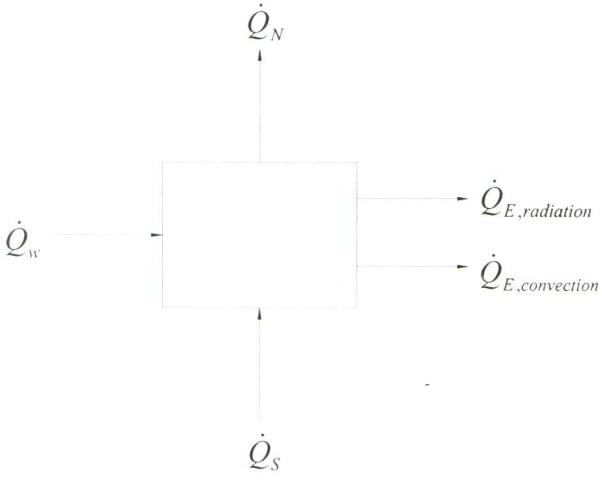

Figure C.3 A boundary element in one of the rotor plates and its associated heat fluxes.

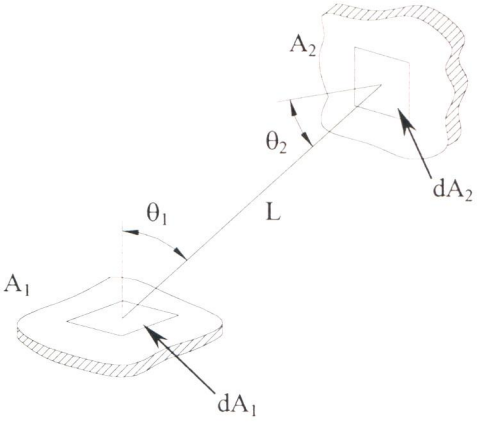

Figure C.4 Geometry for form factor formula.

The method used to calculate the radiation from the surface of a boundary element is best illustrated with the use of an example calculation. Consider two surfaces, one surface of a rotor plate and one surface of the stator with ten elements along the length of each surface. The two surfaces, with elements and corresponding elemental temperatures are shown in figure C.5. The average temperature of the ten elements on the surface of the stator is 361 K and that of the ten elements on the surface of the rotor plate is 309 K. For the purpose of this example assume that the total exposed area of the elements of the stator, A_{stator}, is 0.1 m^2 which must also be equal to the exposed area on the surface of the rotor plate, A_{rotor}. Assume also that the emissitivity of the stator, ε_{stator} and the rotor plate, ε_{rotor}, is 0.9 Therefore the net radiation from the stator to the rotor plate is

$$\dot{Q}_{stator-rotor} = \frac{\sigma\left(T_{stator}^4 - T_{rotor}^4\right)}{\frac{1-\varepsilon_{stator}}{\varepsilon_{stator} A_{stator}} + \frac{1}{A_{stator} F_{stator-rotor}} + \frac{1-\varepsilon_{rotor}}{\varepsilon_{rotor} A_{rotor}}} \qquad \text{(C.25)}$$

In this equation, the form factor is still present. If one considers the geometry in the AFPM machine, it would be a reasonable assumption to let the form factor for all radiation exchange calculations to be equal to unity. This is because the surfaces of the AFPM are all located in close proximity of each other. Consider the stator and one of the rotor plates. The outside diameter is 720 mm with an axial gap of 6.5 mm. The majority of the radiation which leaves the stator will be intercepted by the rotor plate and that which is not will be intercepted by another component of the AFPM machine. With this assumption, the total radiation exchange between the stator and the rotor plate is 36.49 W. This is the total radiation between all of the elements of the stator and all of the elements of the rotor plate. The radiation per element is calculated by dividing the total radiation by the number of elements. Therefore the net radiation leaving an element on the surface of the stator, is 3.649 W and the net radiation falling on an element on the surface of the rotor plate is 3.649 W. With all the heat fluxes evaluated, the temperature of any boundary element in the AFPM machine at the current time step is given by

$$T_{m,n}^{i+1} = T_{m,n}^{i} + \frac{\Delta t}{\rho c(\Delta z \cdot \Delta r \cdot \Delta d)}\left(\dot{Q}_W + \dot{Q}_S - \dot{Q}_N - \dot{Q}_E + \dot{Q}_{\text{int}}\right) \tag{C.26}$$

If the boundary element is not located in the stator then the internal heat generation term, $\dot{Q}_{\text{int}}$, is removed from this equation.

Stator	Rotor plate
352	300
354	302
356	304
358	306
360	308
362	310
364	312
366	314
368	316
370	318

Figure C.5 The elements of the stator and the rotor plate and their corresponding elemental temperatures.

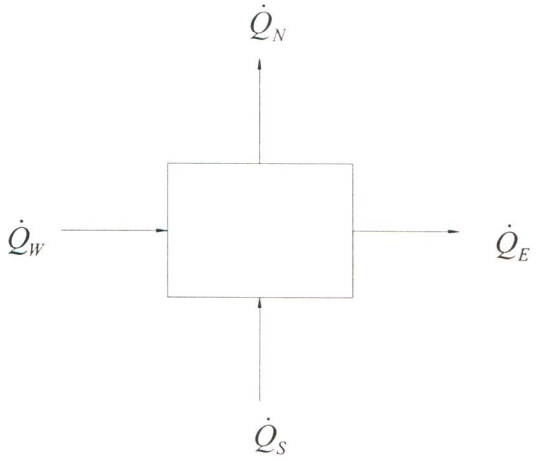

Figure C.6 An interface element between the magnets and a rotor plate and its associated heat fluxes.

C.4 Interface elements

Consider an element located on the interface between the magnets and the rotor plate, element C of figure C.1. Interface elements exist on either side of the interface between the magnets and the rotor plates, the rotor plates and the rotor hub, the rotor hub and the shaft, and the bearings and the shaft. The governing equations of element C will be explained in detail as an example of any interface element found in the AFPM machine. Conduction occurs across the interface of the dissimilar materials. The thermal conductivity will be different on either side of the interface. To evaluate the conduction across this interface, an equivalent thermal conductivity is calculated according to

$$k_{eq} = \frac{\left(k_{m,n}\Delta z_{m,n} + k_{m+1,n}\Delta z_{m+1,n}\right)}{\Delta z_{m,n} + \Delta z_{m+1,n}} \tag{C.27}$$

where $k_{m,n}$ is the thermal conductivity of the element in the magnets, $k_{m+1,n}$ is the thermal conductivity of the element in the rotor plate which lies on the other side of the interface, $\Delta z_{m,n}$ is the width of the element in the magnets and $\Delta z_{m+1,n}$ is the width of the element in the rotor plate. The conduction heat fluxes for the element are evaluated by

$$\dot{Q}_N \Delta t = -k\left(\Delta z \cdot \Delta d\right)\frac{T^i_{m,n+1} - T^i_{m,n}}{\Delta r}\Delta t \tag{C.28}$$

$$\dot{Q}_W \Delta t = -k\left(\Delta r \cdot \Delta d\right)\frac{T^i_{m,n} - T^i_{m-1,n}}{\Delta z}\Delta t \tag{C.29}$$

$$\dot{Q}_S \Delta t = -k\left(\Delta z \cdot \Delta d\right)\frac{T^i_{m,n} - T^i_{m,n-1}}{\Delta r}\Delta t \tag{C.30}$$

$$\dot{Q}_E \Delta t = -k_{eq}\left(\Delta r \cdot \Delta d\right)\frac{T^i_{m+1,n} - T^i_{m,n}}{\Delta z}\Delta t \tag{C.31}$$

The temperature of any interface element in the AFPM machine at the current time step is given by

$$T^{i+1}_{m,n} = T^i_{m,n} + \frac{\Delta t}{\rho c\left(\Delta z \cdot \Delta r \cdot \Delta d\right)}\left(\dot{Q}_W + \dot{Q}_S - \dot{Q}_N - \dot{Q}_E\right) \tag{C.32}$$

These equations are used to evaluate the heat fluxes and new temperature of any interface element found in the AFPM machine.

C.5 Material properties

The material properties of the components in the AFPM thermal model are presented here. The stator consists of copper wires and epoxy. The material properties of the copper wire and the epoxy is shown in tables C.1 ad C.2.

Table C.1 Material properties of the copper wire (Mills,1995).

Conductivity [W/mK]	400
Density [kg/m^3]	8933
Specific heat [J/kgK]	385

Table C.2 Material properties of the epoxy (Wang, 2002).

Conductivity [W/mK]	0.17
Density [kg/m^3]	1100
Specific heat [J/kgK]	1700

The material properties for the magnets, rotor plates and the rotor hub are shown in tables C.3-5 respectively.

Table C.3 Material properties of the magnets (Wang, 2002).

Conductivity [W/mK]	9
Density [kg/m^3]	7400
Specific heat [J/kgK]	420

Table C.4 Material properties of the rotor plates (Mills, 1995).

Conductivity [W/mK]	50
Density [kg/m^3]	7800
Specific heat [J/kgK]	450

Table C.5 Material properties of the rotor hub (Mills, 1995).

Conductivity [W/mK]	50
Density [kg/m^3]	7800
Specific heat [J/kgK]	450

C.6 Discussions and conclusion

In this chapter the governing equations of three typical elements were explained in detail. Each of these elements was an example of an internal element, a boundary element and an interface element. Modelling the radiation presents a large mathematical problem in calculating the form factor. Assumptions were made in the thermal model which alleviated this problem. Every element in the AFPM machine is modelled by one of the three elements explained in the above sections. The values of the material properties were shown. These values are for the current prototype AFPM machine and can be changed in the thermal model. The modelling of the heat pipe was not presented here. This is shown in section G.8.

Appendix D

Theoretical fluid flow model and experimentally determined energy loss coefficients

The AFPM machine can be seen as a fan or pump system. For the purpose of this research the flow channel will be modelled similarly to the method used in one-dimensional pipe systems. Friction as well as other system losses, for example the energy loss due to the sudden expansion in flow area, will be accounted for. Energy (pressure) gains due to the radial blades in the rotor hub as well as the energy gain due to the "viscous pumping" experienced between the rotor plates and the stator will also be accounted for.

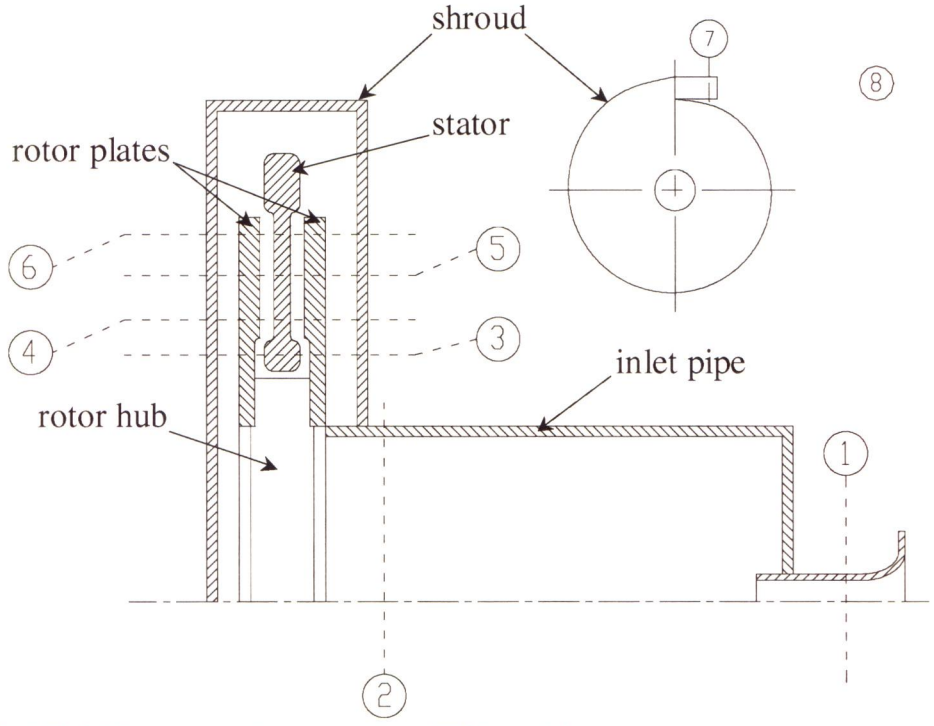

Figure D.1 Fluid flow channel through the AFPM machine

The air enters through the bell mouth at point 1. After the bell mouth the air enters the inlet pipe, which is located between points 1 and 2. The air enters the AFPM machine through the radial blades of the rotor hub. There are 16 radial blades in the rotor hub. A pressure gain is experienced over this section due to the rotating radial blades. Just before point 3 the air channel is split into two separate and smaller channels, on either side of the stator. Points 3,4,5 and 6 then describe the fluid as it flows through the narrow radial passage between the stator and the rotor plates. As the air leaves the rotor-stator channel it is directed into the shroud area. From the shroud area it is forced into the shroud outlet, point 7, where it is dumped into the atmosphere, point 8.

Section 0 to 1

This section simulates the part where the air enters the bell mouth and is directed into the inlet pipe. This section is shown in more detail in figure D.2.

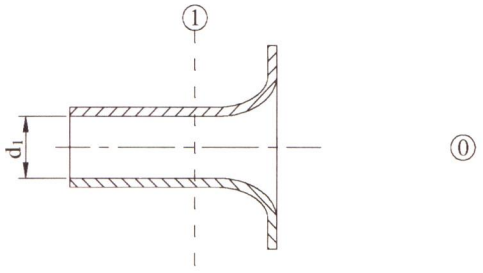

Figure D.2 Section 0

Due to the definition of a bell mouth there are no losses associated with this section of the flow path. The average velocity through the bell mouth is given by

$$V_1 = \sqrt{\frac{2(p_0 - p_1)}{\rho}} \tag{D.1}$$

The volume and mass flow rates through the system are given by the equations D.2 and D.3 respectively

$$G = V_1 A_1 \tag{D.2}$$

where A_1 is the flow area at point 1.

$$\dot{m} = \rho G \tag{D.3}$$

Section 1 to 2

This section describes the flow from the exit of the bell mouth to the inlet of the AFPM machine, see figure D.3. There is a pressure loss due to the sudden expansion in flow area from the outlet of the bell mouth to the inlet of the inlet pipe. A pressure loss is also experienced due to the friction in the pipe.

Sudden expansion loss, k_{se}:

This loss factor was determined experimentally; the experimental values are shown in figure D.4. The average value of this loss coefficient is k_{se} = 0.85. The pressure loss due to the sudden expansion is based on the average velocity in the bell mouth, V_1, and is given by

$$\Delta p_{minor12} = k_{se} \frac{\rho V_1^2}{2} \tag{D.4}$$

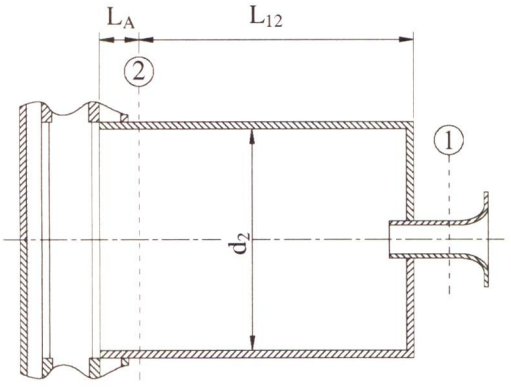

Figure D.3 Section 1 to 2.

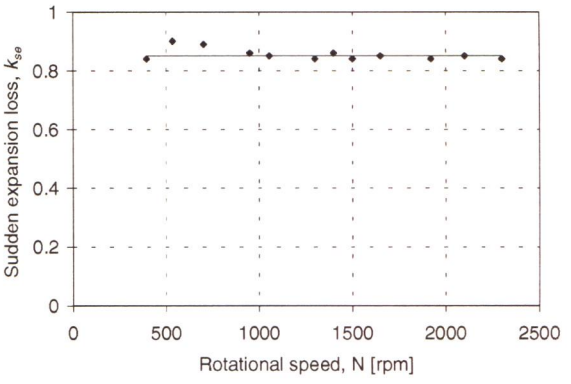

Figure D.4 Loss coefficient, k_{se}, plotted against different rotational speeds.

Energy loss coefficient, k_{pipe12}:

The friction loss as the air flows through the inlet pipe is based on the average velocity at point 2 and is given by

$$\Delta p_{pipe12} = k_{pipe12}\rho\frac{V_2^2}{2} \tag{D.5}$$

where

$$V_2 = \frac{G}{\frac{\pi}{4}d_2^2} \tag{D.6}$$

The Reynolds number at point 2 is given by

$$\mathrm{Re} = \frac{\rho V_2 d_2}{\mu} \tag{D.7}$$

The Darcy friction factor can be determined for this section. This is done by taking two intervals for certain Reynolds number values.

If $\mathrm{Re} < 1180$:

$$f = \frac{64}{\mathrm{Re}} \tag{D.8}$$

If $\mathrm{Re} \geq 1180$:

$$f = 0.316\mathrm{Re}^{-0.25} \tag{D.9}$$

The energy loss coefficient due to friction can now be determined by

$$k_{pipe12} = \frac{f_{12}L_{12}}{d_2} \tag{D.10}$$

where L_{12} is the length of the inlet pipe from point 1 to point 2 as in figure D.3. The pressure loss between section 1 and 2 is given by

$$\Delta p_{loss12} = \Delta p_{minor12} + \Delta p_{pipe12} \tag{D.11}$$

The pressure at point 2 can now be calculated from equation D.13.

$$p_2 = p_1 + \rho\frac{V_1^2}{2} - \Delta p_{loss12} - \rho\frac{V_2^2}{2} \tag{D.12}$$

Section 2 to 3

This section describes the flow path from the end of the inlet pipe to just after the start of the stator. There is an energy loss due to the friction associated with the flow path. The flow patterns associated with this section of the flow path are very complicated and difficult to analyse in theory. There is one minor loss factor for this section, k_{23}. This loss coefficient is the accumulation of several different minor losses. The inlet to the radial blades of the rotor hub results in a large loss in energy, which is similar to the *shock loss* (Sayers, 1990) in turbo machinery. The outlet of the radial blades also exhibits a loss, which can be compared to the *slip loss* (Sayers, 1990) in turbo machinery. The radial blades rotate the air and thus impart energy into the air. There is also a loss due to the many different changes in flow area between points 2 and 3.

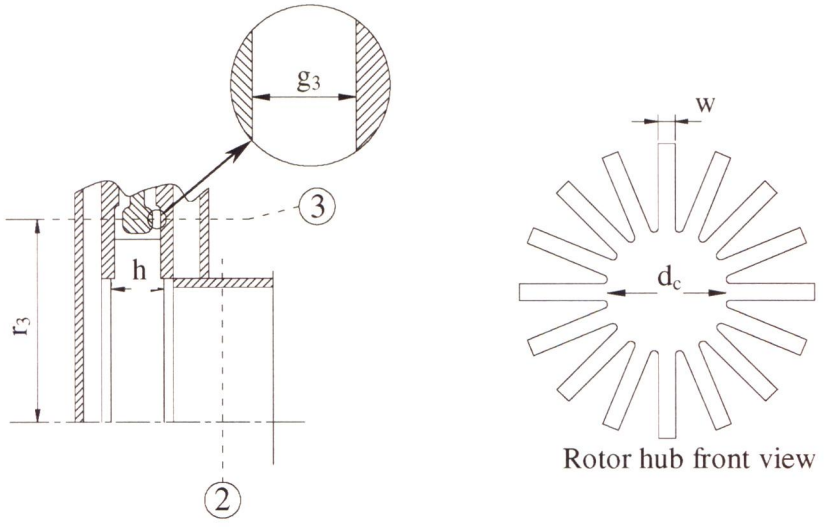

Figure D.5 Section 2 to 3

Minor losses, k_{23}:

This loss coefficient accounts for the numerous minor losses, mentioned above, in the flow path from point 2 to point 3. This minor loss is based on the average velocity at point 3. The flow channel is split into two separate channels just before point three. These flow channels are of identical geometry. It is assumed in this fluid flow model that the mass flow rate in each of these

separate flow channels is equal to half of the total mass flow rate. The flow area at point 3 in one of the channels is given by

$$A_3 = 2\pi r_3 g_3 \tag{D.13}$$

where r_3 is the radius at point 3 and g_3 is the gap between the stator and the rotor plates at point 3. The average velocity at point 3 is given by

$$V_3 = \frac{\dot{m}}{2\rho A_3} \tag{D.14}$$

The minor pressure loss for section 2 to 3 is given by

$$\Delta p_{minor23} = k_{23} \frac{\rho V_3^2}{2} \tag{D.15}$$

The experimental values for the loss coefficient, k_{23}, are shown in figure D.6. As can be seen this loss coefficient was found to be dependent on the size of the gap as well as the size of the magnets.

Energy loss coefficient, k_{pipe23}:

The friction loss for section 2 to 3 is calculated by determining an equivalent pipe based on the average flow areas between these two points. From this an energy loss coefficient can be found from

$$k_{pipe23} = \frac{f_{23} L_{23}}{d_{23}} \tag{D.16}$$

The pressure loss due to the friction for this section is given by

$$\Delta p_{pipe23} = k_{pipe23} \frac{\rho V_{23}^2}{2} \tag{D.17}$$

where V_{23} is an equivalent velocity determined by using the mass flow rate and the equivalent pipe flow area. The pressure loss for section 2 to 3 is given by

$$\Delta p_{loss23} = \Delta p_{pipe23} + \Delta p_{minor23} \tag{D.18}$$

Work input, $\dot{W}_{in}$:

The radial blades impart a relatively large amount of energy into the air. The work input by radial blades for air entering the blade passage at r_1 and leaving the blade passage at r_2 is given by (Sayers, 1990 and White, 1994)

$$\dot{W}_{in} = \dot{m}\omega^2 \left(r_2^2 - r_1^2\right) \tag{D.19}$$

The rotor hub of the AFPM machine presents a slightly more difficult situation. As shown in figure D.7, the airflow does not entirely enter the blade passage at one radius. Instead the entry of the air into the blade passage is distributed over most of the length of the blade. The assumption was made to use a constant velocity profile at the inlet of the blade passage.

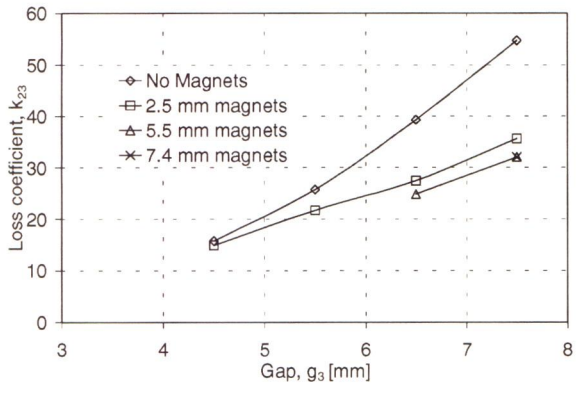

Figure D.6 Loss coefficient, k_{23}, plotted for different magnet and gap sizes

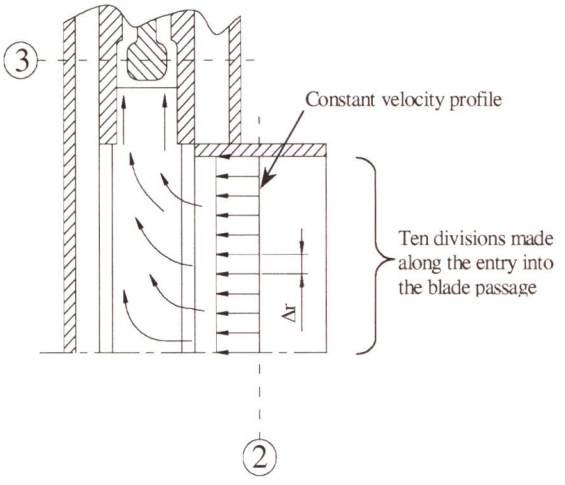

Figure D.7 Inlet to the radial blades of the rotor hub

The work input was calculated by dividing the length of the radial blade into equal divisions. With the assumption of a constant velocity profile at the inlet of the radial blades, the mass flow rate entering each of the divisions can be found. Equation D.19 can then be used to find the work input by the radial blades. The pressure gain over section 2 to 3 is then given by

$$\Delta p_{gain23} = \rho \frac{\dot{W}_{in}}{\dot{m}} \tag{D.20}$$

The pressure at point 3 can now be calculated from

$$p_3 = p_2 + \rho \frac{V_2^2}{2} + \Delta p_{gain23} - \Delta p_{loss12} - \rho \frac{V_3^2}{2} \tag{D.21}$$

Section 3 to 4

This section describes the flow from point 3 to point 4, which is located just after the change in thickness of the stator. There is a minor loss due to the slight bend in the flow channel, k_{bend}, as well as an energy loss due to the friction. There is an energy gain due to the viscous pumping experienced between the rotor and the stator. This section is shown in more detail in figure D.8.

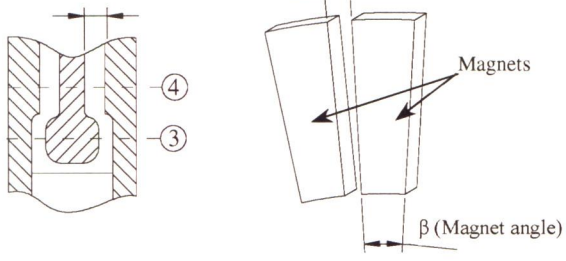

Figure D.8 Section 3 to 4.

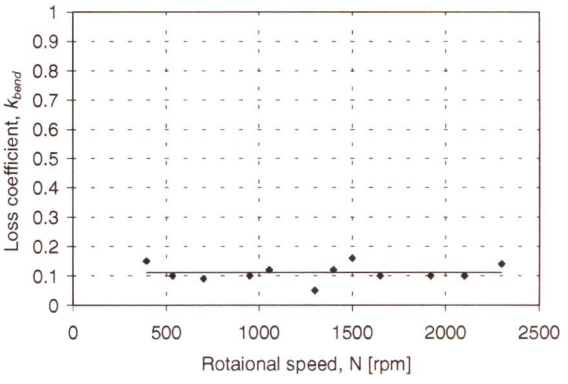

Figure D.9 Loss coefficient, k_{bend}, plotted against rotational speed.

Bend loss, k_{bend}:

The experimental values for this loss coefficient are shown in figure D.9. This loss coefficient was found to have a constant value of $k_{bend} = 0.11$. The pressure loss due to the bend is given by

$$\Delta p_{minor34} = k_{bend} \frac{\rho V_4^2}{2} \tag{D.22}$$

Energy loss coefficient, k_{pipe34}:

The energy loss due to friction for section 3 to 4 is calculated in the same way as that described in section 2 to 3. The average of the areas at points 3 and 4 is used to describe an equivalent pipe area between these points. Point 4 is located just after the start of the magnets; the area of the magnets must be taken into account when calculating the flow area. The flow area at point 4 is given by

$$A_4 = 2\pi r_4 g_4 - \frac{i\beta}{360} 2\pi r_4 t \tag{D.23}$$

where i is the number of magnets, β is the magnet angle, t is the magnet thickness and g_4 is the gap between the rotor plates and the stator as shown in figure D.7. The pressure loss due to friction is given by

$$\Delta p_{pipe34} = k_{pipe34} \rho \frac{V_{34}^2}{2} \tag{D.24}$$

where V_{34} is an equivalent velocity and k_{pipe34} is given by

$$k_{pipe34} = \frac{f_{34} L_{34}}{d_{34}} \tag{D.25}$$

where L_{34} is the difference in radius between point 4 and point 3. The pressure loss for section 3 to 4 is given by

$$\Delta p_{loss34} = \Delta p_{pipe34} + \Delta p_{minor34} \tag{D.26}$$

Viscous pumping:

The work input by viscous pumping, which is discussed in detail in Appendix E, is given by

$$\dot{W}_{viscous34} = C\frac{\dot{m}}{2}\omega^2\left(r_4^2 - r_3^2\right) \tag{D.27}$$

where C is an experimental correlation factor. The pressure gain for section 3 to 4 is given by

$$\Delta p_{gain34} = \rho\frac{\dot{W}_{viscous34}}{\dot{m}} \tag{D.28}$$

The pressure at point 4 can now be calculated from

$$p_4 = p_3 + \rho\frac{V_3^2}{2} + \Delta p_{gain34} - \Delta p_{loss34} - \rho\frac{V_4^2}{2} \tag{D.29}$$

Section 4 to 5

Section 4 to 5, figure D.10, describes the flow channel in the rotor stator region. The magnets are located in this region. There is a loss in energy due to friction and a work input due to the viscous pumping.

Energy loss coefficient, k_{pipe45}:

The loss in energy due to friction for section 4 to 5 is calculated by taking an equivalent pipe, as described in the previous sections. The flow area at points 5 is given by the equation

$$A_5 = 2\pi r_5 g_5 - \frac{i\beta}{360}2\pi r_5 t \tag{D.30}$$

The friction loss is given by

$$\Delta p_{pipe45} = k_{pipe45}\rho\frac{V_{45}^2}{2}$$

where V_{45} is an equivalent velocity and k_{pipe45} is given by

$$k_{pipe45} = \frac{f_{45}L_{45}}{d_{45}} \tag{D.31}$$

The pressure loss for section 4 to 5 is given by

$$\Delta p_{loss45} = \Delta p_{pipe45} \tag{D.32}$$

Viscous pumping:

The work input by viscous pumping for section 4 to 5 is given by

$$\dot{W}_{viscous45} = C\frac{\dot{m}}{2}\omega^2\left(r_5^2 - r_4^2\right) \tag{D.33}$$

The pressure gain for section 4 to 5 is given by

$$\Delta p_{gain45} = \rho\frac{\dot{W}_{viscous45}}{\dot{m}} \tag{D.34}$$

The pressure at point 5 can now be calculated from

$$p_5 = p_4 + \rho\frac{V_4^2}{2} + \Delta p_{gain45} - \Delta p_{loss45} - \rho\frac{V_5^2}{2} \tag{D.35}$$

Section 5 to 6

Section 5 to 6 is analysed in exactly the same manner as that for section 4 to 5. There is a loss in energy due to friction and a work input due to the viscous pumping.

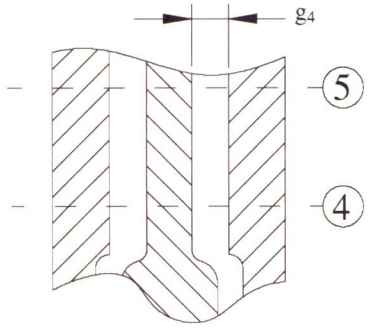

Figure D.10 Section 4 to 5

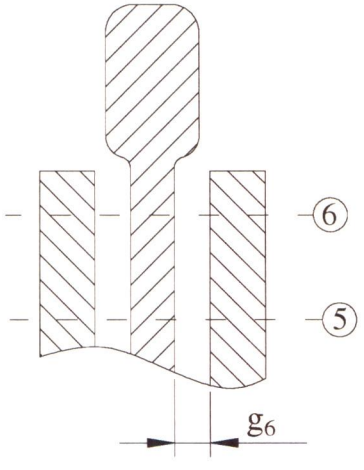

Figure D.11 Section 5 to 6

Energy loss coefficient, k_{pipe56}:

The loss in energy due to friction for section 5 to 6 is calculated by taking an equivalent pipe, as described in the previous sections. The flow area at points 6 is given by the equation

$$A_6 = 2\pi r_6 g_6 - \frac{i\beta}{360}2\pi r_6 t \tag{D.36}$$

A loss coefficient is calculated from

$$k_{pipe56} = \frac{f_{56}L_{56}}{d_{56}} \tag{D.37}$$

The pressure loss due to friction is given by

$$\Delta p_{pipe56} = k_{pipe56} \rho \frac{V_{45}^2}{2} \tag{D.38}$$

The pressure loss for section 5 to 6 is given by

$$\Delta p_{loss56} = \Delta p_{pipe56} \tag{D.39}$$

Viscous pumping:

The work input by viscous pumping for section 5 to 6 is given by

$$\dot{W}_{viscous56} = C \frac{\dot{m}}{2} \omega^2 \left(r_6^2 - r_5^2 \right) \tag{D.40}$$

The pressure gain for section 5 to 6 is given by

$$\Delta p_{gain56} = \rho \frac{\dot{W}_{viscous56}}{\dot{m}} \tag{D.41}$$

The pressure at point 6 can now be calculated from

$$p_6 = p_5 + \rho \frac{V_5^2}{2} + \Delta p_{gain56} - \Delta p_{loss56} - \rho \frac{V_6^2}{2} \tag{D.42}$$

Section 6 to 7

This section, figure D.12, describes the flow channel from just before the outer radius of the rotor plates to the discharge section of the shroud. There is a loss in energy due to friction in this region as well as a minor loss due to the many changes in flow area and direction for this section. There is work input by viscous pumping for the remaining section of the radial channel.

Exit loss, k_{exit}:

The experimental values for this loss coefficient are shown in figure D.12. The average value used for this loss coefficient was k_{exit} = 0.29. The pressure loss due to the exit minor losses is based on the average velocity at point 7 and is given by

$$\Delta p_{minor67} = k_{exit} \frac{\rho V_7^2}{2} \tag{D.43}$$

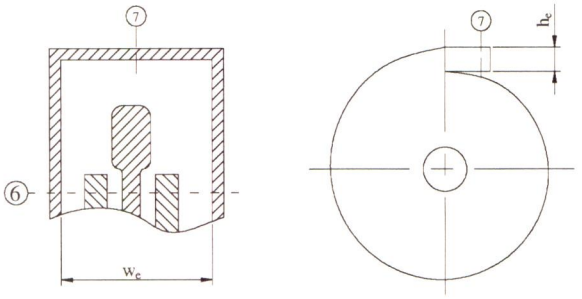

Figure D.12 Section 6 to 7

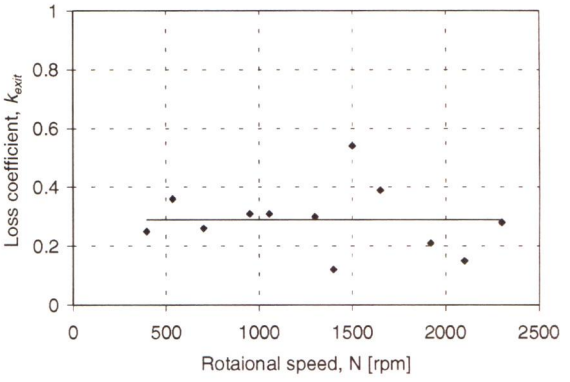

Figure D.13 Loss coefficient, k_{exit}, plotted

Energy loss coefficient, k_{pipe67}:

The calculation of the friction loss for this section was once again related to an equivalent pipe flow. The average flow area in the shroud was used to find an equivalent pipe diameter. The average flow area in the shroud is equal to half of the outlet area and is given by

$$A_{67} = \frac{h_e \cdot w_e}{2} \tag{D.43}$$

The pressure loss due to friction is given by

$$\Delta p_{friction67} = k_{friction67} \rho \frac{V_{67}^2}{2} \tag{D.44}$$

where

$$k_{friction67} = \frac{fL_{67}}{d_{67}} \tag{D.45}$$

The pressure loss for section 6 to 7 is given by

$$\Delta p_{loss67} = \Delta p_{pipe67} + \Delta p_{minor67} \tag{D.46}$$

Viscous pumping:

The work input by viscous pumping for section 6 to 7 is given by

$$\dot{W}_{viscous67} = C \frac{\dot{m}}{2} \omega^2 \left(r_p^2 - r_6^2 \right) \tag{D.47}$$

where r_p is the outer radius of the rotor plates. The pressure gain over this section is given by

$$\Delta p_{gain67} = \rho \frac{\dot{W}_{viscous67}}{\dot{m}} \tag{D.48}$$

The pressure at point 7 can now be calculated from

$$p_7 = p_6 + \rho\frac{V_6^2}{2} + \Delta p_{gain67} - \Delta p_{loss67} - \rho\frac{V_7^2}{2} \tag{D.49}$$

Section 7 to 8

This section describes the discharge of the flow to the atmosphere. Point 8 is located in the surrounding atmosphere and therefore will have the same value as the pressure at point 0, figure D.15. There is only a minor loss associated with this section, namely the sudden expansion into an infinitely large area. This loss factor, k_{outlet}, was determined experimentally and is shown in figure D.14. The value used for this loss coefficient was k_{outlet} = 1.17. The pressure loss for this section is given by

$$\Delta p_{loss78} = k_{outlet}\rho\frac{V_7^2}{2} \tag{D.50}$$

The pressure at point 8 is given by

$$p_8 = p_7 + \rho\frac{V_7^2}{2} - \Delta p_{loss78} \tag{D.51}$$

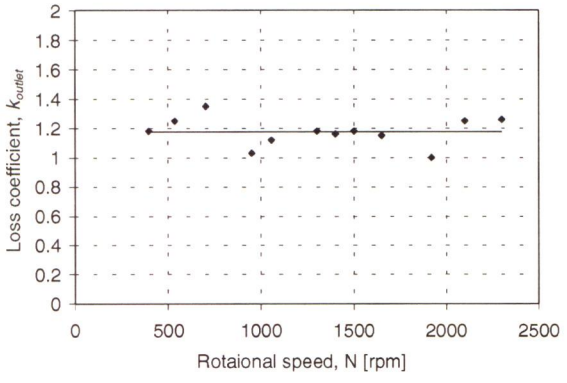

Figure D.14 Loss coefficient, k_{outlet}, plotted against different rotational speeds.

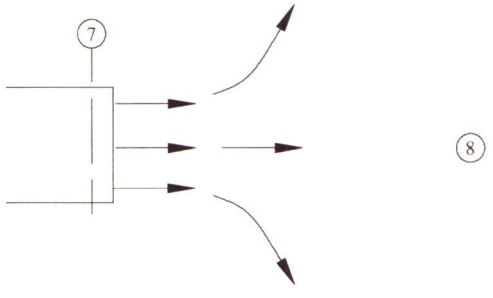

Figure D.15 Section 7 to 8.

Rotor-stator systems

E.1 Introduction and objectives

The detailed knowledge of the flow structure and heat transfer process inside the AFPM machine is of crucial interest for the thermal management of the AFPM machine. Rotating disc systems can often serve as the model for the flow and heat transfer that occurs within the AFPM machine. As shown in figure E.1, the AFPM machine provides two examples of this: the air-cooled rotor plates rotating near the stator can be modelled by a simple rotor-stator system; the same applies for the region between the rotor plates and the shroud. In order to calculate the temperatures in the AFPM machine, knowledge of the heat transfer coefficients between the surface of the rotating disc and the surrounding air is required. The object of this section is to produce a better understanding of the flow and heat transfer process occurring in the AFPM machine.

E.2 The free disc

Figure E.2 shows a simple schematic representation of the free disc. This simple model serves as the first 'building block' with which to begin the synthesis of more complex rotating disc systems. Flow is entrained into a boundary layer on the rotating disc and the tangential component of velocity, V_ϕ, (relative to a stationary frame of reference) is sheared from a value of Ωr on the disc surface to zero outside the boundary layer. Transition from laminar to turbulent flow occurs at $(r/b)^2 \,\mathrm{Re}_\theta \approx 3x10^5$ where $\mathrm{Re}_\theta \equiv \rho\Omega b^2/\mu$. For laminar flow, the boundary layer thickness, δ, is independent of radial location, and

$$\delta \approx 4\left(\frac{\nu}{\Omega}\right)^{\frac{1}{2}} \tag{E.1}$$

where δ is the axial location where $\left(V_\phi/\Omega r\right) = 0.026$. The moment coefficient on one side of the disc is given by

$$C_m = 1.935\,\mathrm{Re}_\theta^{-0.5} \tag{E.2}$$

where

$$C_m \equiv \frac{M}{\frac{1}{2}\rho\Omega^2 b^5}$$

M is the frictional moment generated on one side of the disc. The dimensionless flow rate, $C_{w,ent}$, where $C_{w,ent} \equiv Q_{ent}/\nu b$ and Q_{ent} is the volumetric flow rate entrained, or 'pumped', by one side of the disc, is given by

$$C_{w,ent} = 2.78 \mathrm{Re}_{\theta}^{\frac{1}{2}} \tag{E.3}$$

For turbulent flow the following correlations are applicable

$$\frac{\delta}{r} = 0.525 \left(\left(\frac{r}{b} \right)^2 \mathrm{Re}_{\theta} \right)^{-0.2} \tag{E.4}$$

$$C_m = 0.073 \mathrm{Re}_{\theta}^{-0.2} \tag{E.5}$$

$$C_{w,ent} = 0.219 \mathrm{Re}_{\theta}^{0.8} \tag{E.6}$$

A more accurate expression for C_m, which agrees well with measured values up to $\mathrm{Re}_{\theta} \approx 7x10^6$, is

$$C_m = 0.491 (\log_{10} \mathrm{Re}_{\theta})^{-2.58} \tag{E.7}$$

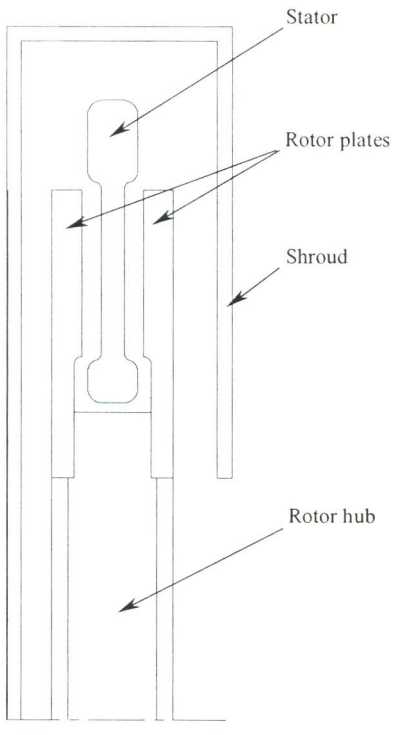

Figure E.1 Cross Section of the AFPM machine

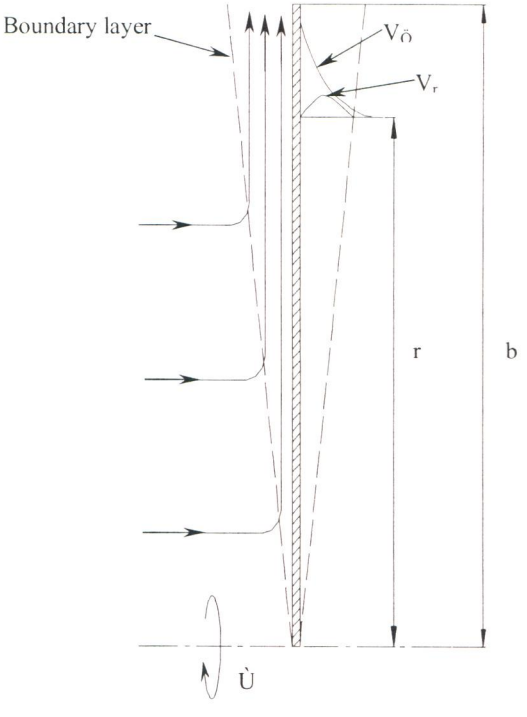

Figure E.2 Schematic of boundary-layer flow on the free disc

In the case of a disc rotating in free air, with a power law temperature profile $T(r) = T_\infty + cr^n$, the following correlations give the local Nusselt number (Harmand *et al*, 1999):

$$Nu = 0.221\sqrt{n+2}(\mathrm{Re})^{0.5} \tag{E.8}$$

for the laminar flow $(\mathrm{Re} \le 1.82 \cdot 10^5)$ and

$$Nu = 0.0169(n+2.6)^{0.2}(\mathrm{Re})^{0.8} \tag{E.9}$$

for the turbulent flow $(\mathrm{Re} \le 2.82 \cdot 10^5)$

E.3 Rotor-stator systems

Schematic diagrams of enclosed, open (or 'partially enclosed') and shrouded rotor-stator systems are shown in figure E.3. These systems can be used to model the type of flow that occurs when a disc rotates near to a stationary casing with or without superimposed flow. In the limiting case where there is no superimposed flow and the casing is removed, the systems reduce to the free disc.

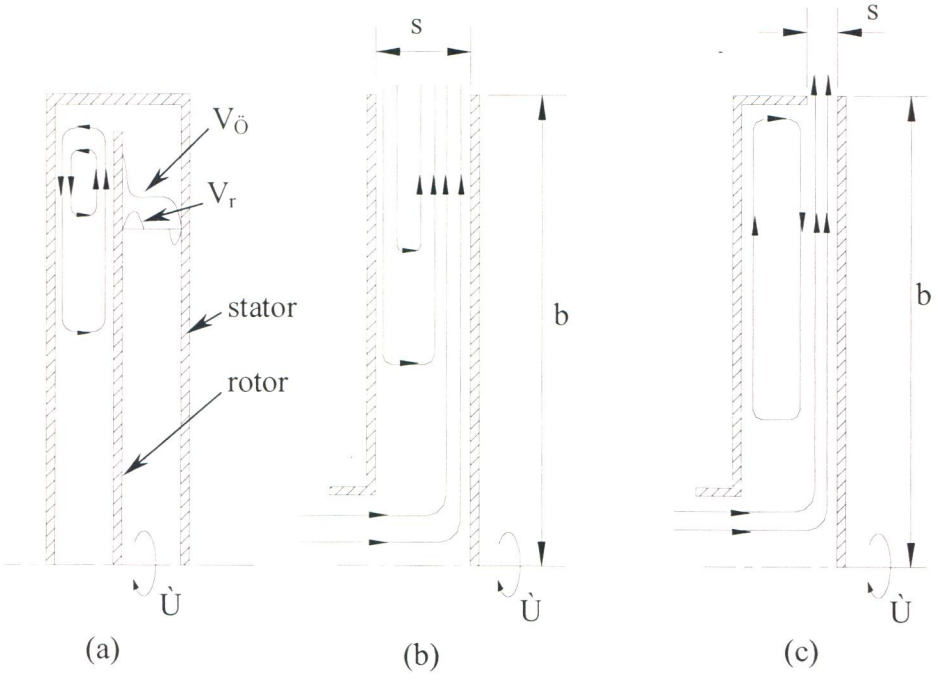

Figure E.3 Schematic diagram of flow in rotor-stator systems: (a) enclosed disc; (b) open rotor-stator; (c) shrouded rotor-stator

The system, which most resembles that in the AFPM machine, is the open rotor-stator system; figure E.3 (b). Therefore only this system will be looked at in detail in the following sections. In the open (or 'partially-enclosed') system, figure E.3 (b), fluid can be supplied at the centre to simulate an air-cooled disc. For the case of zero superimposed flow and an infinite gap between the rotor and stator, the flow will be the same as that for the free disc. However, as the gap is

reduced (the superimposed flow still being zero), the fluid entrained into the boundary layer on the rotor is supplied by the inflow down the stator. The *gap ratio* for rotor stator systems is defined as

$$G^* = \frac{s}{b}$$

where s is the gap between the rotor and the stator and b is the outer radius of the system.

At large values of G^*, the boundary layers will remain separate. If the gap is reduced below a certain value of G^* ($G^* = G^*_{max}$) the layers will start to interact. This interaction will restrict the flow entrained by the rotor and thereby reduce the momentum efflux in its boundary layer. Therefore, for $G^* < G^*_{max}$, there will be a tendency for the moment coefficient (and, by analogy, the nusselt number) to be reduced. If the gap is further reduced below a limiting value of G^* ($G^* = G^*_{min}$), Couette flow will occur and the moment coefficient and Nusselt number will start to increase with decreasing G^*. This effect is shown in figure E.4 which indicates the general variation of C_m and Nu_{av} with G^*. An estimate of G^*_{max} is given by (Owen, 1989)

$$G^*_{max} = 1.05\,\mathrm{Re}_\theta^{-0.2} \qquad \text{(E.10)}$$

and that for G^*_{min} is

$$G^*_{min} = 0.23\,\mathrm{Re}_\theta^{-0.2} \qquad \text{(E.11)}$$

E.4 Rotor-stator flow regimes

In the case of rotor-stator systems Owen (1989) distinguished four flow regimes depending on the rotational speed and gap between the disc and the stator as shown in figure E.5. Regime I corresponds to laminar boundary layers on the two parallel surfaces which touch and give rise to the low gap ratio, G. Regime II is obtained for high G values, when there are two laminar boundary layers, one on the rotor and another on the stator are separated by a core of fluid rotating at approximately 0.4Ω. Regimes III and IV are respectively equivalent to regimes I and II but for turbulent boundary layers.

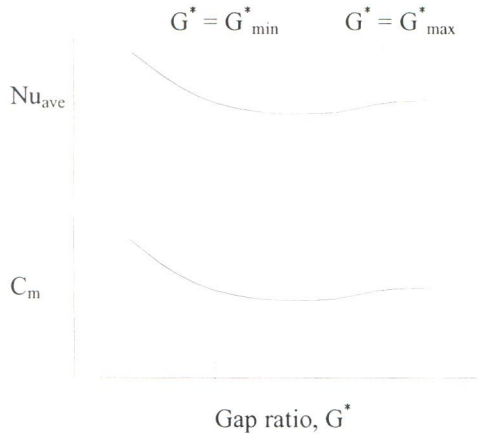

Figure E.4 The effect of the gap ratio on the average Nusselt number and moment coefficient (Owen, 1989).

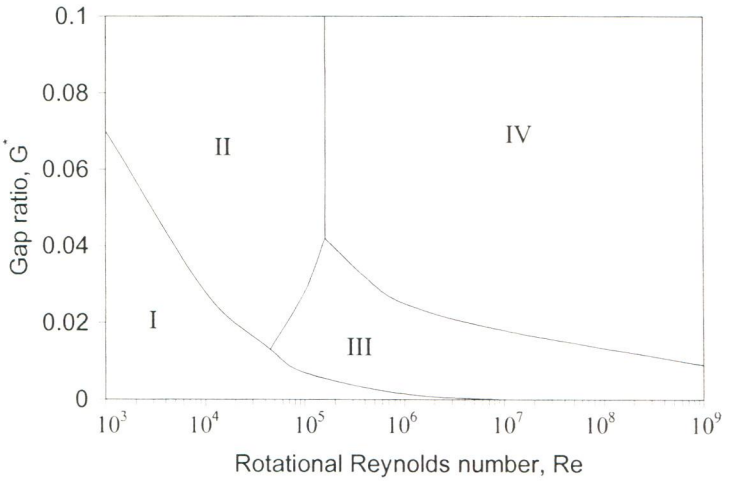

Figure E.5 The four regimes of flow in rotor stator systems (Owen, 1989).

Table E.1 The four flow regimes in rotor stator systems (Owen, 1989).

Regime	Clearance	Flow
I	Small	Laminar
II	Large	Laminar
III	Small	Turbulent
IV	Large	Turbulent

In the case of a rotating disc with a quadratic surface temperature profile $T(r) = T_\infty + cr^2$, parallel to a stationary isothermal full disc at T_∞, it has been shown that for regime I, Nu_{ave} is independent of Re ($Nu_{ave} = (G^*)^{-1}$), and that for regime III, Nu_{ave} depends on $\mathrm{Re}^{0.75}$ and is given by (Owen, 1989)

$$Nu_{ave} = 9.8 \cdot 10^{-3} \left(G^*\right)^{-1/4} \mathrm{Re}^{0.75} \qquad \text{(E.12)}$$

In the specific case of the AFPM machine, the gap ratio varies from 0.005 (between the rotor plates and the stator) to 0.014 (between the rotor plates and the shroud). The peripheral Reynolds number varies from a minimum of $1.8x10^5$ to a maximum of $2.1x10^6$ for rotational speeds of 200 and 2300rpm respectively. This places the AFPM machine well within the boundaries of regime III of figure E.5.

The determination of the local convective heat transfer coefficient involves solving the Navier Stokes equations that must be extended to include heat transfer. Therefore considering the scope of the current research project, two case studies will be presented in the following sections.

E.5 Case study A

The following section looks at the experimental work done by Harmand *et al* (1999) on the local convective heat transfer coefficient from the surface of a rotor facing a stator.

Introduction

The local convective heat transfer from a rotor with a 310 mm outer radius was studied experimentally at a distance of 3 mm from a coaxial crown-shaped stator with a 176 mm inner radius and a 284 mm outer radius. The experimental technique was based on the use of a thermally thick rotor heated from behind by infrared radiation. The local heat flux distribution from the rotor surface was identified by resolving the Laplace equation by finite-difference method using the experimental temperature distribution as boundary conditions. The tests were carried out with a single rotor and the rotor-stator system for peripheral Reynolds numbers ranging from $5.86x10^4$ to $1.47x10^6$ and thus sweeping across the laminar, transition and turbulent flow regimes. The gap ratio was kept at a constant value of $G^* = 0.01$.

Experimental set-up

A thick aluminium disc and a polyethersulfone (PES) layer with a thickness e=2 mm in the study zone ($R_1 > r < R_2$) constitute the rotor. The geometrical parameters of the test bench, figure E.6, are: R_1 = 170 mm, R_2 = 290 mm, R_{1s} = 176 mm, R_{2s} = 284 mm, R_{ext} = 310 mm and s = 3 mm.

The PES part of thermal conductivity k = 0.36 $Wm^{-1}K^{-1}$ facing the stator, is stuck on the aluminium disc, the rear face of which is subjected to infrared radiation. As the values of the PES thermal conductivity and PES thickness are low, the variations in the heat transfer coefficients on the PES surface are translated into temperature variations on this surface. The high values of the aluminium thermal conductivity and the disc thickness allow the temperature at the aluminium/PES interface to be homogenized. The rotor's rotational speed varies from 100 to 2400 rev/min. The steel stator is equipped with a fluorspar window so that the temperature on the rotor can be identified by infrared thermography.

The temperatures at the PES/aluminium interface are measured by two thermocouples bound to the acquisition system with a mercury ring collector. The stator temperature is measured by two K type thermocouples located at two different radii on its surface parallel to the rotor. For all the tests the stator temperature is quasi-uniform and the stator is considered isothermal. The temperature difference between the stator and the air is about 15 K.

Results of the tests on the convective heat transfer

The representation of the temperature difference $(T - T_\infty)$ as a function of dimensionless radius $r^* = (r - R_1)/(R_2 - R_1)$, shown in figure E.7, shows that there is a weak temperature variation in the study zone and a big drop in temperature at dimensionless radius $r^* = 0$ corresponding to the beginning of the study zone. The temperature difference between 15 and 30 K for all the tests is due to the increase in the PES thickness in this zone. In a simplified way the temperature profile on the disc surface can be represented by the following law: for $r < R_1$, $T = T_1$ and for $r \geq R_1$, $T = T_2$.

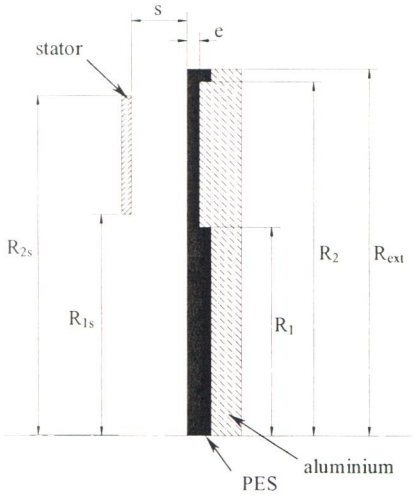

Figure E.6 Diagram of the rotor-stator system.

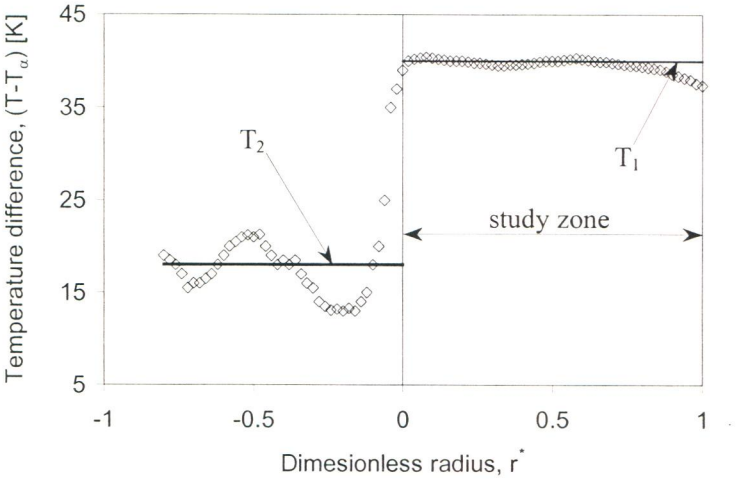

Figure E.7 Temperature profile on the surface of the rotor.

Local Nusselt number

In figures E.8 and E.9 the local Nusselt numbers are plotted as a function of the dimensionless radius r^* for different peripheral Reynolds numbers Re. The results relative to the single disc without the stator are also plotted.

Figure E.8 represents the results for $\mathrm{Re} = 1.17 \cdot 10^5$ for which the flow is laminar on the single disc. In the case of the free disc, the Nusselt number is in good correlation with equations (E.8) with, however, a slight increase next to the temperature step. In the case of the rotor facing the

stator, the Nusselt number is practically constant, which corresponds to a non-uniform convective exchange on the rotor: it is higher at the inner radius of the rotor study zone than at the outer radius. The experimental results for $Re = 1.47 \cdot 10^6$ are plotted in figure E.9. In the case of the free disc, this Reynolds number corresponds to completely turbulent flow. The experimental results correlate well with equation E.9 except near the temperature step where a slight increase in the Nusselt number is observed for the experimental configuration.

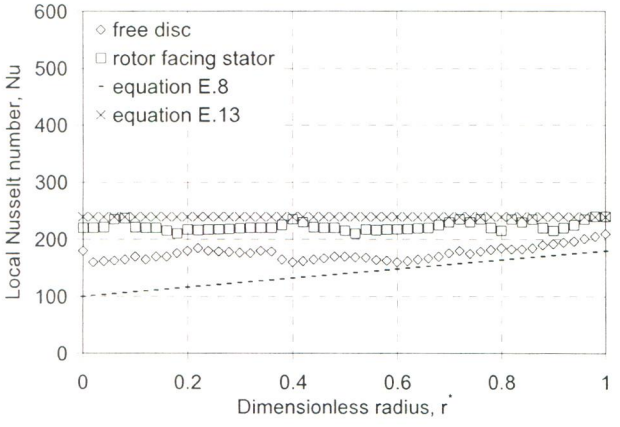

Figure E.8 Local Nusselt number as a function of dimensionless radius for $Re=1.17x10^5$

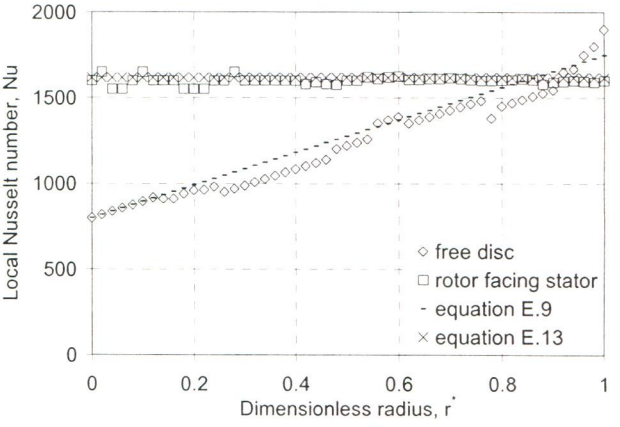

Figure E.9 Local Nusselt number as a function of dimensionless radius for $Re=1.47x10^6$

According to these tests, the distribution of the local Nusselt number as a function of the radius in the rotor-stator system, differs significantly from that obtained on the single disc. For the rotor-stator system, the local Nusselt number remains almost independent from the radius. The comparison of the experimental results for the local convective exchanges from the rotor facing the stator in the study zone and the free disc give rise to the following conclusions: the local convective heat transfer decreases as a function of increasing radius on the rotor when facing a stator which features a large central opening, contrary to the free disc. The fresh air supply is through the stator opening. The fluid in the air gap heats in the flow direction. There is no fresh fluid supply to the rotor facing the stator, contrary to the single disc, and the fluid temperature approaches that of the disc, thereby causing the decrease in the convective heat transfer from the disc towards the periphery.

The AFPM machine exhibits many similarities to the tests conducted above. The geometrical configurations as well as the thermal boundary conditions are very similar. The radii of the study zone as well as the magnitude of the gap is in the same order. The opening of the stator is large in the above tests as is that found in the AFPM machine. In both cases the stator is heated and

has similar temperature distributions. Using the above results the following correlation for the local Nusselt number on the surface of the rotor is established

$$Nu = 9.83 \cdot 10^{-3} (G^*)^{-0.28} \cdot \mathrm{Re}^{0.755} \qquad \text{(E.13)}$$

The results of this equation are also plotted in figures E.8 and E.9.

E.6 Case study B

The following section looks at the experimental work done by Djaoui *et al* (2001) on the local convective heat transfer coefficient from the surface of a rotor facing a stator.

Introduction

The convective heat transfer process occurring in an open rotor stator system subjected to superposed radial inflow was experimentally studied. The flow was characterised by a small gap ratio with turbulent flow (Regime III).

Experimental setup

The experimental apparatus consists of two coaxial horizontal discs 750 mm in diameter separated by an adjustable axial gap as shown in figure E.10. The lower disc is driven by an electric motor which allows the rotational speed to be varied up to 2000 rpm. The rotor and the hub were not insulated and no thermal boundary conditions were prescribed for these surfaces. The upper stationary disc was heated by heating tapes with a total power of 5.6 kW, located on the outside face of the disc. The tapes are set along circles concentric to the discs. The device allows an overheating of up to 40 degrees with respect to the surrounding atmosphere, the temperature of which is kept close to 297 K. The temperature distribution on the inside face of the disc is adjusted by means of copper-constantan thermocouples connected to electronic temperature controllers. The disc temperature was only measured at the eight locations indicated in figure E.10, which correspond to the following values of r: 0.43, 0.48, 0.53, 0.61, 0.69, 0.77, 0.83, 0.88. Eight pellicular fluxmeters are installed at the above-mentioned radial positions. The overall accuracy of the thermocouples and fluxmeters is estimated to be within ±5%.

Experimental results

For the results presented below, G^* was taken equal to 0.08 and the rotational speed was 1500 rpm, so that Re was fixed to $1.44 \cdot 10^6$, which corresponds to turbulent flow. The ambient temperature was maintained at 297 K and the stator temperature distribution as constant as

possible up to $r = 0.88$, with a mean value of 332 K. In figure E.11 the effect of inflow on the Nusselt number is shown.

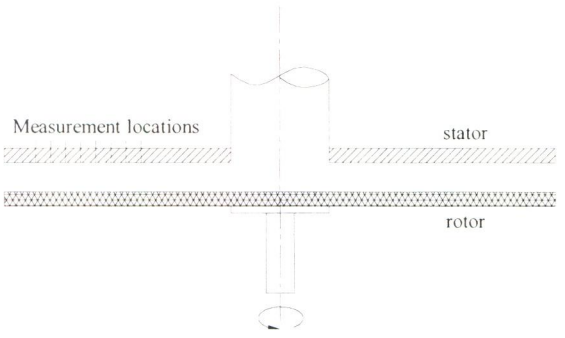

Figure E.10 Schematic diagram of the experimental setup

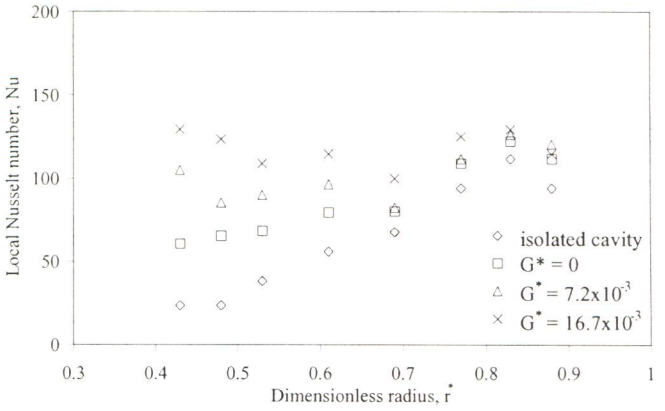

Figure E.11 Radial variation of the local Nusselt number on the stator

Using the experimental results obtained in this case study, a relationship for the local Nusselt number versus the dimensionless radius and flow rate was established. Nine data points from figure E.11 were used to establish the following polynomial

$$Nu(r,G^*) = a + br^* + c(r^*)^2 + dG^* + e(G^*)^2 + fr^*(G^*) + gr^*(G^*)^2 + h(r^*)^2 G + i(r^*)^2(G^*)^2 \quad \text{(E.14)}$$

Where the values of the constants are given in table E.2

Table E.2 Values of constant in equation E.14

a	74.487
b	-129.473
c	225.454
d	31153.947
e	-1834456.335
f	-87528.492
g	5830750.488
h	61198.939
i	-4380778.747

Equation E.14 is only valid for the range of flow rates used in the experiments, from 0 m^3 to $16.7x10^{-3}$ m^3. For flow rates outside this region equation E.14 is not applicable. For flow rates higher than $16.7x10^{-3}$ m^3 the Nusselt number is taken to equal a constant value of 140. This assumption is based on the data of figure E.11 and it is evident that as the flow rate increases the local Nusselt number increases. For higher flow rates it seems that the Nusselt number becomes less dependant on the radius. Once a limiting value of flow rate is achieved it is possible that the Nusselt number does not increase.

E.7 Conclusions and summary

This section presented research done on the rotor-stator systems. Correlations for the simple case of a free disc were presented. Rotor-stator systems with superposed flow were defined as well as the four different flow regimes associated with these systems. Of these systems the open rotor stator system is found in the AFPM machine and this system was explained in more detail. Considering the complexity of solving the Navier-Stokes equations for these systems and the scope of this thesis, two case studies were presented. In these case studies, experimental work was done on rotor-stator systems that were geometrically similar to those found in the AFPM machine. The experimental data from these case studies was used to establish a correlation for the convective heat transfer coefficient of the surface of the rotor and the stator. These correlations were used in the thermal model.

AFPM model drawings

The following pages contain the drawings produced for the manufacture of the Perspex model of the AFPM machine. Table F.1 shows the drawing tree for the AFPM model. The detailed drawings for the bearing housing were not produced as this component was manufactured in a previous research project.

Table F.1 Drawing tree of the AFPM model

Drawing name	Drawing number
General assembly	AFPM01
Shroud	
Open shroud	AFPMH01
Closed shroud	AFPMH02
Bracket	AFPMB01
Bellmouth	AFPMB02
Stator	AFPMT01
Rotor plates	
Left rotor plate	AFPMR02
Right rotor plate	AFPMR02
2.5 mm magnets	AFPMM01
5 mm magnets	AFPMM02
7.5 mm magnets	AFPMM03
Rotor hub	AFPMR01
1 mm spacer	AFPMSP01
2 mm spacer	AFPMSP02
3 mm spacer	AFPMSP03
Shaft	AFPMS01
Bearing housing	
Bearing bracket	
Bearings	
Bearing sleeve	
Bearing cover	
Bearing spacer	

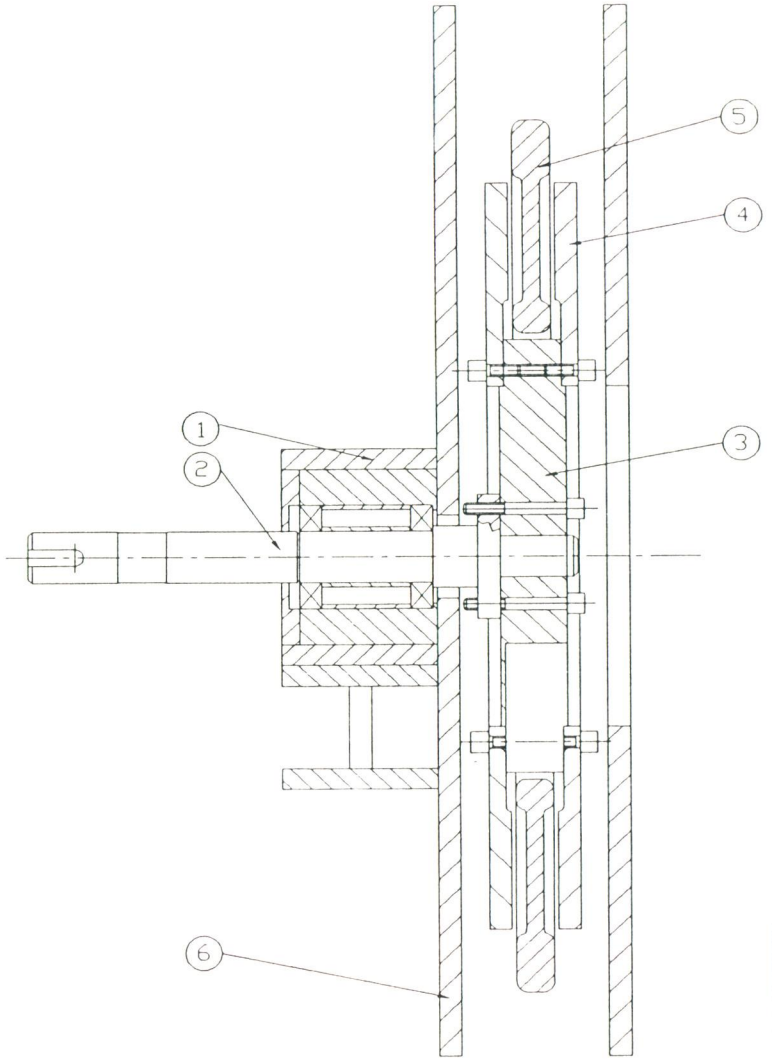

ITEM	DESCRIPTION	No.	MATERIAL	SPECS	DRAWING No.
6	SHROUD	2	PERSPEX		AFPMH1, AFPMH2
5	STATOR	1	PERSPEX		AFPMT01
4	ROTOR PLATE	2	PERSPEX		AFPMR02
3	ROTOR HUB	1	PERSPEX		AFPMR01
2	SHAFT	1	MILD STEEL		AFPMS01
1	BEARING HOUSING	1	PERSPEX		

UNIVERSITY OF STELLENBOSCH

STUDENT No. 12751189	DRAUGHTSMAN S.SCOWBY	CHECKED

SCALE 1:1	TITLE	GENERAL ASSEMBLY
MEASUREMENTS mm		
DATE	PAGE No. 1 OF 1 PAGES	No. AFPM01

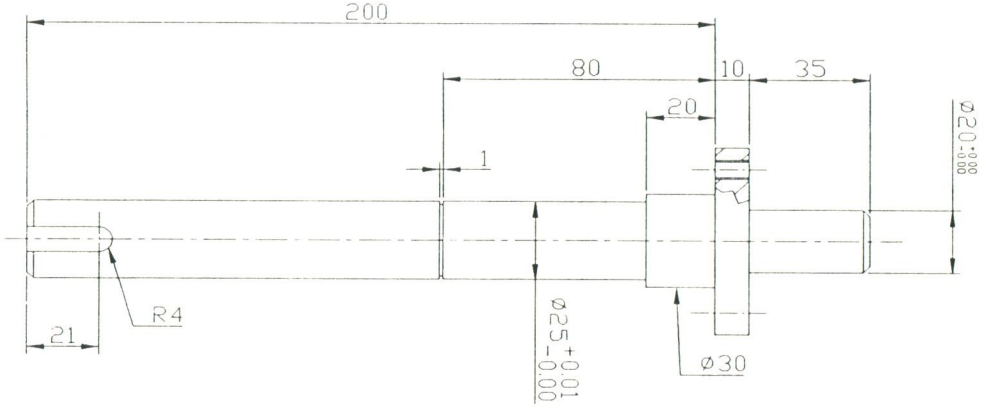

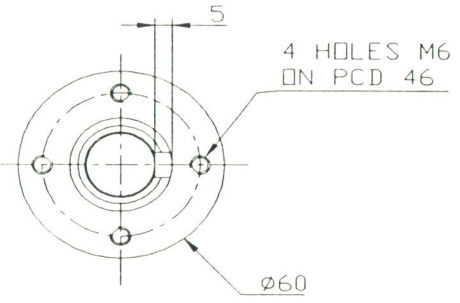

ITEM	DESCRIPTION	No.	MATERIAL	SPECS	DRAWING No.
1	SHAFT	1	MILD STEEL	ø110x282	

UNIVERSITY OF STELLENBOSCH	SCALE 1:1	TITLE SHAFT	
	MEASUREMENTS mm		
STUDENT No. 12751189 / DRAUGHTSMAN S.SCOWBY / CHECKED	DATE 20/02/02	PAGE No. 1 OF 1 PAGES	No. AFPMS01

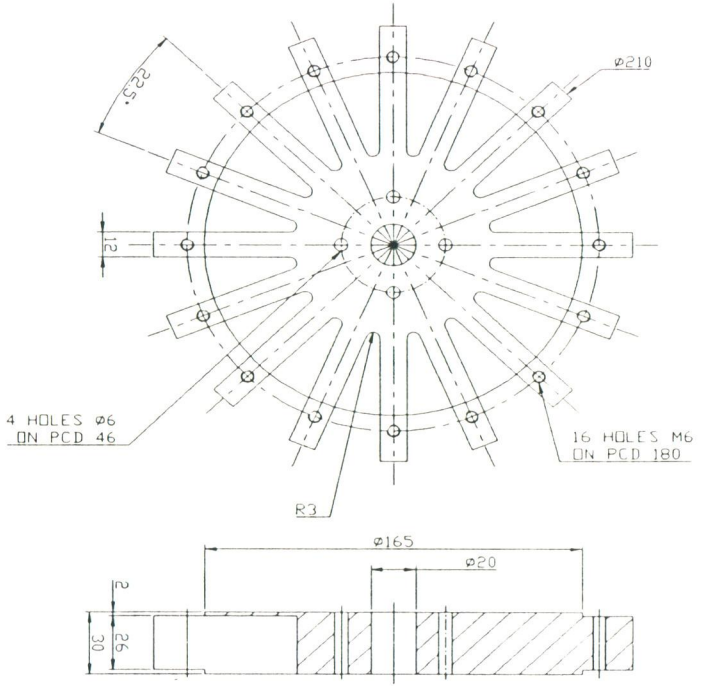

1	ROTOR	1	PERSPEX	ø210x30	
ITEM	DESCRIPTION	No.	MATERIAL	SPECS	DRAWING No.

UNIVERSITY OF STELLENBOSCH			SCALE 1:1	TITLE ROTOR HUB	
			MEASUREMENTS mm		
STUDENT No. 12751189	DRAUGHTSMAN S.SCOWBY	CHECKED	DATE	PAGE No. 1 OF 1 PAGES	No. AFPMR01

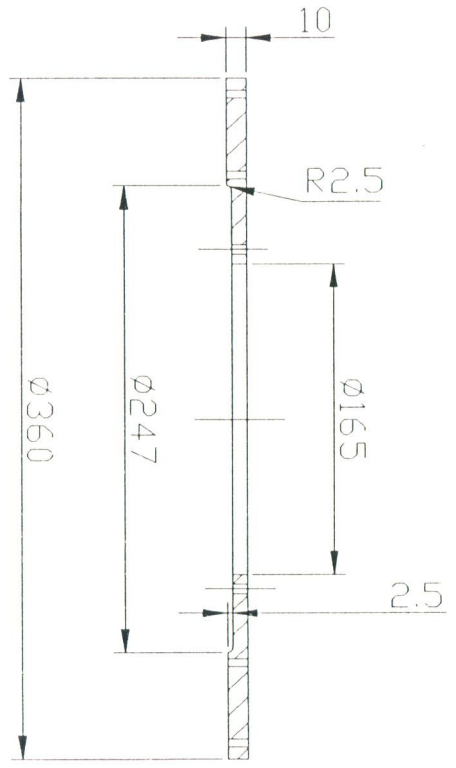

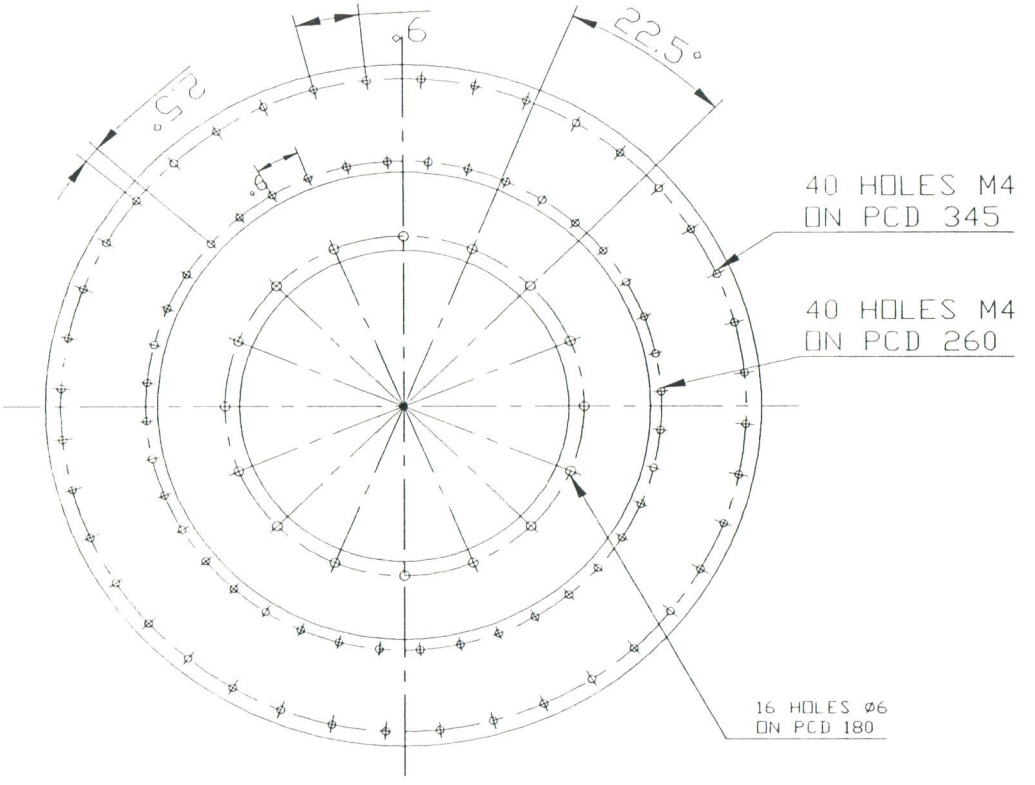

ITEM	DESCRIPTION	No.	MATERIAL	SPECS	DRAWING No.
1	ROTOR PLATE	2	PERSPEX	ø724x20	

UNIVERSITY OF STELLENBOSCH

STUDENT No. 12751189	DRAUGHTSMAN S.SCOWBY	CHECKED	SCALE 1:1 MEASUREMENTS mm DATE 20/02/02	TITLE ROTOR PLATE PAGE No. 1 OF 1 PAGES No. AFPMR02

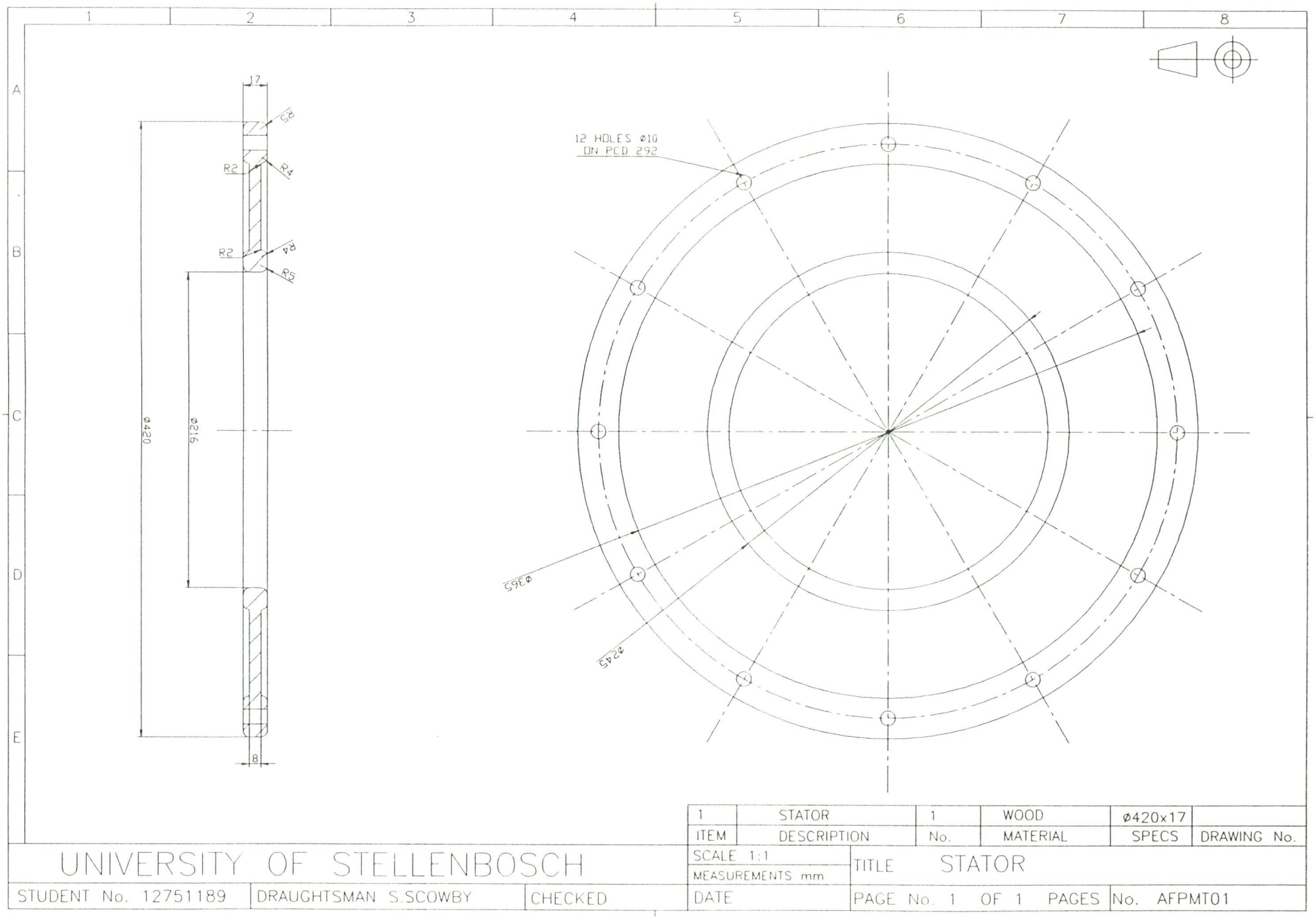

1	STATOR	1	WOOD	ø420x17	
ITEM	DESCRIPTION	No.	MATERIAL	SPECS	DRAWING No.

UNIVERSITY OF STELLENBOSCH	SCALE 1:1 MEASUREMENTS mm	TITLE STATOR
STUDENT No. 12751189 | DRAUGHTSMAN S.SCOWBY | CHECKED	DATE	PAGE No. 1 OF 1 PAGES | No. AFPMT01

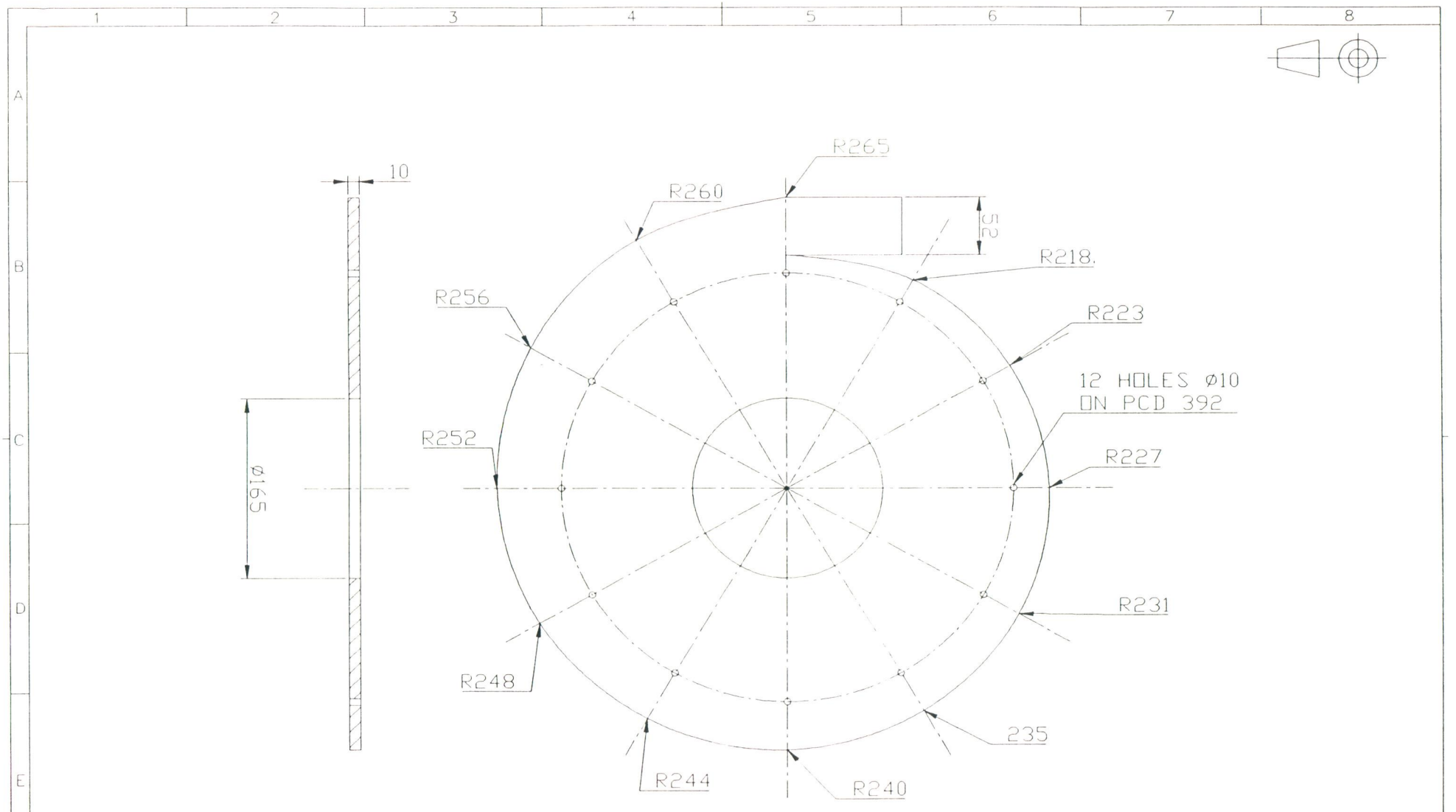

1	OPEN SHROUD	1	PERSPEX	ø530x10	
ITEM	DESCRIPTION	No.	MATERIAL	SPECS	DRAWING No.

UNIVERSITY OF STELLENBOSCH			SCALE 1:1	TITLE OPEN SHROUD		
			MEASUREMENTS mm			
STUDENT No. 12751189	DRAUGHTSMAN S.SCOWBY	CHECKED	DATE	PAGE No. 1 OF 1 PAGES	No.	AFPMH01

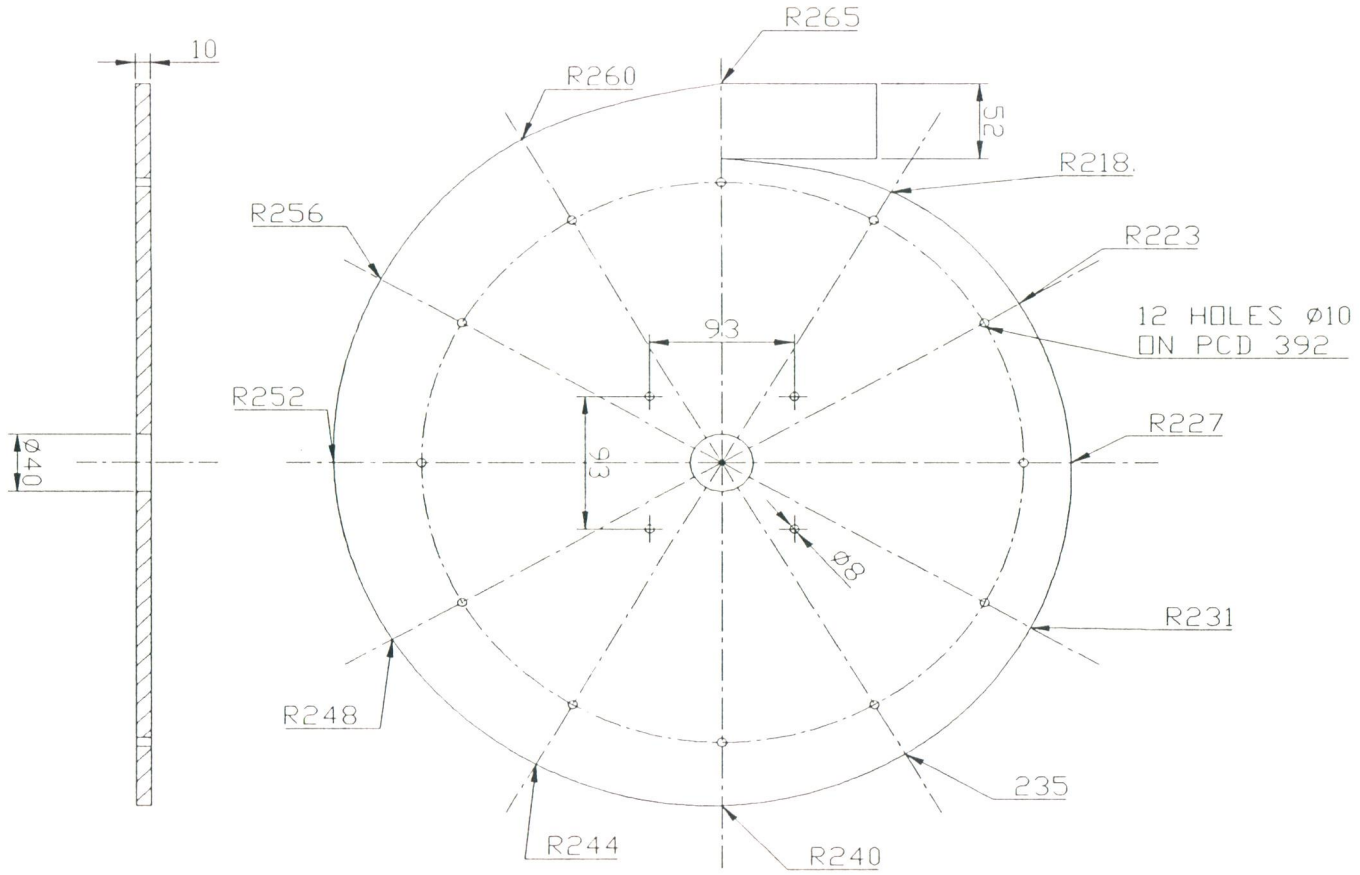

1	CLOSED SHROUD	1	PERSPEX	ø530x10	
ITEM	DESCRIPTION	No.	MATERIAL	SPECS	DRAWING No.

UNIVERSITY OF STELLENBOSCH			SCALE 1:1 MEASUREMENTS mm	TITLE CLOSED SHROUD	
STUDENT No. 12751189	DRAUGHTSMAN S.SCOWBY	CHECKED	DATE	PAGE No. 1 OF 1 PAGES	No. AFPMH02

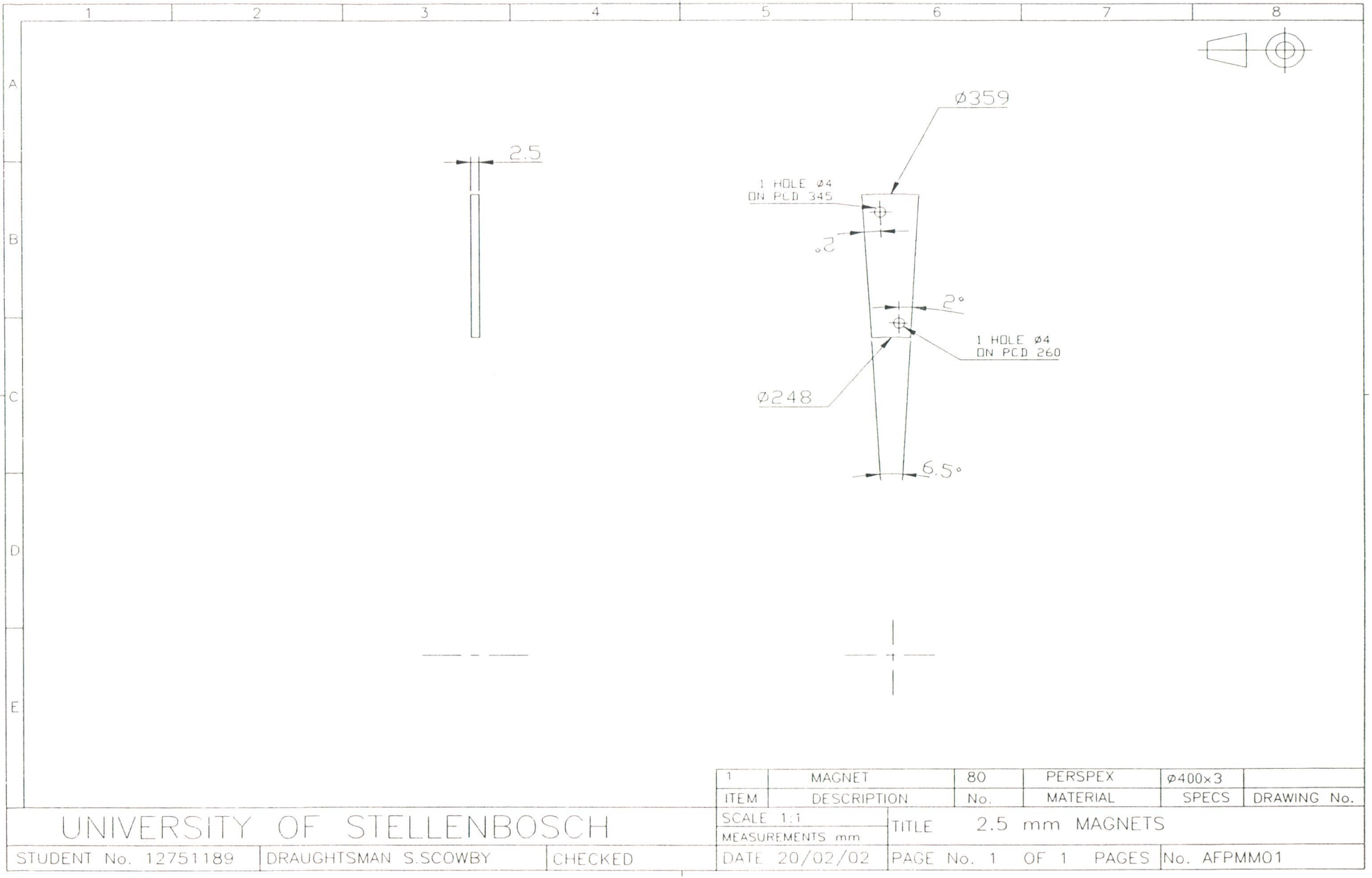

1	MAGNET	80	PERSPEX	Ø400x3	
ITEM	DESCRIPTION	No.	MATERIAL	SPECS	DRAWING No.

UNIVERSITY OF STELLENBOSCH			SCALE 1:1 MEASUREMENTS mm	TITLE 2.5 mm MAGNETS	
STUDENT No. 12751189	DRAUGHTSMAN S.SCOWBY	CHECKED	DATE 20/02/02	PAGE No. 1 OF 1 PAGES	No. AFPMM01

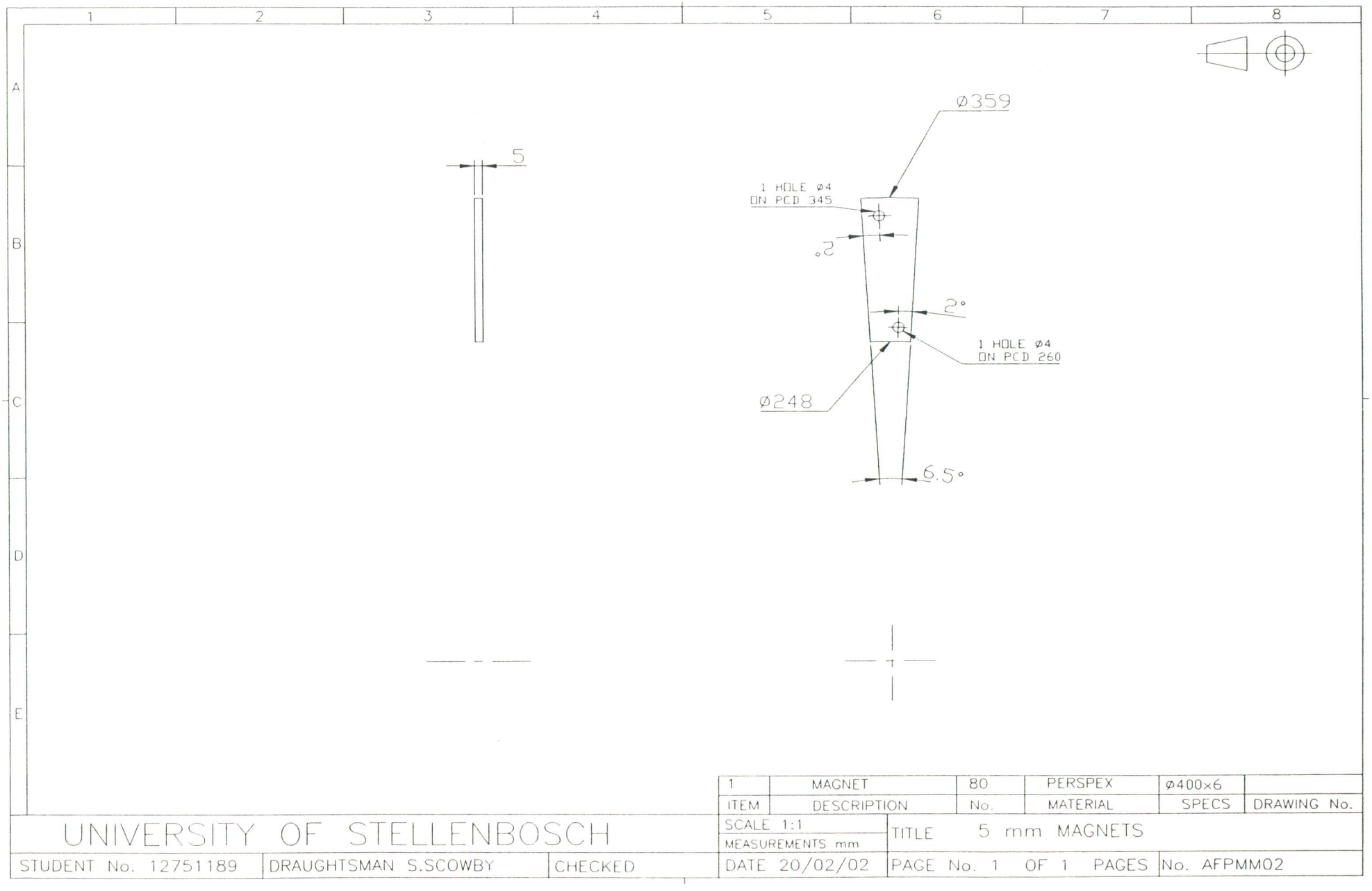

1	MAGNET	80	PERSPEX	Ø400×6	
ITEM	DESCRIPTION	No.	MATERIAL	SPECS	DRAWING No.

UNIVERSITY OF STELLENBOSCH			SCALE 1:1	TITLE 5 mm MAGNETS	
			MEASUREMENTS mm		
STUDENT No. 12751189	DRAUGHTSMAN S.SCOWBY	CHECKED	DATE 20/02/02	PAGE No. 1 OF 1 PAGES	No. AFPMM02

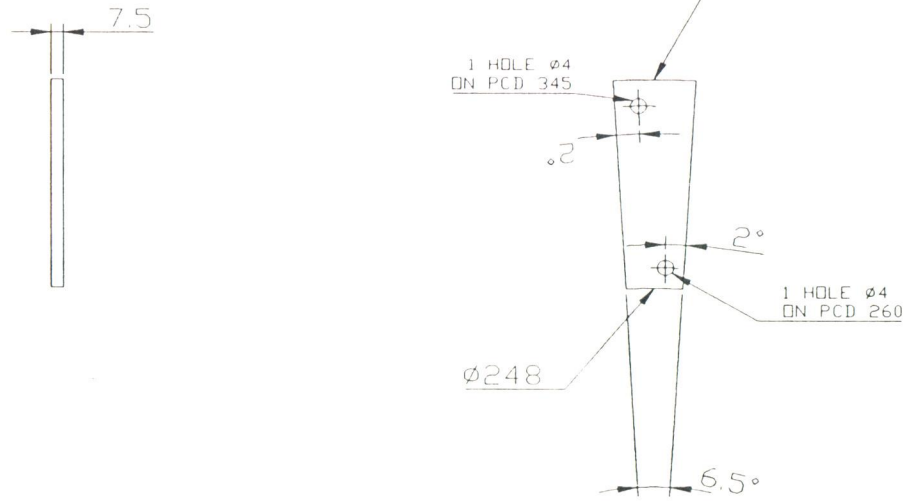

1	MAGNET	80	PERSPEX	ø400×8	
ITEM	DESCRIPTION	No.	MATERIAL	SPECS	DRAWING No.

UNIVERSITY OF STELLENBOSCH	SCALE 1:1 MEASUREMENTS mm	TITLE 7.4 mm MAGNETS	
STUDENT No. 12751189 | DRAUGHTSMAN S.SCOWBY | CHECKED	DATE 20/02/02	PAGE No. 1 OF 1 PAGES	No. AFPMM03

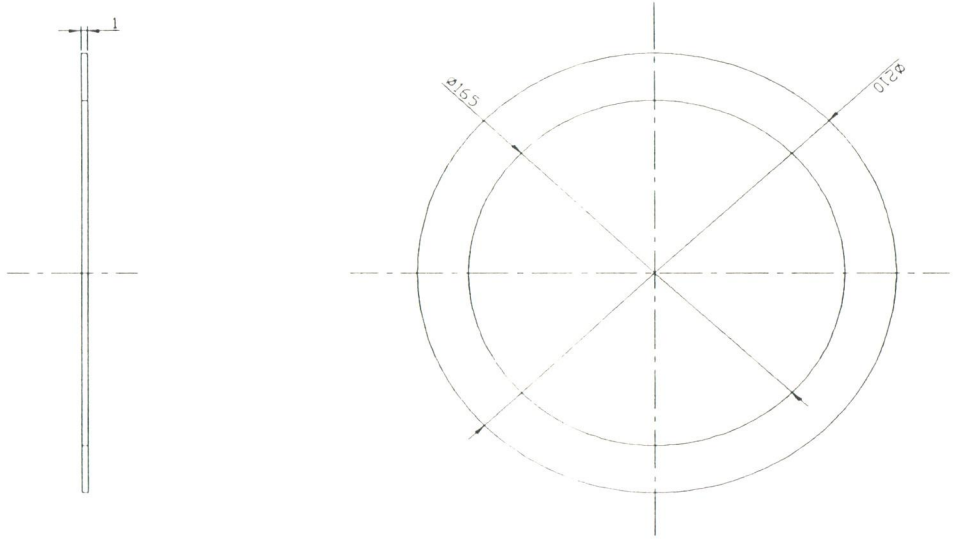

1	1 mm SPACER	2	PERSPEX	ø210x1	
ITEM	DESCRIPTION	No.	MATERIAL	SPECS	DRAWING No.

UNIVERSITY OF STELLENBOSCH			SCALE 1:1 MEASUREMENTS mm	TITLE 1 mm SPACER	
STUDENT No. 12751189	DRAUGHTSMAN S.SCOWBY	CHECKED	DATE	PAGE No. 1 OF 1 PAGES	No. AFPMSP01

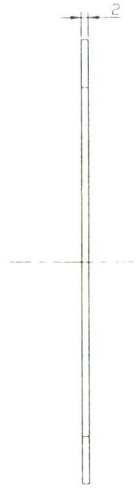

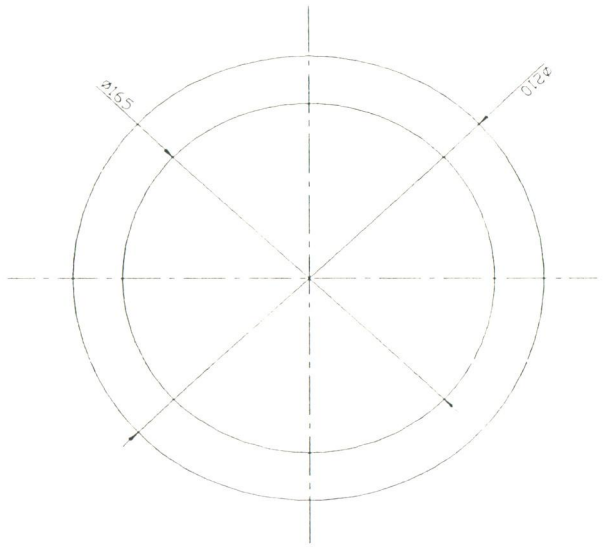

ITEM	DESCRIPTION	No.	MATERIAL	SPECS	DRAWING No.
1	2 mm SPACER	2	PERSPEX	ø210x2	

UNIVERSITY OF STELLENBOSCH	SCALE 1:1 MEASUREMENTS mm	TITLE 2 mm SPACER	
STUDENT No. 12751189 / DRAUGHTSMAN S.SCOWBY / CHECKED	DATE	PAGE No. 1 OF 1 PAGES	No. AFPMSP02

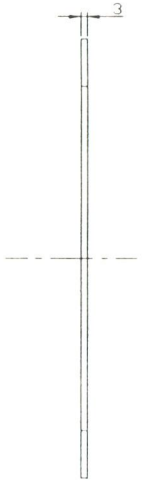

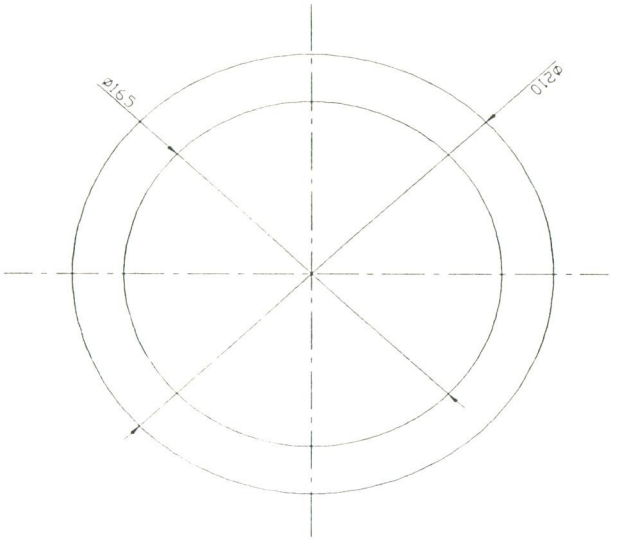

1	3 mm SPACER	1	PERSPEX	ø210x3	
ITEM	DESCRIPTION	No.	MATERIAL	SPECS	DRAWING No.

UNIVERSITY OF STELLENBOSCH			SCALE 1:1 MEASUREMENTS mm	TITLE 3 mm SPACER	
STUDENT No. 12751189	DRAUGHTSMAN S.SCOWBY	CHECKED	DATE	PAGE No. 1 OF 1 PAGES	No. AFPMSP03

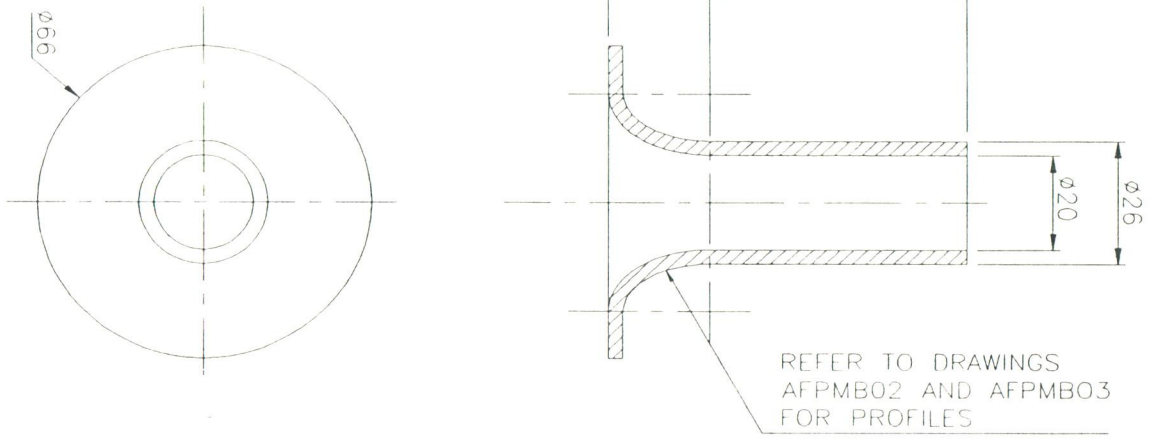

ITEM	DESCRIPTION	No.	MATERIAL	SPECS	DRAWING No.
1	BELLMOUTH	1	PVC	ø66x70	AFPMB01

UNIVERSITY OF STELLENBOSCH	SCALE 1:1 MEASUREMENTS mm	TITLE BELLMOUTH	
STUDENT No. 12751189 / DRAUGHTSMAN S.SCOWBY / CHECKED	DATE ITEM	PAGE No. 1 OF 2 PAGES	No. AFPMB01

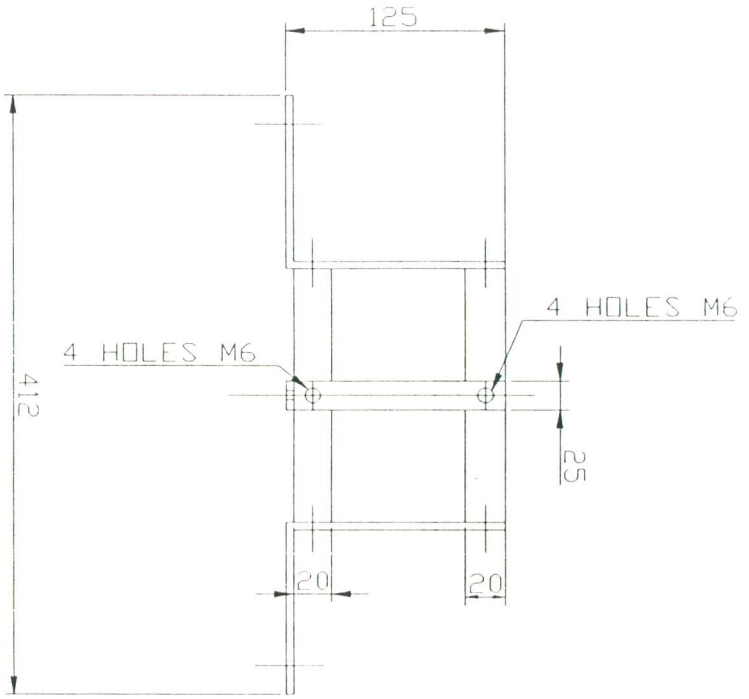

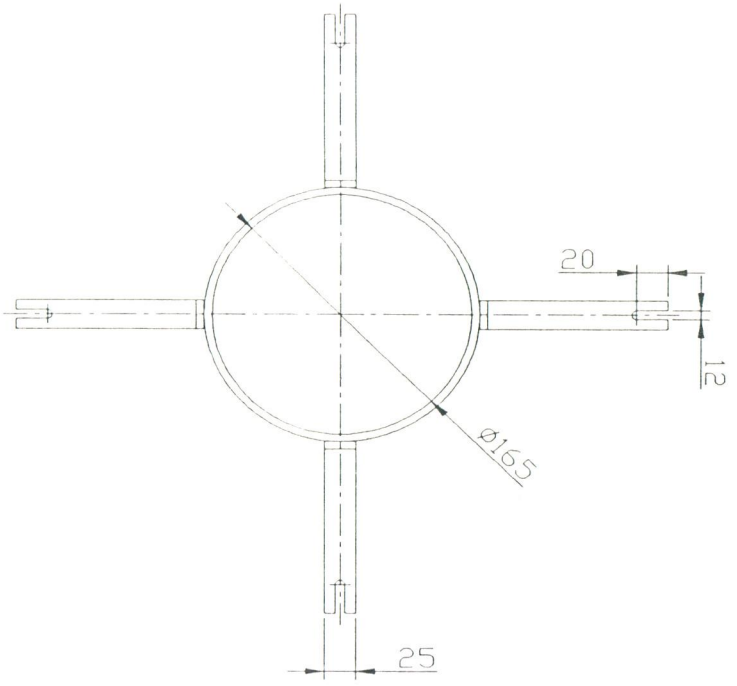

NOTE: TO BE MADE FROM
25x5 FLAT PLATE

ITEM	DESCRIPTION	No.	MATERIAL	SPECS	DRAWING No.
1	OPEN SHROUD	1	25x5 FLAT PLATE	ø530x10	

UNIVERSITY OF STELLENBOSCH	SCALE 1:1	TITLE BRACKET	
	MEASUREMENTS mm		
STUDENT No. 12751189 / DRAUGHTSMAN S.SCOWBY / CHECKED	DATE	PAGE No. 1 OF 1 PAGES	No. AFPMB01

Appendix G

Heat pipes

G.1 Introduction and objectives

The heat pipe is a very effective device for transmitting heat at high rates over considerable distances with extremely small temperature drops, exceptional flexibility, simple construction, and easy control with no external pumping power. Heat pipes and thermosyphons both operate on a closed two-phase cycle and utilize the latent heat of vaporization to transfer heat with very small temperature gradients. Thermosyphons rely solely on the gravitational forces to return the liquid phase of the working fluid from the condenser to the evaporator, while heat pipes utilize capillary pumping within the wick. Heat pipes can be used in any orientation, i.e. the condenser can be below the evaporator. This dependence on the gravitational field to return the working fluid from the condenser to the evaporator differentiates the thermosyphon from the heat pipe. The objective of this section is to develop a better understanding of heat pipes and how they can be applied in the thermo fluid modelling of the AFPM machine.

G.2 Principles of operation

A classical heat pipe consists of a sealed container lined with a wicking structure. The container is evacuated and backfilled with just enough liquid to fully saturate the wick. When a heat pipe operates on a closed two-phase cycle with only pure liquid and vapour present, the working fluid remains at saturation conditions as long as the operating temperature is between the freezing point and the critical state. The three distinct regions of a heat pipe, figure G.1, are: the evaporator or heat addition region, the condenser or heat rejection region, and the adiabatic or isothermal region. Heat added to the evaporator region of the container causes the working fluid in the evaporator wicking structure to be vaporized. The high temperature and corresponding high pressure in this region result in flow of the vapour to the other, cooler end of the container, where the vapour condenses, giving up its latent heat of vaporization. The capillary forces in the wicking structure then pump the liquid back to the evaporator. Similar devices, referred to as two-phase thermosyphons, have no wick but utilize gravitational forces for the liquid return.

In order to function properly, heat pipes require three major components: the case, which can be constructed from glass, ceramic, or metal; a wicking structure, which can be fabricated from

woven fibreglass, sintered metal powders, screens, wire meshes, or grooves; and a working fluid, which can vary from nitrogen or helium for low-temperature (cryogenic) heat pipes to lithium, potassium, or sodium for high-temperature (liquid metal) heat pipes. Each of these three components is equally important, with careful consideration given to the material type, thermophysical properties, and compatibility.

The heat pipe container or case provides containment and structural stability. It must be fabricated from a material that is compatible with both the working fluid and the wicking structure, strong enough to withstand the pressure associated with the saturation temperatures encountered during storage and normal operation, and of a high enough thermal conductivity to permit the effective transfer of heat either into or out of the vapour core. The container should also be resistant to corrosion resulting from interaction with the environment and must be malleable enough to be formed into the appropriate size and shape.

The wicking structure has two functions in heat pipe operation: it is the mechanism by which the working fluid is returned from the condenser to the evaporator. It also ensures that the working fluid is evenly distributed over the evaporator surface in order to provide a flow path with low flow resistance through which the liquid can be returned from the condenser to the evaporator. An open porous structure with a high permeability is desirable. However, to increase the capillary pumping pressure, a small pore size is necessary. The menisci at the liquid-vapour interface are highly curved in the evaporator section due to the fact that the liquid recedes into the pores of the wick, figure G.2. On the other hand, during the condensation process the menisci in the condenser section are nearly flat.

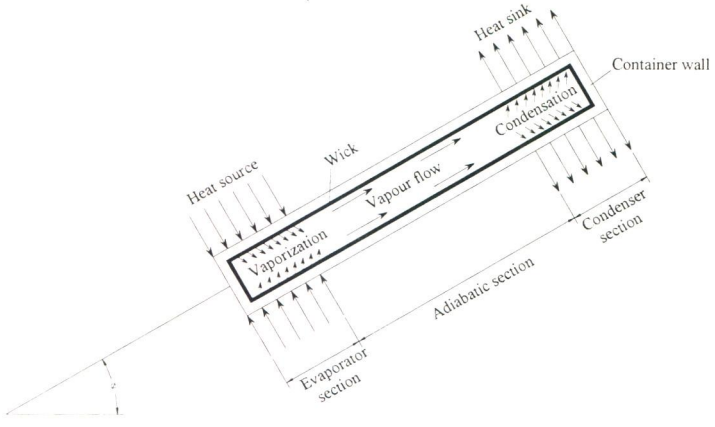

Figure G.1 Heat pipe operation

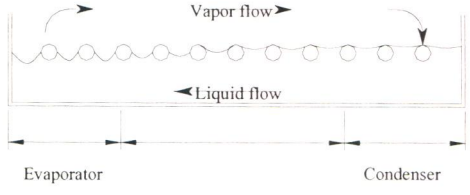

Figure G.2 Variation of meniscus curvature as a function of axial position (Rohsenhow, 1998).

G.3 Working fluids and their temperature ranges

Each heat pipe application has a particular temperature range in which the heat pipe needs to operate. Therefore, the design of the heat pipe must take into consideration the intended temperature range by specifying the proper working fluid. Table G.1 lists some of the commonly used and proposed working fluids, their melting and boiling points at atmospheric pressure, and their useful ranges.

As a rule of thumb, the useful range extends from the point where the saturation pressure is greater than 0.1 atm and less than 20 atm. Below 0.1 atm, the vapour pressure limit may be approached. Above 20 atm, the container thickness must increase to the point where the heat pipe becomes limited by the thermal resistance through the container. Longevity of a heat pipe can be assured by selecting a container, wick and welding materials that are compatible with each other and with the working fluid of interest. Performance can be degraded and failures can occur in the container wall if any of the parts (including the working fluid) are not compatible. The different parts of the heat pipe can react chemically or set up a galvanic cell within the heat pipe. Also, the container material may be soluble in the working fluid or may catalyse the decomposition of the working at the expected operational temperature. A compilation of the compatibility of metals with working fluids is given in table G.2.

Another means of evaluating a working fluid's potential is the **figure of merit,** μ, of the working fluid, usually expressed in kW/cm^2 (Dunn and Reay, 1982):

$$\mu = \frac{\rho_l \sigma h_{fg}}{\mu_l} \qquad [\text{kW/cm}^2] \qquad \text{(G.1)}$$

The figure of merit is a function of temperature and is shown in figure G.3 for a selection of heat pipe fluids. The clear superiority of water in the intermediate temperature range is due to its high latent heat and surface tension.

Table G.1 Working fluids and their temperature ranges (Dunn and Raey, 1982).

Working Fluid	Melting Point, K at 1 atm	Boiling Point, K at 1 atm	Useful Range, K
Helium	1.0	4.21	2-4
Hydrogen	13.8	20.38	14-31
Neon	24.4	27.09	27-37
Nitrogen	63.1	77.35	70-103
Argon	83.9	87.29	84-116
Oxygen	54.7	90.18	73-119
Methane	90.6	111.4	91-150
Krypton	115.8	119.7	116-160
Ethane	89.9	184.6	150-240
Freon 22	113.1	232.2	193-297
Ammonia	195.5	239.9	213-373
Freon 21	138.1	282.0	233-360
Freon 11	162.1	296.8	233-393
Pentane	143.1	309.2	253-393
Freon 113	236.5	320.8	263-373
Acetone	180.0	329.4	273-393
Methanol	175.1	337.8	283-403
Flutec PP2	223.1	349.1	283-433
Ethanol	158.7	351.5	273-403
Heptane	182.5	371.5	273-423
Water	273.1	373.1	303-473
Toluene	178.1	383.7	323-473
Flutec PP9	203.1	433.1	273-498
Naphthalene	353.4	490	408-478
Dowtherm	285.1	527.0	423-668
Mercury	234.2	630.1	523-923
Sulphur	385.9	717.8	530-947
Cesium	301.6	943.0	723-1173
Rubidium	312.7	959.2	800-1275
Potassium	336.4	1032	773-1273
Sodium	371.0	1151	873-1473
Lithium	453.7	1615	1273-2073
Calcium	1112	1762	1400-2100
Lead	600.6	2013	1670-2200
Indium	429.7	2353	2000-3000
Silver	1234	2485	2073-2573

Table G.2 Generalized results of experimental compatibility tests (Dunn and Raey, 1982).

Working Fluid	Compatible Material	Incompatible Material
Water	Stainless steel, copper, silica, nickel, titanium	Aluminium, inconel
Ammonia	Aluminium, stainless steel, cold rolled steel, iron, nickel	Copper
Methanol	stainless steel, iron, copper, brass, silica, nickel	Aluminium
Acetone	Aluminium, stainless steel, copper, brass, silica	
Freon-11	Aluminium	
Freon-21	Aluminium,iron	
Freon-113	Aluminium	
Heptane	Aluminium	
Dowtherm	Stainless steel, copper, silica	
Lithium	Tungsten, tantalum, molybdenum, niobium	Stainless steel, nickel, titanium, inconel
Sodium	Stainless steel, nickel, inconel, niobium	Titanium
Cesium	Titanium, niobium	
Mercury	Stainless steel	Molybdenum, nickel, tantalum, inconel, titanium, niobium
Lead	Tungsten, tantalum	Stainless steel, nickel, inconel, titanium, niobium
Silver	Tungsten, tantalum	Rhenium

G.4 Capillary wick designs and structures.

The wick structure within the heat pipe is present to return condensate to the evaporator section. While small pores are needed at the liquid-vapour interface to develop high capillary pressures, large pores are preferred within the wick so that the movement of the liquid is not restricted too greatly. For this reason, many different types of wick structures have been developed in order to optimise the performance of the capillary heat pipe. The types of wick structures can be divided into two categories: homogeneous and composite wicks. Homogeneous wicks have the benefit of being relatively simple to design, manufacture and install. Composite wicks, however, can significantly increase the capillary limit of the heat pipe, but have the drawback of high manufacturing costs. There are three properties of wicks that are important in heat pipe design:

1. Minimum capillary radius: This parameter should be small if a large capillary pressure difference is required, such as terrestrial operation for a long heat pipe with the

evaporator above the condenser or in cases where a high heat transport capability is needed.

2. Permeability: Permeability is a measure of the wick resistance to axial liquid flow. This parameter should be large in order to have a small liquid pressure drop and therefore higher heat transport capability.
3. Effective thermal conductivity: A large value for this parameter gives a small temperature drop across the wick, which is a favourable condition in heat pipe design.

A high thermal conductivity and permeability, and a low minimum capillary radius are somewhat contradictory properties in most wick designs. For example, a homogeneous wick may have a small minimum capillary radius and a large effective thermal conductivity, but have a small permeability. Therefore, the designer must always make trade-offs between these competing factors to obtain an optimal wick design.

G.5 Heat transfer limitations

Heat pipes undergo various heat transfer limitations depending on the working fluid, the wick structure, the dimensions of the heat pipe, and the heat pipe operational temperature. Figure G.4 gives a qualitative description of the various heat transfer limitations, which include vapour-pressure, sonic, entrainment, capillary, and boiling limitations. The composite curve in figure G.4 gives the maximum heat transfer rate of the heat pipe as a function of the operational temperature. The figure shows that as the operational temperature increases, the maximum heat transfer rate of the heat pipe is limited by different physical phenomena. As long as the operational heat transfer rate falls within the enclosed region, the heat pipe will function properly.

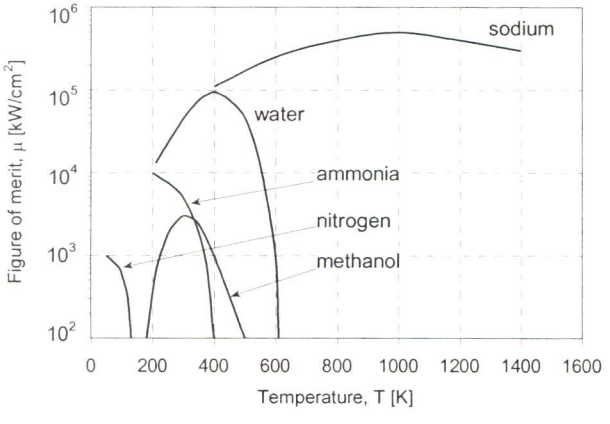

Figure G.3 Figure of merit for a number of heat pipe fluids.

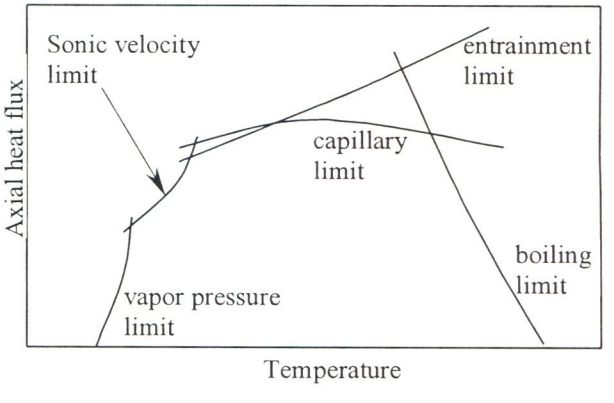

Figure G.4 Heat transfer limitations in heat pipes (Kreith, 1999).

The vapour-pressure limitation (or viscous limitation) in heat pipes develops when the pressure drop in the vapour core reaches the same order of magnitude as the vapour pressure in the evaporator. Under these conditions, the pressure drop due to flow through the vapour core creates an extremely low vapour pressure in the condenser preventing vapour from flowing in the condenser. A general expression for the vapour-pressure limitation is (Dunn and Reay, 1982)

$$\dot{Q}_{vp,\max} = \frac{\pi r_v^4 h_{fg} \rho_{v,l} p_{v,l}}{12 \mu_{v,l} l_{eff}} \tag{G.2}$$

where r_v is the cross-sectional radius of the vapour core, h_{fg} is the latent heat of vaporization, $\rho_{v,l}$ is the vapour density in the evaporator, $p_{v,l}$ is the vapour pressure in the evaporator, and $\mu_{v,l}$ is the vapour viscosity in the evaporator. l_{eff} is the effective length of the heat pipe equal to $l_{eff} = 0.5(l_e + 2l_a + l_c)$. The vapour-pressure limitation can occur during the start-up of heat pipes at the lower end of the working-fluid-temperature range.

The sonic limitation also can occur in heat pipes during start-up at low temperatures. The low temperature produces a low vapour density, thereby reducing the speed of sound in the vapour core. Thus, a sufficiently high mass flow rate in the vapour core can cause sonic flow conditions and generate a shock wave that chokes flow and restricts the pipes ability to transfer heat to the condenser. Dunn and Reay (1982) suggest an expression for the sonic limitation that correlates very well with experimental data,

$$\dot{Q}_{s,\max} = 0.474 A_v h_{fg} (\rho_v p_v)^{1/2} \tag{G.3}$$

where A_v is the cross-sectional area of the vapour core. The sonic limitation should be avoided because large temperature gradients occur in heat pipes under choked-flow conditions.

The entrainment limitation in heat pipes develops when the vapour mass flow rate is large enough to shear droplets of liquid off the wick surface causing dry-out in the evaporator. A conservative estimate of the maximum heat transfer rate due to entrainment of liquid droplets has been given by Dunn and Reay (1982) as

$$\dot{Q}_{e,\max} = A_v h_{fg} \left[\frac{\rho_v \sigma_l}{2 r_{c,ave}} \right]^{1/2} \tag{G.4}$$

where σ_l is the surface tension and $r_{c,ave}$ is the average capillary radius of the wick.

The capillary limitation in heat pipes occurs when the net capillary forces generated by the vapour-liquid interfaces in the evaporator and condenser are not large enough to overcome the frictional pressure losses due to fluid motion. This causes the heat pipe evaporator to dry out and shuts down the transfer of heat from the evaporator to the condenser. For most heat pipes, the maximum heat transfer rate due to the capillary limitation can be expressed as (Chi, 1976)

$$\dot{Q}_{c,\max} = \left[\frac{\rho_l \sigma_l h_{fg}}{\mu_l}\right]\left[\frac{A_w K}{l_{eff}}\right]\left[\frac{2}{r_{c,e}} - \left(\frac{\rho_l}{\sigma_l}\right) g L_t \cos\psi\right] \tag{G.5}$$

where K is the wick permeability, A_w is the wick cross-sectional area, ρ_l is the liquid density, μ_l is the liquid viscosity, $r_{c,e}$ is the wick capillary radius in the evaporator, g is the acceleration due to gravity, and L_t is the total length of the pipe. For most practical operating conditions, this limitation can be used to determine the maximum heat transfer rate in heat pipes.

The boiling limitation occurs when the degree of liquid superheat in the evaporator is large enough to cause the nucleation of vapour bubbles on the surface of the wick or the container. Boiling is usually undesirable in heat pipes because local hot spots can develop in the wick, obstructing the flow of liquid in the evaporator. An expression for the boiling limitation is (Chi, 1976)

$$\dot{Q}_{b,\max} = \frac{4\pi l_{eff} k_{eff} T_v \sigma_v}{h_{fg} \rho_l \ln(r_i / r_v)}\left(\frac{1}{r_n} - \frac{1}{r_{c,e}}\right) \tag{G.6}$$

where k_{eff} is the effective thermal conductivity of the composite wick and working fluid, T_v is the vapour saturation temperature, r_i is the inner container radius and r_n is the nucleation radius (equal to 2.00×10^{-6} m in the absence of noncondensable gas).

G.6 Pressure Balance in a Heat Pipe

The stable working fluid circulation in a heat pipe is achieved through the capillary pressure head developed by the wick structure. The maximum heat transfer attainable in a heat pipe is achieved under conditions such that the capillary pressure head is greater than or equal to the sum of pressure losses occurring in the vapour-liquid path. In order for the heat pipe to operate properly, the following pressure balance must be satisfied

$$\Delta p_{cap,\max} \geq \Delta p_l + \Delta p_v + \Delta p_g \tag{G.7}$$

where Δp_l is the pressure loss in overcoming the resistance to flow due to friction in moving the condensate through the wick, Δp_v is the pressure loss in overcoming the resistance to flow due to

friction in moving the vapour through the central core of the heat pipe and Δp_g is the pressure loss due to lifting the condensate from the condenser, against gravity. The maximum capillary head can be calculated by

$$\Delta p_{ca,\max} = \frac{2\sigma}{r_{eff}} \tag{G.8}$$

where r_{eff} is the effective pore radius. The pressure loss in overcoming the resistance to flow due to friction in moving the condensate through the wick from the condenser to the evaporator is

$$\Delta p_l = \frac{\mu_l L_{eff,wick} \dot{m}}{\mathrm{K}_{wick} \rho_l A_{wick}} \tag{G.9}$$

Δp_l depends on the mass flow rate $\dot{m}$, the fluid properties μ_l and ρ_l, the effective length of the wick $L_{eff,wick}$, the cross section area of the wick A_{wick} as well as the wick permeability K_{wick}. The pressure loss in overcoming the resistance to flow due to friction in moving the vapour through the central core of the heat pipe from the evaporator to the condenser is given by

$$\Delta p_v = 4C_{f,v} \frac{L_{eff} \dot{m}^2}{d_v \rho_v A_v^2} \tag{G.10}$$

This frictional pressure loss for the vapour depends on the coefficient of friction, $C_{f,v}$, between the working fluid and the surface over which it is flowing, the distance over which it must travel L_{eff}, the diameter of the central core through which the vapour is flowing, d_v=*2 x wick thickness*, and the cross-sectional area of the vapour flow A_v, the density of the vapour ρ_v, and the mass flow rate $\dot{m}$. An estimate of the coefficient of friction can be obtained from

$$C_{f,v} = \frac{16\mu_v A_v}{\dot{m} d_v} \tag{G.11}$$

The pressure loss due to lifting the condensate from the condenser, against gravity back to the evaporator, is given by

$$\Delta p_g = -\rho_l g L_{eff} \sin\theta \tag{G.12}$$

The gravitational pressure loss depends on the density of the liquid ρ_l, the gravitational constant due to gravity g and the vertical distance that the liquid must be lifted $L_{eff} \sin\theta$. The angle θ, describes the angle of inclination between the heat pipe and the horizontal. If the evaporator is above the condenser, then θ is taken as positive, *unfavourable tilt.* If the evaporator is below the condenser then θ is taken as negative, *favourable tilt.*

If equations G.8-12 are substituted into equation G.7 a rather complicated equation is obtained that must be solved for the mass flow rate. Thus an alternative option is to use a numerical solution. The idea is to plot the left hand side of equation G.7 against the right hand side. The intersection point of these lines gives the maximum possible mass flow rate. From this the maximum heat transfer rate can be determined by

$$Q_{\max} = \dot{m}_{\max} h_{fg} \tag{G.13}$$

One must keep in mind that this is the maximum heat transfer permissible as determined by the capillary pressure (heat transfer limitation due to capillary pressure). There are still other limiting factors as were mentioned earlier. Figure G.5 shows the point of maximum mass flow rate.

A lower heat load than that given by equation A.13 would mean that the amount of working fluid evaporated in the evaporator would be less, therefore the driving pressure in the vapour flow would also be less. Less vapour would condensate in the condenser and therefore less fluid would flow through the wick. In this case the mass flow rate is given by

$$\dot{m} = \frac{\dot{Q}_{applied}}{h_{fg}} \tag{G.14}$$

When the operating mass flow rate is less than the maximum mass flow rate, the heat pipe will be operating at a point similar to that shown in figure G.6. At this point the capillary pumping pressure is greater than the pressure losses throughout the system. Therefore any vapour that is condensed in the condenser will be pumped back to the evaporator. This excess pumping pressure given by the difference between the capillary pressure and the system pressure loss is known as the '*capillary pump advantage*' as shown in figure G.6.

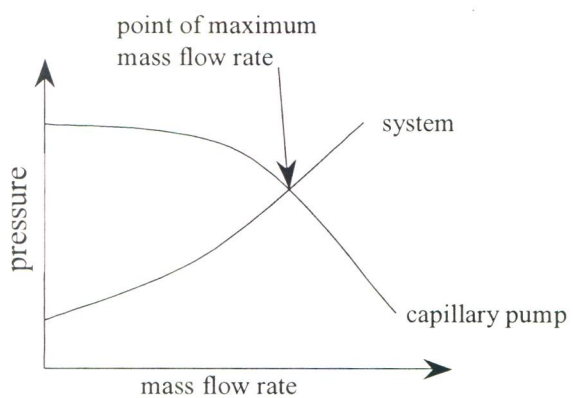

Figure G.5 The point of maximum mass flow rate

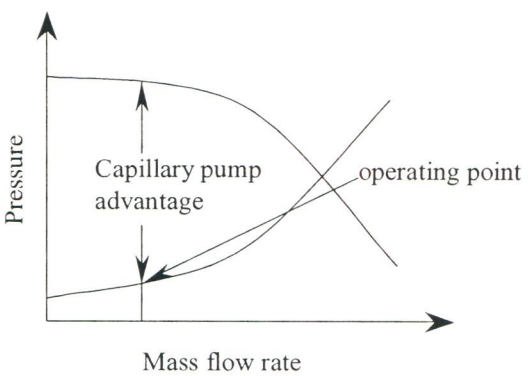

Figure G.6 Capillary pumping advantage.

G.7 Thermal Modelling of the Heat Pipe

In the design of a heat pipe it is important to have an efficient model of the heat pipe. This will aid in making decisions on certain variables such as the different lengths and diameters involved. For the implementation of the model it is necessary to have knowledge of certain thermal characteristics, i.e. different heat transfer coefficients. The three main thermal characteristics are:

1. The various heat transfer coefficients involved.
2. The optimum geometry for efficient heat transfer.
3. The maximum heat transfer that the heat pipe is capable of transferring for the selected geometry.

Generally the heat transfer coefficients are very complex functions and it is for this reason that experimental results are preferred. The amount of heat transferred by the heat pipe depends on two parameters, namely the temperature difference or the "thermal potential" between the hot and cold ends, and the "thermal resistance" to heat flow between the hot and cold ends. This process in which the heat is transferred can be represented by a thermal resistance circuit diagram as shown in figure G.7. This model can be simplified somewhat by making the following observations. The resistance to heat flow along the container wall (axial direction) is large relative to the vapour core axial resistance. If the resistance is high the heat flow will naturally be lower, therefore this heat transfer path can effectively be ignored. The same applies for the axial resistance of the wick and fluid. This simplified model can be represented schematically as shown in figure G.8.

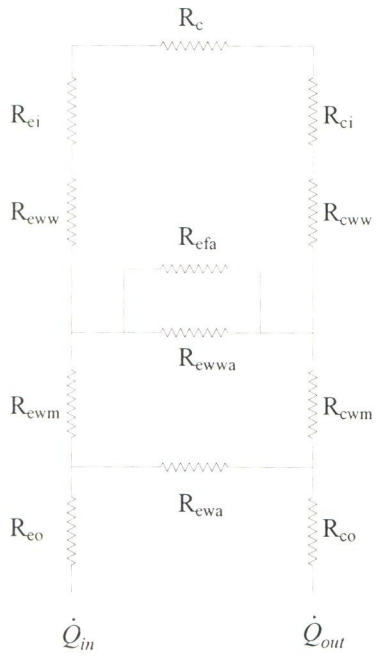

Figure G.7 Thermal resistance model for the heat pipe.

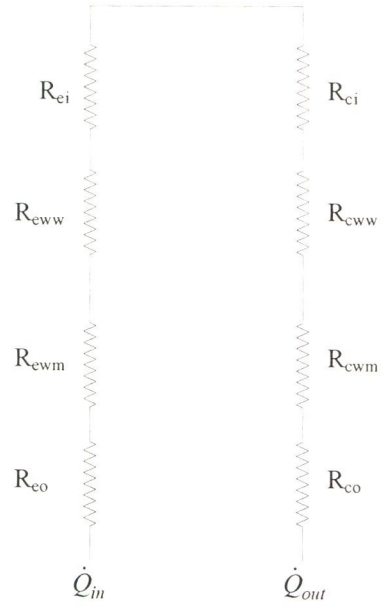

Figure G.8 Simplified thermal model of the heat pipe.

Where

R_{co} is the external surface resistance of the container wall.

R_{ewa} is the container wall axial resistance (excluding the wick).

R_{ewm} is the radial resistance of the container wall (excluding the wick).

R_{ewwa} is the wick axial resistance (excluding the fluid).

R_{efa} is the fluid axial resistance.

R_{eww} is the radial resistance of the wick.

R_{ei} is the liquid vapor interface resistance.

R_c is the vapor core resistance.

The above resistances refer to the evaporator section. The corresponding resistances for the condenser section start with the subscript c instead of e.

G.8 Application to the AFPM machine

The heat pipe in the thermal model was configured as in figure G.9. The calculation of how much heat is removed by the heat pipe was based on the following assumptions:

- The heat pipe remained at a constant temperature, equal to that of the air that cooled the finned surface or at a specified temperature.

- The internal resistances were taken to be negligible. The only resistances that were taken into account were the convective resistance on the inside wall of the heat pipe and the overall resistance of the finned surface.

The size and position of the heat pipe as well as the above-mentioned resistances are determined by the user. With these assumptions, the heat removed by the heat pipe is given by

$$\dot{Q}_{heatpipe} = \frac{T_{hot} - T_{cold}}{\frac{1}{h_{hot} A_{hot}} + \frac{1}{h_{cold} A_{cold}} + \frac{1}{\eta_{fin} h_{fin} A_{fin}}} \tag{G.15}$$

where T_{hot} is the average temperature of the elements that surround the heat pipe in the stator, T_{cold} is the temperature of the air which cools the finned surface, h_{hot} is the convective heat transfer coefficient on the inside wall of the heat pipe in the stator, A_{hot} is the exposed area of the heat pipe in the stator, h_{cold} is the convective heat transfer coefficient on the inside wall of the heat pipe in the finned area, A_{cold} is the exposed area of the heat pipe at the finned surface, η_{fin} is the efficiency of the finned surface, h_{fin} is the convective heat transfer coefficient on the surface of the fins and A_{fin} is the total exposed area of the finned surface.

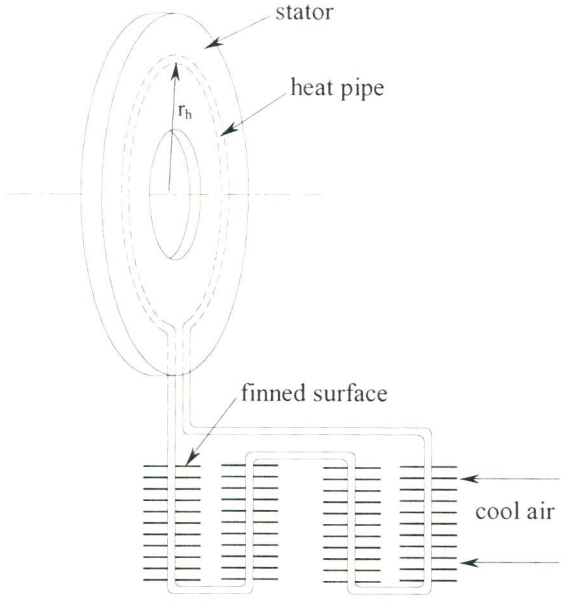

Figure G.9 Configuration of the heat pipe in the AFPM machine.

G.9 Conclusion

The most obvious pointer to the success of the heat pipe is the wide range of applications where its unique properties have proved beneficial. Some of these applications are (Faghri, 1995): electronics cooling, diecasting and injection moulding, heat recovery and other energy conserving uses, de-icing duties, cooking, cooling of batteries, control of manufacturing process temperatures, and as a means of transferring heat from fluidised beds.

The AFPM machine is another application where the heat pipe is beneficial. This appendix presented research done on heat pipes. The basic operating principles, design considerations and various limitations of heat pipes were discussed. The thermal modelling of heat pipes was presented as well as how the heat pipe was modelled in the thermal model of the AFPM machine.

Appendix H

Structural analysis of the AFPM machine model

H.1 Introduction

The Perspex model of the AFPM machine had to withstand rotational speeds of up to 2300 rpm for prolonged periods of time. To prevent catastrophic failure of the machine, its structural integrity would have to be investigated. In the case of the model not being able to withstand the centrifugal forces, design changes would have to be made to overcome this. In this section the structural analysis of the Perspex model is investigated.

H.2 FEM model

The structural analysis of the AFPM machine was conducted using Nastran, a finite element modeller. This version of Nastran used was limited to 300 nodes. The material properties used for the Perspex were (Callister, 1996)

Density = 1.5 g/cm^3

Modulus of elasticity = 2.5 GPa

Poisson's ratio = 0.38

Yield strength = 6.5 MPa

The rotor plates were identified as the main area of concern. A quarter model of one of the rotor plates was constructed. The maximum stress would be expected to be at the inner radius of the rotor plate. An approximate value of the hoop stress is given by the equation

$$\sigma_\theta = \frac{3+\nu}{4}\rho\omega^2\left(r_0^2 + \frac{(1-\nu)}{(3+\nu)}r_i^2\right) \qquad \text{(H.1)}$$

This gives a hoop stress of 2.45 MPa at the inner radius. This does not take into account the stress concentration due to holes or the step in the thickness of the plate. Therefore one could expect the actual stress to be slightly higher than this value. Figures H.1 and H.2 show the results of the analysis on the rotor plates.

H.3 Conclusion

From the results of the Nastran analysis the maximum von Mises stress was calculated at 2.7 MPa, which is below the yield strength for the Perspex. This value compares quite well with that

given by equation H.1. It was expected to be slightly higher. The maximum stress was found around the holes at the inner radius of the rotor plate, see figures H.1 and H.2. The calculated safety factor for the rotor plates is 2.4 and it can therefore be concluded that the rotor plates are capable of withstanding the centrifugal forces at 2300 rpm.

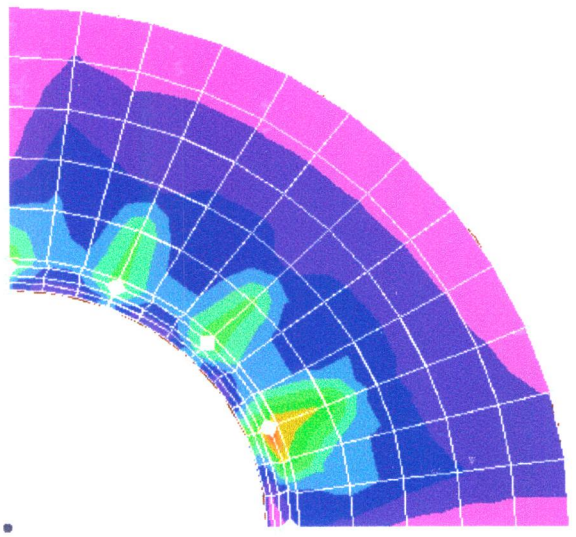

Figure H.1 Top view of the von Mises stresses.

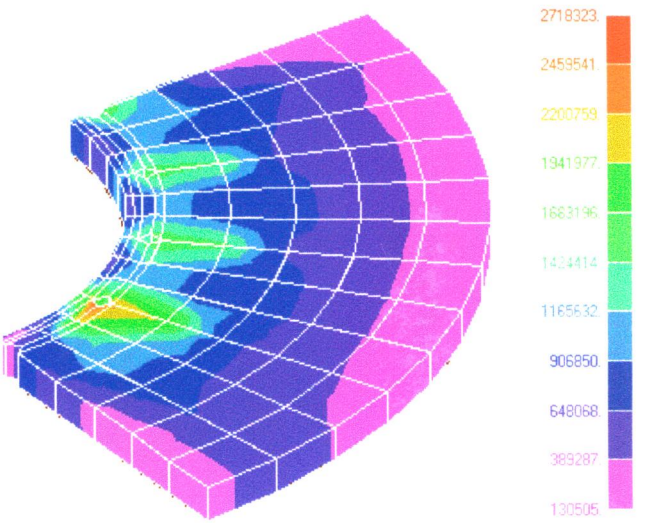

Figure H.2 Isometric view of the von Mises stresses.